Targeting of Vascular Cell Adhesion Molecule 1 with an Ultrasound Contrast Agent Bearing Designed Ankyrin Repeat Proteins as Targeting Ligands

Inauguraldissertation

zur

Erlangung der Würde eines Doktors der Philosophie

vorgelegt der

Philosophisch-Naturwissenschaftlichen Fakultät

der Universität Basel

von

Alexandra Kosareva

2021

Genehmigt von der Philosophisch-Naturwissenschaftlichen Fakultät

auf Antrag von

Prof. Dr. med. Beat Kaufmann

Prof. Dr. Christoph Handschin

Prof. Dr. Constantin von zur Mühlen

Basel, den 17. März 2020

Dekan Prof. Dr. Martin Spiess

Acknowledgements

First of all, I would like thank my supervisor, Prof. Dr. med. Beat Kaufmann, for giving me the opportunity to do my PhD in his research group, for helping me and encouraging me throughout the whole process. I cherish very much his constructive inputs and ideas, his support during experimental planning, manuscript writing, as well es his help with experiments in the lab. I was motivated with his dedicated and passionate approach to science, friendly and gentle nature and willingness to support me and take time for my questions.

I am very grateful to my colleague, Dr. Mukesh Punjabi, for his support and guidance through the difficult and emotional moments of the PhD. He introduced me to most of the experimental procedures and proper experimental planning. I am extremely thankful for his organization and support during the animal experimentation, for his willingness to help me with the troubleshooting of all the experiments and for readiness to share his knowledge and experience. I also would like to thank my colleague, Dr. Amanda Ochoa-Espinosa, for her open-minded and cheerful attitude to science and life. I appreciate a lot our discussions, her support with the experiments and her encouragement. I want to thank Dr. Lifen Xu, for the support with animal experiments and data evaluation. I am thankful for my former colleague, Dr. David Steinl, for sharing his knowledge and his useful advice. I would also like to thank Mariah Kohlbrenner and Georg Hofmann for their technical support.

Furthermore, I am very thankful to Prof. Dr. Christoph Handschin and Prof. Dr. Constantin von zur Mühlen, for co-supervising my work and giving me ideas for the experiments, and the group of Prof. Dr. Gabriela Kuster Pfister for their advice and help.

Many thanks to my friends from all over the world, especially from Basel, Munich, Moscow and Snezhinsk. They encouraged me to insist on my goals and believe in myself throughout this challenging time. Many thanks to my friends from the Russian lunch connection, who were supporting me during my PhD time here in Basel and made this time more joyful. I am thankful to the PhD community of DBM, where I got a lot of input from smart and talented people.

Last, but most important, I want to thank my family for always being by my side and supporting me by any problem. Although being far away, they were believing in me and encouraging me not to give up and reach my goals.

Contents

Abstract

Atherosclerosis is an inflammatory disease of the large arteries that progresses silently over decades until it causes stroke and myocardial infarction. In order to prevent such late complications, an early and reliable diagnosis of atherosclerosis is clinically needed. Vascular cell adhesion molecule 1 (VCAM-1) is expressed on the surface of endothelial cells throughout the pathogenesis of atherosclerosis and can therefore be used as a biomarker. Hence, non-invasive imaging of the expression of VCAM-1 could be used for early detection and risk stratification. Contrast enhanced ultrasound molecular imaging (CEUMI) of VCAM-1 was shown to be possible in mouse models of atherosclerosis. However, the ultrasound contrast agents that were used so far have relied on biotin-streptavidin conjugation chemistry and full-size antibodies as targeting agents, which are expensive, potentially immunogenic and may have low targeting efficiency. For clinical translation, there is thus an urgent need for the development of ultrasound contrast agents that use smaller, easy to produce and highly specific ligands. Designed Ankyrin Repeat Proteins (DARPins) are multipurpose affinity reagents that have not just been proven to recognize targets with exceptional specificity and selectivity, but that also may overcome the aforementioned limitations. Therefore, the aim of this work is to develop and characterize an ultrasound contrast agent carrying a DARPin ligand targeted to VCAM-1.

DARPin binders were selected from a large library though specific screening assays. After several screening rounds, 5 high affinity binders were identified and characterized. *In vitro* flow chamber experiments were performed with the purpose of predicting *in vivo* performance of the five selected binders. Subsequently, in a mouse model of hind limb inflammation, it could be shown that successful imaging of VCAM-1 expression in a low shear stress environment is possible using microbubbles bearing DARPins as ligands targeted to VCAM-1. However, the individual *in vivo* performance of the DARPin ligands was not predicted by the flow chamber studies. In a second step, three of the binders were selected to be tested in a pathologically relevant mouse model of atherosclerosis in the aortic arch. In this high-shear environment there were no differences in signal from microbubbles bearing DARPin ligands targeted to VCAM-1 versus a microbubble bearing a control DARPin ligand. Subsequent flow chamber studies performed using pulsatile shear stress and flow chamber experiments testing the off-rate of VCAM-1 targeted microbubbles bearing DARPin ligands indicate that a high off-rate could be primarily responsible for the lack of selective attachment.

1. Ultrasound

1.1. Medical Imaging

Medical imaging comprises several imaging technologies that in modern medicine are used to visualize the interiors of the body by non-invasive methods. Through accessing the function and physiology of organs and tissues, abnormalities can be identified and diseases diagnosed. Medical imaging is an inevitable element of state-of-the art health care everyday life and gives a lot of information to the doctors, which general examination fails to deliver. The most used modalities in medical imaging include conventional radiography, computed tomography (CT), magnetic resonance imaging (MRI), positron emission tomography (PET), single-photon emission computed tomography (SPECT) and ultrasound imaging. Depending on the organ structure or tissue that has to be imaged, an appropriate imaging modality is used to access the pathology with the best possible sensitivity and specificity. Table 1 gives an overview of the imaging modalities that are currently being used in clinical medicine and compares their main properties (Verma 2019). Over the past decades the capabilities of medical imaging have tremendously increased due to advances in technology as well as computing power. However, early disease progression is often outlined by pathological changes on the molecular level, for example upregulation or downregulation of certain structures on the cell surface, which are inaccessible by conventional imaging. To go beyond this limit, molecular imaging has been developed that utilizes functionalized contrast agents to image cellular functions and biological processes. It is thought that such techniques will allow for earlier disease detection, for a more refined assessment of disease progression and for monitoring the effect of therapies. Also, molecular imaging could in the future be a valuable technique to improve our understanding of disease mechanisms in appropriate *in vivo* models. Molecular imaging techniques have been developed for all major imaging modalities. Thus, radionuclides have been functionalized to enable molecular imaging for PET/SPECT (Xu, et al. 2009), magnetic nanoparticles (MNP, (Issa, et al. 2013)) and ultrasmall particles of iron oxide (USPIO, (Ruehm, et al. 2001)) have been used for MRI and iodinated nanoparticles for CT scans (Cormode, et al. 2010, Pysz, et al. 2010). For ultrasound molecular imaging, microbubbles (MBs) that are functionalized to recognize different cellular structures are used (Deshpande, et al. 2010).

This work is focused on the application of contrast enhanced ultrasound molecular imaging (CEUMI) for early disease diagnosis. Compared to other imaging modalities, CEUMI is characterized by a positive tradeoff between resolution and sensitivity for the tracer. Moreover, ultrasound imaging is safe, as it does not require ionizing radiation, widely available and affordable. It can be used in real time and provide information from moving organs, which cannot be obtained from static images.

Table 1: Comparison of medical imaging modalities. Adapted from (Verma, 2019).

Modalities	**X-Ray**	**CT**	**MRI**	**PET**	**SPECT**	**Ultrasound**
Radiation source and type	X-rays (ionizing)	X-rays (ionizing)	Electric and magnetic fields (non-ionizing)	Positron radiation (ionizing)	Photons (ionizing)	Ultrasound waves (non-ionizing)
Cost	Low	High	High	High	High	Low
Spatial resolution	50-200 µm	50-200 µm	25-100 µm	1-2 mm	0.5-1 mm	50-500 µm
Penetration depth	No limit	No limit	No limit	No limit	No limit	mm-cm
Advantages	Fast and easy	No super-position of overlapping structures	Variable thickness, any tissue and plane are discriminated	Efficient in distinguishing benign and malign tumors	Imaging of neuro-degenerative diseases	Non-invasive, easy to use, widely available
Disadvantages	Super-position of structures makes the inter-pretation difficult	High radiation dose	Expensive, very uncomfortable for the patient, impossible for patients with metallic implants	Radiation exposure, limited time for imaging	Blurring effect, attenuation compensation is not possible, radiation exposure	Operator dependency, difficult to images bones and lungs
Contrast agent for molecular imaging	Iodinated nano-particles	Iodinated nano-particles	MNP, USPIO	Radionuclides	Radionuclides	Microbubbles

1.2. Ultrasound Wave Characteristics

Sound waves with higher frequencies than the upper acoustic perception limit in humans (>20 kHz) are referred to as ultrasound (Figure 1). Ultrasound imaging has been developed and is widely used in modern clinical medicine for the assessment of tissue structure and function in virtually all medical subspecialties.

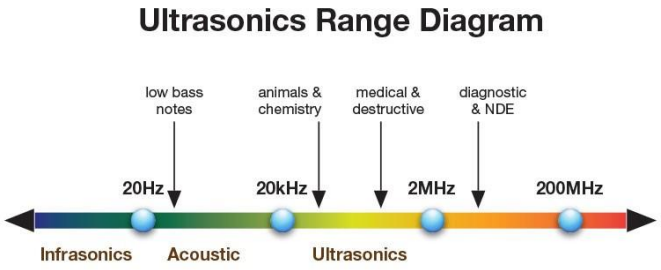

Figure 1: Frequency range of sound. Frequencies under 20 Hz are referred to as Infrasound, from 20 Hz to 20 kHz as audible sound and upper than 20 kHz as ultrasound. Adapted from Wikipedia article on ultrasound.

Ultrasound can travel through tissue in the form of a longitudinal wave (Figure 2), which is characterized by the frequency (f, MHz) and its inverse, the wavelength (λ, mm), the amplitude (A, MPa) and the speed of propagation (c, m/s) and causes regions of compression and rarefaction (decompression) (Conrad 2010) within the tissue. The wavelength is the distance between successive crests of a wave and is dependent on the speed of a sound wave and its frequency (Equation 1). For soft tissues it is around 0.1-0.8 mm.

$$\lambda = \frac{c}{f} \qquad \text{Equation 1}$$

The velocity of a longitudinal wave is dependent on the media it travels in and not on the characteristics of the sound. In soft tissues the speed of ultrasound is around 1540 m/s on average, which is much faster compared to the speed of propagation in air (340 m/s), whereas in bone it is much faster (4100 m/s).

An important parameter of an ultrasound wave is its amplitude. The amplitude is related to the energy component of the ultrasound wave. It relates to the “loudness” of the wave and is expressed as pressure amplitude (A) described in megapascals (MPa), Figure 2. The amplitude of an ultrasound wave is related to the compression of the tissue that the wave travels through. Usually on clinical ultrasound systems, the amplitude of the sound wave is displayed as a relative value on a logarithmic scale in decibels (dB).

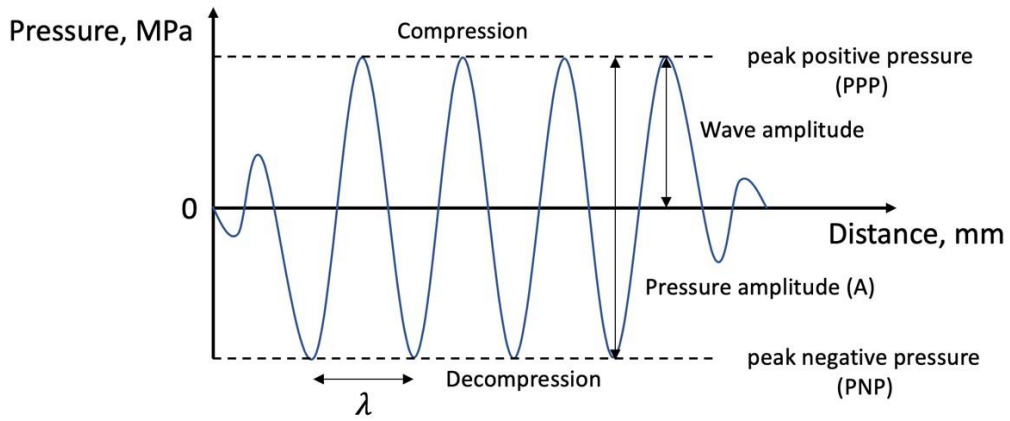

Figure 2: Parameters of pressure (sound) waves. They are characterized by the wave length (λ), the amplitude, the phases of compression and decompression, as well as the speed of propagation (c). Adapted from (Schrope and Goel, 2014).

The power of the ultrasound beam is the rate of energy transferred to the tissue and is expressed in Watts (W). The intensity of the ultrasound beam is the concentration of energy within the beam and is expressed as the rate at which power passes through an area unit of the tissue (W per cm^2). Intensity is as well indirectly proportional to the square of the penetration depth, so it will rapidly decrease with increasing tissue depth as the ultrasound wave is being attenuated (Equation 2).

$$Intensity = \frac{Power,}{Beam\ area}, (\frac{mW}{cm^7}) \qquad \text{Equation 2}$$

Assuming a constant propagation speed and compressibility of a particular tissue, intensity is proportional to the pressure (or pressure amplitude) squared and the pulse rate. Since the pulse rate is fixed in most systems, intensity is only determined by the pressure amplitude of the ultrasound wave (Equation 3).

$$Intensity \sim Pressure\ Amplitude^7 \qquad \text{Equation 3}$$

The frequency of a sound wave is determined by its source. For instance, in a piano, the source of sound is a string that is vibrating by striking it. Each string is adjusted to vibrate at a certain resonant frequency. In medical imaging, ultrasound wave is generated by a transducer, which consists of an array of piezoelectric crystals (Figure 3). When alternating current voltage is applied to an individual crystal, the crystal oscillates at the frequency of alternating current. The oscillation of the crystal produces an ultrasound wave at the same frequency. In other words, the piezoelectric crystal is used to convert electrical energy into mechanical energy, this has also been called the piezoelectric effect. These electrical signals are sent to the ultrasound scanner. In medical ultrasound frequencies from 1-20 MHz are usually utilized (Chan 2011). A backing material ensures for unidirectional emission of

sound waves. By selective and time-dependent activation of parts of an array, complex waves can be generated. After receiving an echo, amplification is used to increase the size of electrical pulses. The amount of amplification is dependent on gain settings.

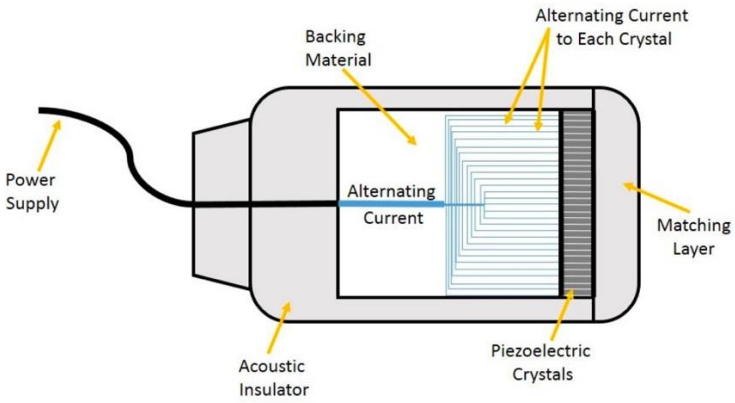

Figure 3: Scheme of a typical transducer. Alternating current is applied to each of an array of piezoelectric crystals to generate ultrasound. Picture from VAULT.

1.3. Generation of a 2D image

Ultrasound waves are emitted in rapid short pulses, controlled by pulse generator (Figure 4). For conventional ultrasound imaging protocols, a pulse rate of approximately 1000 pulses per second (1 kHz) is applied (not to be confused with the frequency of the ultrasound wave itself, controlled by the transducer, 1-20 MHz). Pulse duration, as well as pulse rate are important parameters for ultrasound imaging because they define frame rate and therewith temporal image resolution. Pulse duration is controlled by the damping characteristics of the transducer. Damping stops the vibrating of the transducer after sending a pulse.

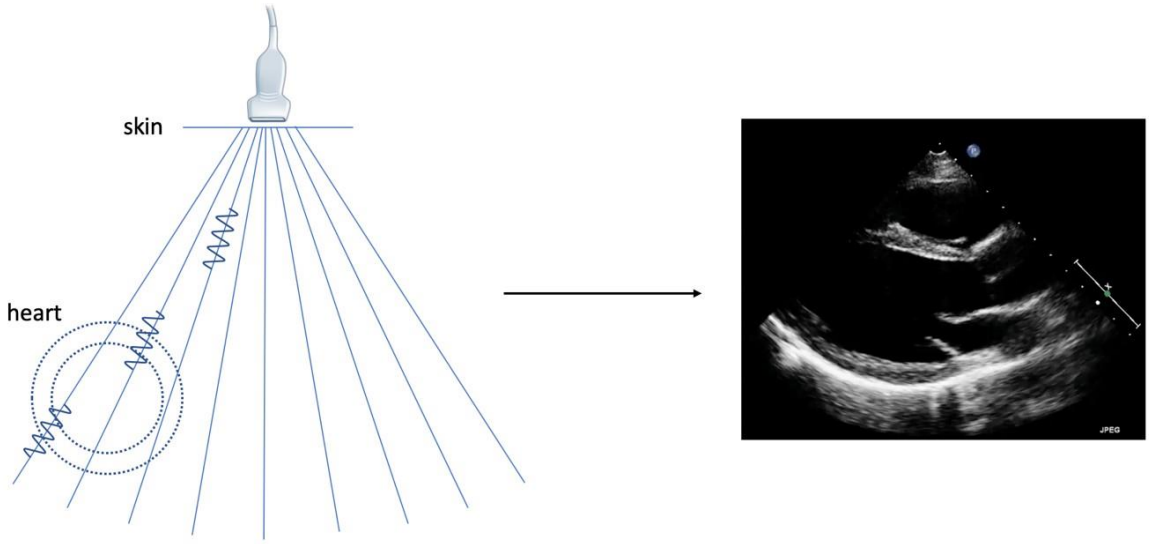

Figure 4: Example of pulsed ultrasound imaging. The sequence of 3 short pulses is shown. Between the pulses a listening period of the transducer takes place to detect the echo and no echoes are sent.

Compared to audible sound, ultrasound waves can be sent in a certain direction. Sent from the transducer, an ultrasound wave travels through the human body and is partially reflected from the boundaries between tissues and partially lost through acoustic attenuation. Attenuation is a loss in intensity (amplitude) of the wave over distance and it includes diffuse reflection, scattering, refraction and absorption. Diffuse reflection happens when a wave hits on irregularities at the interface and gets reflected at various angles. Scattering occurs when a sound wave hits a structure that is smaller than the wave length, such as blood cells or ultrasound contrast agents. Depending on the shape and orientation of the particles, scattering is stochastically directed in the direction of the incident wave (forward scattering), or the in opposite direction (backscattering). Refraction happens when a wave hits the interface at an angle less than 90° and gets refracted away from the transducer with angle of incidence. During absorption the energy of the ultrasound wave is transformed into heat. Absorption increases with penetration depth. Attenuation is greatly influenced by the frequency of the incident wave. Ultrasound waves with higher frequencies are more readily attenuated due to the rapid energy loss.

The sound wave is most effectively reflected at the boundaries of tissues with different acoustic properties, which have a big difference in the ability to be displaced under the influence of the pressure wave, or acoustic impedance, such as interfaces between blood and soft tissue. The part of the ultrasound wave that is reflected within the tissue is called an echo, which is then used to reconstruct the image (Figure 4). Since the speed of sound in soft tissues is known and the time between sending and receiving an echo can be calculated, one can determine the exact depth of the reflecting structure in the body. This distance is then used for the generation of two-dimensional images of tissues and organs.

1.4. Ultrasound Resolution

Resolution is one of the most important parameters that define the quality of an imaging modality. In ultrasound imaging, axial and lateral spatial resolution as well as temporal resolution are influenced by different aspects of the ultrasound wave characteristics.

Spatial resolution of ultrasound imaging is the ability of the system to distinguish two different structures at a certain imaging depth in two dimensions: lateral (perpendicular to the beam axis) and axial (parallel to the beam axis). Lateral resolution is dependent on the beam width, which is set by the size of piezoelectric element. As the wave travels through the body, the beam width changes, and the rate of change is determined by the focusing characteristics of the transducer. Transducers can be used in focused and non-focused mode, whereby a focused beam is desirable for the most imaging applications. Focused beam has a smaller beam width, as a focal zone is created, where the beam is higher in amplitude. In turn, resolution of the structures in the focal zone is increased. By creating a narrow focal zone, lateral resolution can be increased, but it is decreased before and behind the focal region, axial resolution is not affected by focusing.

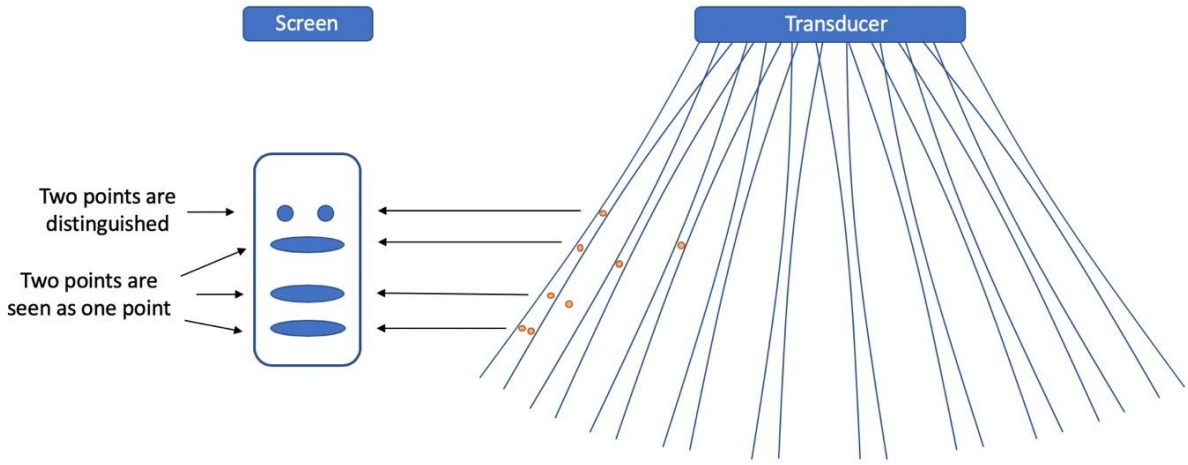

Figure 5: Lateral resolution can be influenced by focusing and increasing the number of scan lines.

The axial spatial resolution in turn depends on the wavelength (frequency) and the length of the individual ultrasound pulse train sent into tissue. As shown in Figure 6, returning echoes from two surfaces will overlap and, thus not resolve two individual surfaces when the pulse length is too large. On the contrary, by decreasing the pulse length, returning echoes are separated by a gap and therefore resolve the two surfaces. The smaller the wavelength and shorter the pulse train, the higher the resolution. Intuitively, one would choose higher frequencies to improve axial resolution, however, acoustic attenuation increases with increasing frequencies, and therefore high frequency ultrasound

will have a limited penetration into tissue. Thus, a trade-off needs to be made between using higher frequencies (better axial resolution) and lower frequencies (better penetration depth). For typical ultrasound imaging procedure with frequency about 3-5 MHz, the resolution is between 50-500 µm and the penetration depth is about 20 cm.

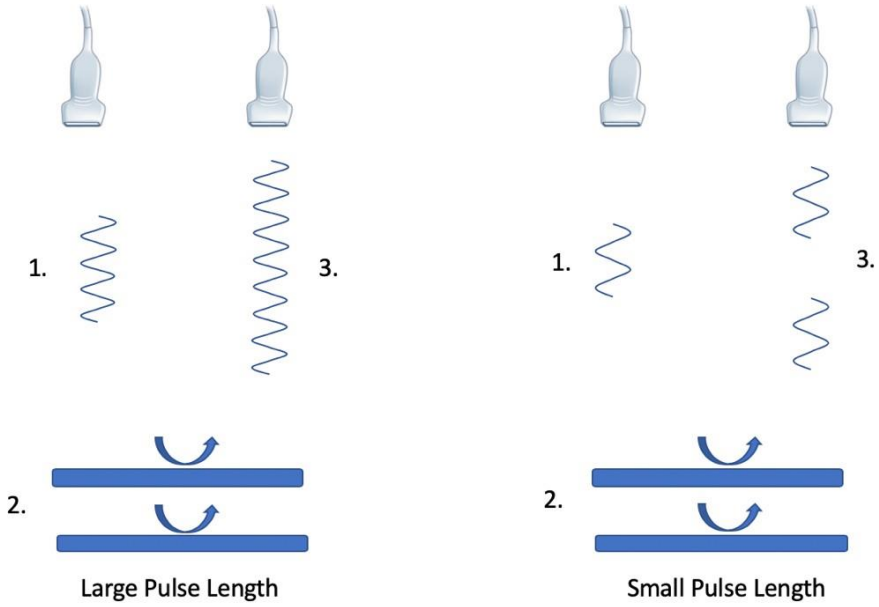

Figure 6: Schematic illustration of the influence of spatial pulse length on the axial spatial resolution.

Temporal resolution depends on how fast the frame rate is, or how many image frames can be made per second, expressed in Hz. Temporal resolution can be improved by reducing the time needed for imaging. This can be achieved by reducing the image width, decreasing the depth of imaging and decreasing the scan line density, the latter will, however, compromise the lateral aspect of spatial resolution (Wong 2014).

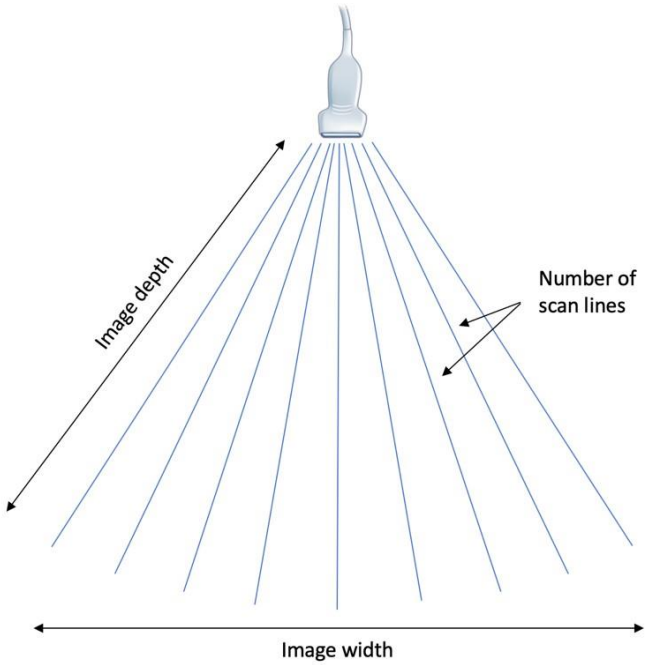

Figure 7: Temporal resolution can be improved by decreasing the image depth, image width or the number of scan lines. Adapted from (Wong 2014).

1.5. Bioeffects produced by ultrasound

While ultrasound imaging in clinical practice is not associated with any hazard, there are two potential bioeffects that have to be taken into account for ultrasound technology. First, absorption of the ultrasound energy and conversion to thermal energy could potentially lead to heating and damage of insonified tissue. Therefore, regulative authorities require that every ultrasound machine that is in clinical use displays the thermal index (TI) on the screen. The TI is a rough estimate of how much tissue can be heated if the transducer is held constant over a long period of time. Thermal indices are different for bone versus soft tissue. Generally, a TI for soft tissue is displayed on ultrasound devices.

The second bioeffect that can potentially result from ultrasound energy is cavitation. Cavitation is defined as formation (from dissolved gas within tissues), expansion and contraction or collapse of bubbles caused by the acoustic pressure of the ultrasound beam (Sen, et al. 2015). As the collapsing can occur rather violently, tissue damage can be caused. The probability of cavitation occurring within the tissue is related to the energy delivered. In order to avoid this bioeffect, regulative authorities require clinical ultrasound machines to have a limit on the energy maximally delivered to tissue and to display a measure thereof on the ultrasound image.

This measure, the mechanical index (MI), which expresses the probability for the occurrence of cavitation within tissue, is defined as peak negative pressure (PNP), divided by the square root of the ultrasound frequency (Equation 4).

$$MI = \frac{PNP}{A\sqrt{f}} \qquad \text{Equation 4}$$

The magnitude of cavitation is dependent on the power of the ultrasound beam. The square root of the frequency reflects the experimental observation that the probability of cavitation is higher at lower frequencies. Regulative authorities demand that the energy delivered to tissue by clinical ultrasound scanners is limited to a maximum of an MI of 1.9.

1.6. Ultrasound Contrast Agents (UCAs)

In ultrasound imaging it is often a problem to visualize the vascularization of the organs, as vessels are poorly visible on the ultrasound images. For this reason, UCAs have been developed to highlight the blood pool. UCAs are particles that backscatter ultrasound waves more efficiently than tissues. UCAs can be injected into the circulation and increase the contrast of the blood stream to distinguish blood vessels from the tissue (Malm, et al. 2004). The main types of UCAs include microbubbles (MBs), nanobubbles (NBs), phase change contrast agents (PCCAs) and echogenic liposomes (ELIPs).

The first and most commonly used UCAs, MBs (Figure 8A), have been originally introduced by Gramiak and Shah in 1968 and were used to opacify (increase the echogenicity and therewith the contrast) the blood pool (Gramiak and Shah 1968). MBs are 1-8 µm in diameter and usually consist of phospholipid, albumin or biopolymer shell and a gas core (Kaufmann, et al. 2007). Heavy gas cores, such as perfluorocarbon or sulfur hexafluoride are normally used to increase the stability of the MBs, as compared to air or nitrogen, the former are bulky molecules that diffuse slowly from the core of the MB. Polydisperse MBs are prepared by sonication of the lipid emulsion by simultaneous gas introduction. Monodisperse MBs can be prepared by using microfluidic flow focusing devices (Talu, et al. 2007). Addition of polyethylene glycol (PEG) to the emulsion for production of MBs is often used. This results in the creation of a PEG brush on the shell surface upon sonification. The PEG brush in turn limits the MB coalescence (merging of many MBs to a single MB) and increases the half-life in the blood stream (Klibanov, et al. 1990). Moreover, the PEG brush prevents the direct contact of MB shell lipids with endothelial cells, leukocytes or proteins of the complement system (Fischer 2002, Chen and Borden 2010).

Due to their size, MBs are limited to the vascular compartment, so in order to image non-vascular structures with ultrasound, other UCAs were developed. It is known that in tumor tissue, endothelial cells lack tight junctions, so that the gap between the cells can reach 800 nm (Hobbs, et al. 1998). With the development of NBs with a size distribution of 100-1000 nm, the extravasation of the contrast agent into the tumor tissue has become possible (Figure 8C). Once extravasated, NBs coalesce to form larger, highly echogenic MBs and increase tumor contrast (Rapoport, et al. 2007). The formulation of NBs is similar to MBs, consisting of a lipid shell and a heavy gas core. NBs are obtained from a polydisperse preparation by physical filtering or floatation centrifugation (Yin, et al. 2012).

Another type of UCAs are phase change contrast agents (PCCAs) are nanodroplets, which consist of a lipid shell and liquid heavy gas core and are less than a micron in diameter (Rojas and Dayton 2019) (Figure 8D). The liquid aggregate state of the gas is achieved through temperature decrease and mechanical pressure that alter the boiling point. When exposed to pulsed ultrasound, the gas within nanodroplets vaporizes and can be detected (Sheeran, et al. 2011, Wilson, et al. 2012).

Last, echogenic liposomes (ELIPs) are another kind of UCAs, which consist of a lipid bilayer and gas pockets, which are entrapped whether in the shell or in the liquid core (Huang 2008, Paul, et al. 2014) (Figure 8B).

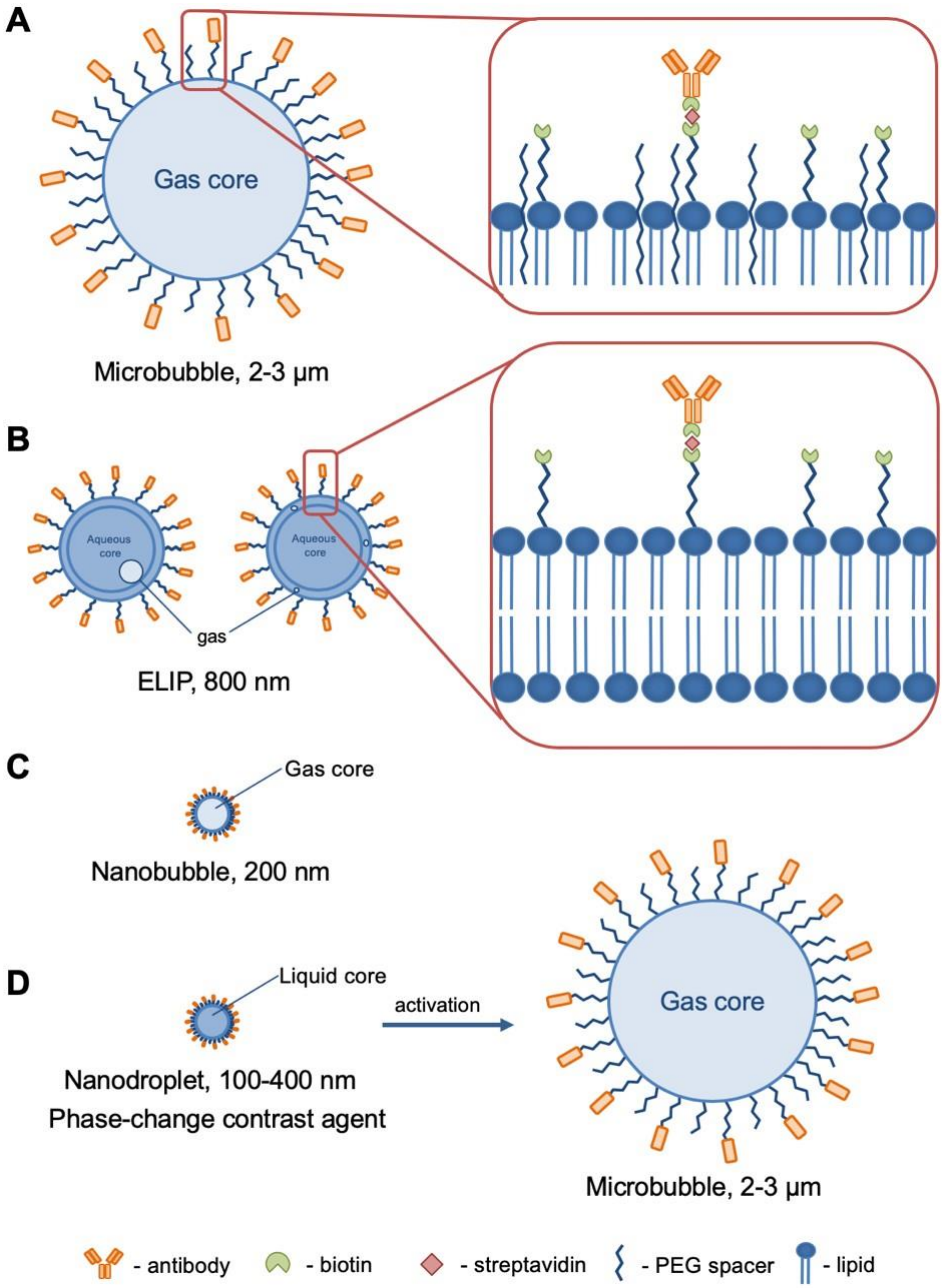

Figure 8: Different types of UCAs. A: microbubbles (MBs), B: echogenic liposomes (ELIPs), C: Nanobubbles (NBs), D: Phase-change-contrast-agents (PCCAs). From (Kosareva et.al. 2019).

1.7. Microbubble Pharmacology and Rheology

Due to their small size, MBs travel freely through the circulation. They neither aggregate or cause obstruction of the capillaries and overall show a behavior similar to red blood cells in terms of flow velocity (Jayaweera, et al. 1994, Lindner, et al. 2002). However, MBs cannot extravasate, as they are too big compared to the cell junctions. After some minutes of circulation (Landmark, et al. 2008), MBs are taken up by the splenic and hepatic reticuloendothelial system and are then phagocytized by Kupfer cells in the liver (Yanagisawa, et al. 2007, Willmann, et al. 2008), the gas is exhaled via lungs.

1.8. Contrast Specific Ultrasound Imaging

The aim of the contrast specific ultrasound imaging protocols is to increase the contrast signal-to-tissue ratio by efficiently imaging MBs while suppressing the signal from the surrounding tissue. The principle of contrast agent detection relies on the compressibility of the encapsulated gas, which is higher compared to the surrounding tissue. When exposed to an ultrasound field, MBs undergo cycles of compression during the peak positive pressure and expansion during the peak negative pressure, related to as volumetric oscillations (Dayton, et al. 1999). The resonance frequency of MBs is close to the frequencies used in medical ultrasound and they resonate efficiently when exposed to ultrasound (De Jong 1992).

To understand the process of echo generation from contrast agents, it is important to understand the process of ultrasound wave propagation and the response form the surrounding tissue. Speaking of ultrasound wave propagation, it is worth to mention that an incident pulse itself propagates non-linearly through the tissue. This happens because the peaks of a pressure propagate faster than the pressure nadirs, so at some point the peaks meet the troughs. This effect increases with the amplitude and distance. Depending on the distance traveled in tissue, frequencies other than the fundamental frequency are generated. The frequency spectrum of a sound wave with a certain amplitude that has traveled in tissue will therefore not only contain the fundamental frequency (f_c), but also harmonic components thereof, such as double the fundamental frequency, or second harmonics ($2f_c$), triple of the fundamental frequency or third harmonics ($3f_c$) and so on (Whittingham 2005). Consequently, since the incident waveform is distorted, the echo from tissues will contain harmonic components, dependent on the incident amplitude and the position of the tissue in the beam.

This fact is used in a imaging technique called tissue harmonic imaging. In this technique the receiver is restricted to echoes with a significant harmonic component, which are the echoes from tissues near the beam axis, where transmitted pulses are stronger and more tissue harmonics are generated. By using UCAs, specific imaging techniques can be applied to suppress the tissue signal and increase signal-to-tissue ratio from the contrast agents.

Depending on the amplitude of the ultrasound wave, the oscillations of the contrast agents can relate linearly or non-linearly to the incident acoustic pressure.

Linear oscillations

At lower peak pressure amplitudes (<100kPa) microbubble oscillations correspond to the rarefaction and compression of the incident ultrasound wave with a similar frequency in a linear manner and do not produce harmonic components. Nevertheless, compared to the echo from blood cells, the resulting backscatter from microbubbles is of several magnitudes higher in amplitude, because of the difference in acoustic impedance between microbubbles core gas and liquid.

Non-linear oscillations

When the peak pressure amplitude is increased (0.1 – 1 MPa), the ultrasound backscattered from the microbubbles becomes non-linear. This peculiar behavior of the microbubbles results from their asymmetrical compression and rarefaction response to the incident pressure (Figure 9, (Averkiou, et al. 2003)). This happens because the density and hence the stiffness of the encapsulated gas increases during compression and decreases during expansion, so that MBs compress less and expand more and thus stay longer in the expanded state. This effect causes the asymmetric movement of the microbubbles wall and is referred to as non-linear oscillation.

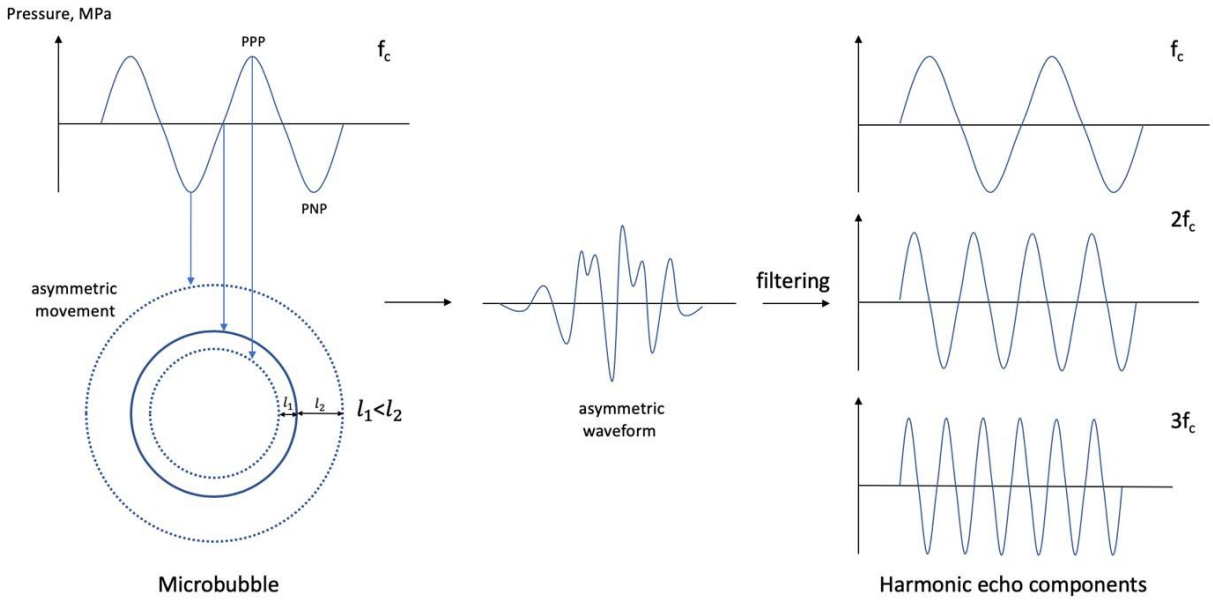

Figure 9: Schematic model of an asymmetrical MB movement during expansion and contraction in an ultrasound wave. An example of an incident pulse and the echoes from a microbubble. The echo from a microbubble is a composite of fundamental and harmonic frequencies. Adapted from (Whittingham 2005).

The non-linearity of the scattering process creates prominent harmonic and subharmonic components in the back-scatter of the microbubbles (Figure 10). A strong signal is returned at the incident

(fundamental) frequency and harmonic peaks are generated at the multiples of the fundamental frequency. As the amplitude of the harmonic signal from the microbubbles is several magnitudes higher than harmonic signal from the surrounding tissue, filtering out the harmonic signal enhances the signal-to-tissue-ratio during contrast imaging.

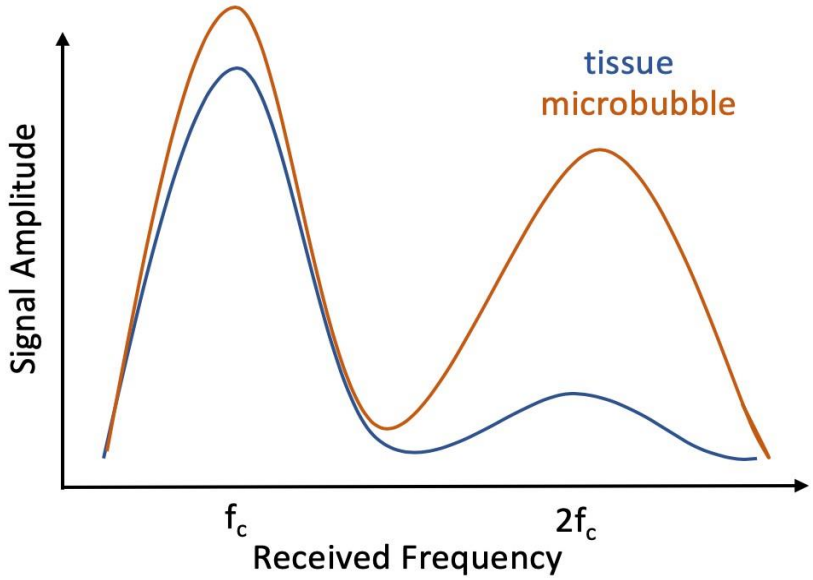

Figure 10: Schematic representation of the received echo from microbubbles and from tissue. Microbubbles give a stronger second harmonic signal ($2f_c$) than the tissue, signal at fundamental frequency (fc) is not greatly different. Adapted from (Kaufmann et.al., 2007).

The echo from MBs shows a non-proportional change in peak amplitude and a higher harmonic content, compared to the surrounding tissue. However, the second harmonic component of the surrounding tissue can be quite high in case of imaging with high amplitudes. To increase the signal from microbubbles, one strategy would be to simply subtract the background signal acquired from pre-contrast frames, thus filtering out the harmonic component from the microbubbles. To further increase the signal-to-tissue ratio, specific multipulse protocols were developed.

1.9. Multipulse protocols

Pulse Inversion

In this technique, two short pulses are transmitted, with the waveform of the second one being phase-inverted relative to the first one (Figure 11). Scattered echoes from tissues will be cancelled out when summing up the two echoes. The two non-linear echoes from the MBs will not be cancelled out by addition (Whittingham 2005). This imaging algorithm results in a very efficient suppression of tissue signal while generating a strong signal from MBs. However, by using successive pulses it is susceptible to motion artefacts when used on rapidly moving structures.

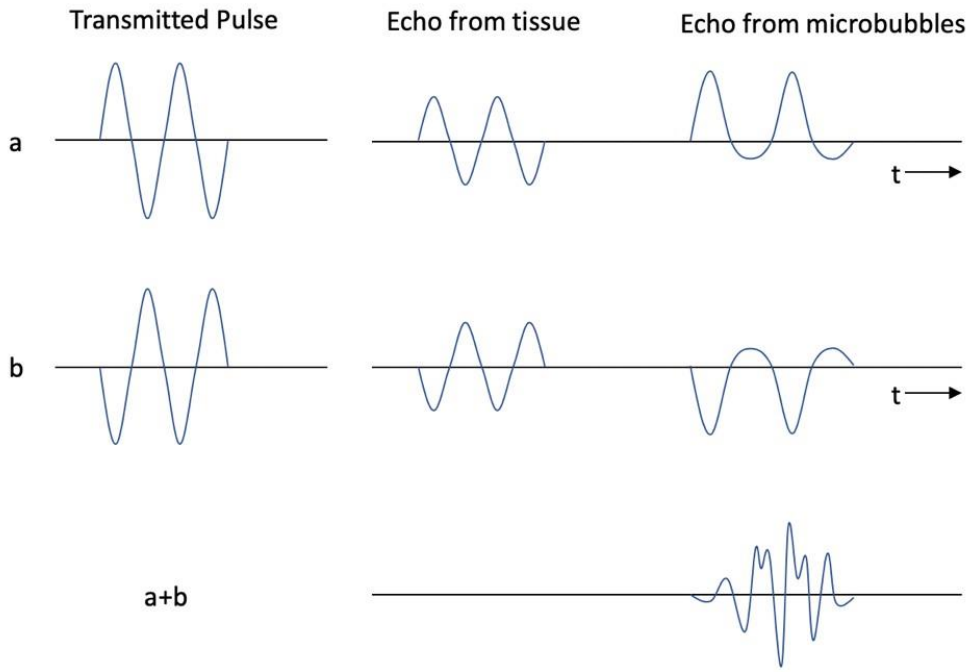

Figure 11: Schematic illustration of pulse inversion imaging to improve signal to noise ratio in contrast enhanced imaging. In this method two pulses with an inverted phase are transmitted. By summarizing the two echoes the signal from the tissue will be eliminated and the non-linear signal from microbubbles will be enhanced. Adapted from (Whittingham T.A.)

Power Modulation

In this approach two pulses are transmitted with different amplitudes, with the second being typically the double of the first one (Figure 12). During image processing the echo from the first pulse is multiplied by two before being subtracted from the echo from the second pulse. This results in signal cancellation from the tissue. The same pulses, when reflected from the MBs, would differ from each other and will be therefore not cancelled out. Similar to pulse inversion, power modulation imaging results in an excellent signal-to-tissue ratio, but is susceptible to motion artefacts.

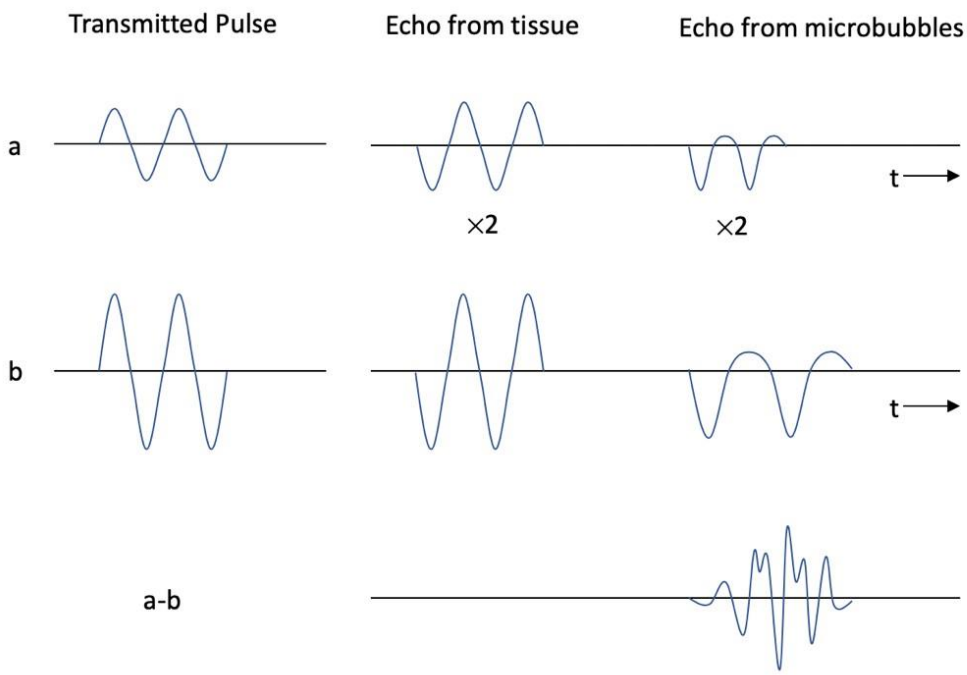

Figure 12: Schematic illustration of power modulation imaging to improve signal to noise ratio in contrast enhanced imaging. In this method two pulses are transmitted, one having the half of the amplitude than the other. The echo signal from the smaller pulse will be multiplied by 2 and subtracted from the echo from another pulse. Linear signal from the tissue is eliminated. The non-linear response from the microbubbles will result in signal enhancement.

Combined Amplitude Modulation and Pulse Inversion/Phase Shift: Contrast Pulse Sequence (CPS) Imaging

CPS is an imaging method, which combines harmonic imaging, pulse inversion and power modulation. Different phase shifts can be exploited with this technique, combined with amplitude modulation. During image processing, the echo sequence is first amplified by a particular weighting factor and then summed up. It is possible to suppress the fundamental or any harmonic frequency of the echo.

In Figure 13 an example of CPS on the ACUSON Sequoia Ultrasound Platform is shown. In this set up a half-amplitude, positive 0-degree pulse is first transmitted. The received signal includes linear fundamental signal component from the tissue, which is immediately suppressed, non-linear fundamental and non-linear harmonic components. Next, a full-amplitude, 180-degree inverted pulse is transmitted. In this case a non-linear echo from the MBs is much greater than that from the tissue. Lastly, another half-amplitude 0-degree pulse is transmitted. The received signals are similar to the echoes from the first pulse. By summing up all the received echoes, non-linear fundamental and harmonic signals from the microbubbles are enhanced.

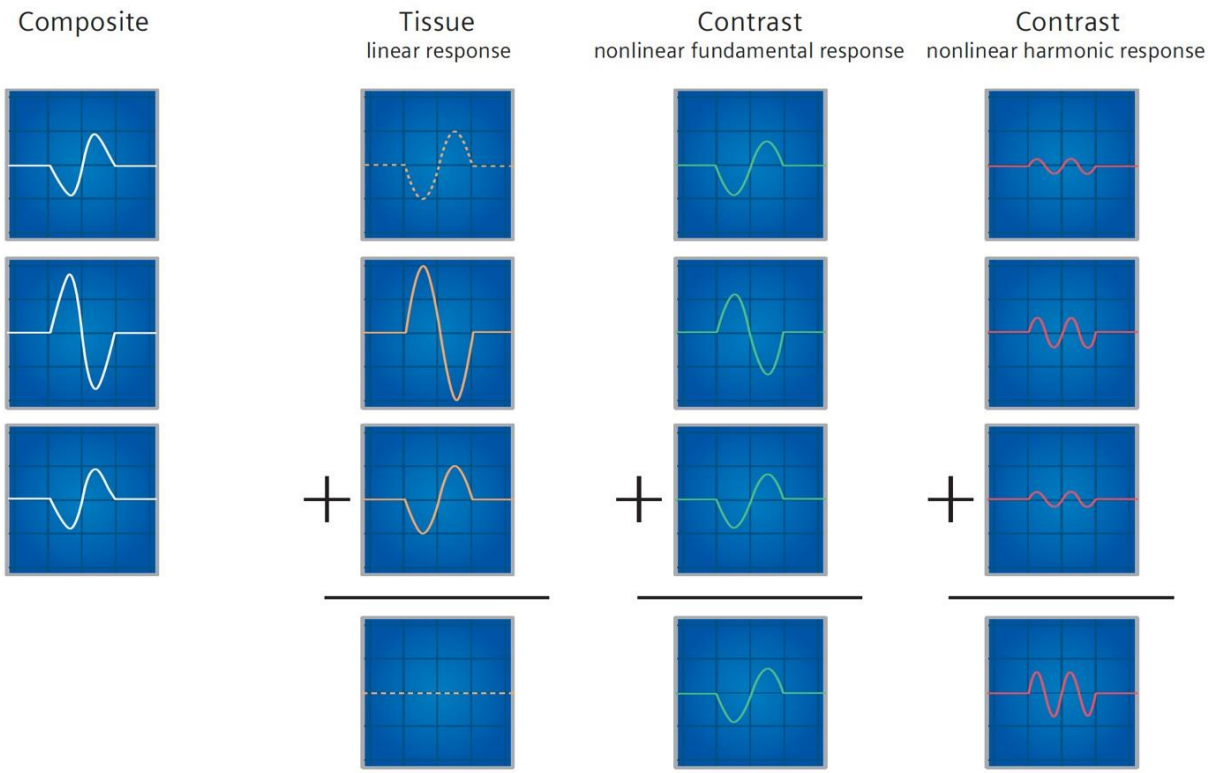

Figure 13: An example of CPS on the ACUSON Sequoia Ultrasound Platform. Cadence CPS removes the linear fundamental signal leaving the non-linear fundamental and other harmonic signals. Picture from Siemens medical (Cadence Contrast Agent Imaging Technology).

1.10. Clinical Use of Microbubbles

In the clinics, MBs are normally used in echocardiography to highlight the blood circulation for better delineation of the left vertical (LV) to better assess its function and structure (Figure 14) or to inspect myocardial perfusion (Lindner, et al. 1998, Wei, et al. 1998, Senior and Khattar 2017). Also, MBs are routinely used for the detection of liver metastases and of focal pathologies in the kidney, pancreas, spleen, breast, ovary and prostate by assessing the perfusion of these organs (Wilson, et al. 2009).

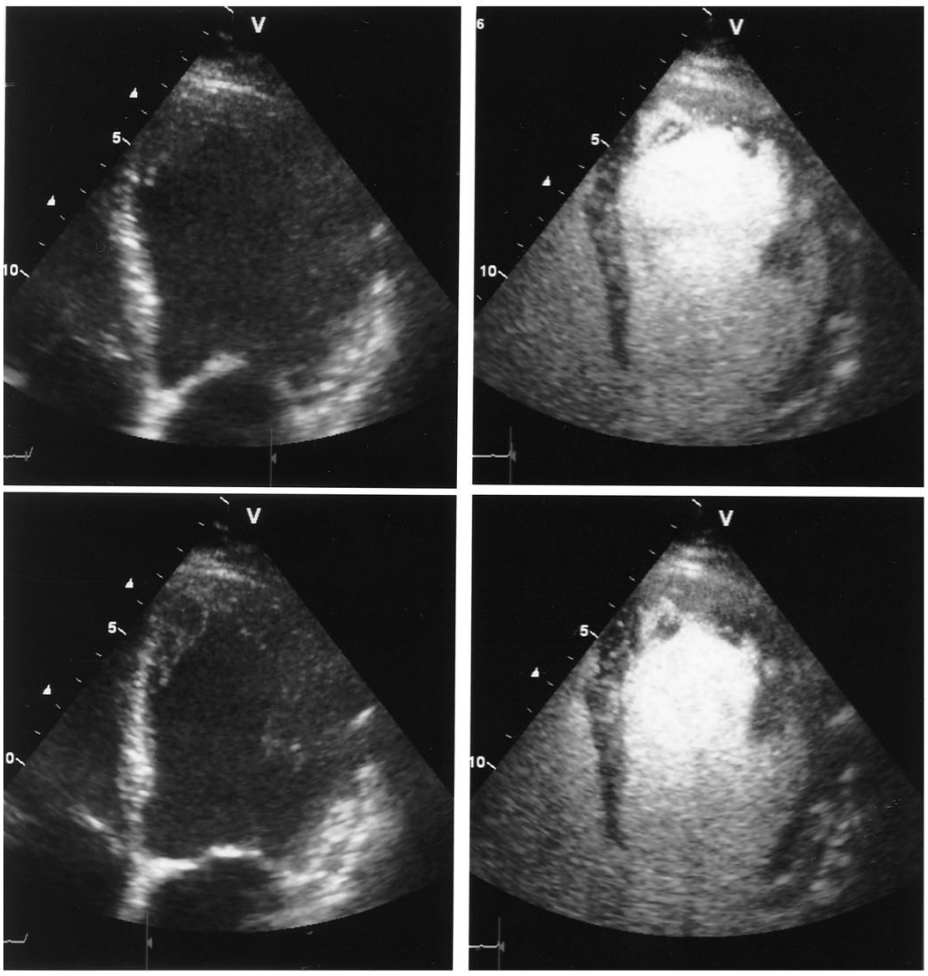

Figure 14: Representative images of end-diastolic (top) and end-systolic (bottom) images of the apical four-chamber view from a patient before (left) and after (right) contrast agent administration. Picture from (Malm, et.al. 2004). In contrast enhanced images myocardial wall motion can be accessed.

1.11. Contrast enhanced ultrasound molecular imaging (CEUMI)

Contrast agents have been successfully used in the clinical field to assess structure and function of organs and tissues, such as LV function and tissue perfusion, as mentioned before. However, a number of pathological processes, especially early disease progression, take place at the molecular level and are inaccessible for conventional imaging. To be able to image those molecular changes, techniques have been developed to functionalize existing contrast agents by conjugating ligands on their surface and thus make them bind to certain molecular targets. Imaging procedures for the use of functionalized contrast agents are referred to as contrast enhanced ultrasound molecular imaging (CEUMI).

1.11.1. Targeting strategies for CEUMI

When microbubbles are used as contrast agents, CEUMI aims to target specific molecular targets on the surface of endothelial cells in the vasculature. Two strategies are widely used for targeting: changing the shell composition of the contrast agent for binding of microbubbles to areas of inflammation or conjugating a targeting ligand specific for a particular disease-related molecule on the surface of the contrast agent.

The first strategy exploits the negative charge of the microbubble surface provided through the incorporation of phosphatidylserine in the shell of the MB (Fisher, et al. 2002). This results in rapid attachment of complement fragments to the MB, which are bound to activated leukocytes during the process of inflammation in the tissue (Lindner, et al. 2000). Similarly, MBs that consist of albumin, are known to bind to activated leucocytes in a similar way, through binding complement fragments (Anderson, et al. 2007) or via β2-integrins (Lindner, et al. 2000). Despite viscoelastic damping, phagocytized microbubbles can be detected after intake by monocytes, neutrophils and macrophages and can be used for imaging of inflammation *in vivo* (Lindner, et al. 2000). After half an hour after being phagocytized, MBs can remain acoustically active, as it was shown by imaging the cremaster muscle of mice in the presence of TNF-α induced inflammation. The assumption that the signal originates from the phagocytosed microbubbles was supported by the intravital microscopy performed directly before imaging.

The second strategy represents a more versatile way of targeting molecular markers and relies on conjugating binding ligands on the surface of the MB, such as antibodies, peptides, oligosaccharides or glycoproteins. Antibodies are commonly used in preclinical research, as they bind their targets with high affinity and specificity, are widely available and can be selected to bind theoretically to any given

target. However, for clinical translation, the use of antibodies is problematic due to the potential risk of immune reaction via antibody-dependent cell-mediated cytotoxicity (ADCC) (Moller 1967) and complement-dependent cytotoxicity (CDC) (Herlyn and Koprowski 1981). Moreover, antibodies are difficult to formulate and have a complex architecture of four polypeptide chains. Specific glycosylation patterns and presence of disulfide bonds require an eukaryotic system for the expression of the antibodies, which requires extensive optimization processes and makes the production costly and laborious (Skerra and Pluckthun 1988, Werner 2004). For these reasons, different low molecular weight binders have been developed to exceed these limits.

For instance, Lewis oligosaccharide derivates, such as sialyl Lewis X (sLe^x) have been proven to be successful in targeting P-and E-selectin on the endothelial cells (Klibanov 2005). Multitargeting using both sLe^x in combination with antibodies has been also shown to be feasible and improved MB adhesion (Weller, et al. 2005).

It has been already shown that MBs bearing nanobodies coupled with maleimide covalent binding to the microbubble surface can be used to detect VCAM-1 in large arteries (Punjabi, et al. 2019). With the use of this agent, early and late stage of stable atherosclerosis could be detected with CEUMI in an atherosclerotic mouse model (double knock out mice (DKO)).

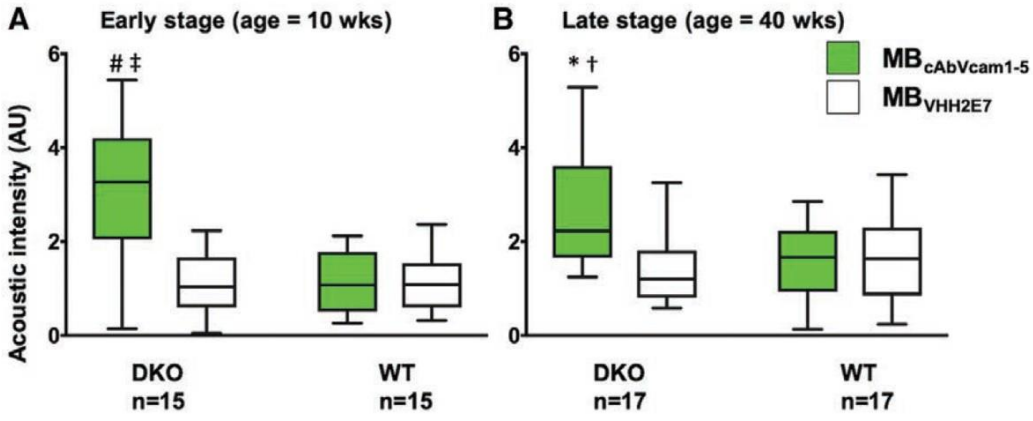

Figure 15: CEUMI signal intensity of the aortic arch injected with nanobody ($MB_{cAbVcam1-5}$) and control (MB_{VHH2E7}) in DKO mice and wild type mice (WT) at early and late stage atherosclerosis. Significant signal enhancement for $MB_{cAbVcam1-5}$ was observed in DKO mice at both ages.

Importantly, *ex vivo* CEUMI of human endarterectomy tissue was shown to be feasible in detection of VCAM-1 expression, along with CEUMI in murine aortic arch. These findings indicate a potential for clinical translation of the nanobody-coupled MBs for detection of early pathophysiological changes and refine risk stratification for atherosclerosis complications.

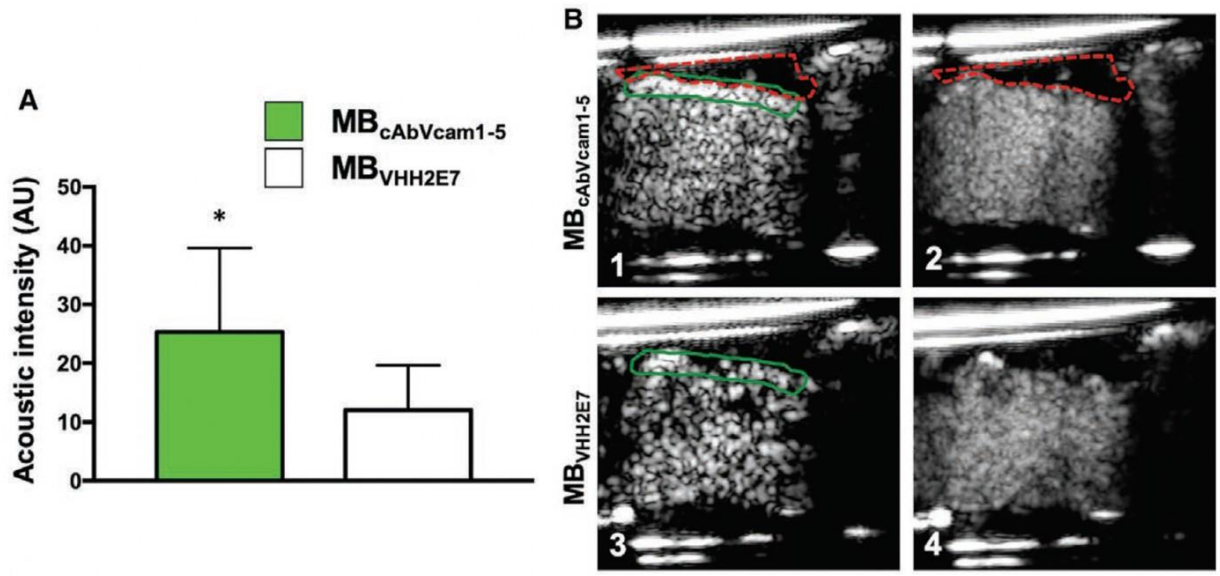

Figure 16: CEUMI of the expression of VCAM-1 in human thrombendarteriectomy specimen. A: Significant signal enhancement for $MB_{cAbVcam1-5}$ compared to MB_{VHH2E7} could be observed. Data is mean ± SD. B: Example of CEUMI showing single pre-destruction image fames (1 and 3) and the average post-destruction image frames (2 and 4). Human thromboendarterectomy specimen is shown in red, region of interest in green, drawn for deriving acoustic intensity from microbubbles attached to the endothelium.

In vitro selection techniques have been developed, such as ribosomal or phage displays (will be discussed in 2.3.3 in greater detail), in order to select binders without immunization. Following these, peptide scaffolds with desired customized properties are being engineered to overcome the shortcomings of antibodies (Binz, et al. 2005, Hosse, et al. 2006, Skerra 2007, Zahnd, et al. 2007). These high-affinity binders can be selected from a large library and screened against a given target. Several classes of them, including DARPins (see section 2.2), have recently been developed and represent high economic potential. Small peptide binders can be easily and inexpensively produced in bacterial culture, which offers an additional advantage over antibodies. Recent studies show that microbubbles bearing small peptide binders on their surface can be used for imaging of platelets and inflammatory cells *in vivo* (Moccetti, et al. 2018).

1.11.2. Conjugation strategies for binding targeting ligands to contrast agents for CEUMI

A ligand can be conjugated to the microbubble shell surface through different strategies. Very often a PEG spacer is included in the formulation of the microbubble shell in order to create distance between the microbubble and the ligand and therewith support ligand-target interaction. The length of the PEG spacer can affect the targeting efficiency (Khanicheh, et al. 2012). Nevertheless, in some cases such exposed ligands can be recognized by the immune system, this has resulted in a development of buried-ligand architecture, where ligands are conjugated to shorter PEG-arms, surrounded by longer

PEG spacer without ligands. However, this buried ligand architecture decreases ligand-target interaction and acoustic radiation force needs to be incorporated into imaging algorithms in order to bring the ligand close enough to its target (Borden, et al. 2013).

For the conjugation of the ligand to the PEG arm, biotin-streptavidin linkage is commonly used in preclinical research. Though being extremely practical and robust, it is impossible to use this strategy for clinical applications due to the potential immunogenicity of streptavidin. For this reason, other strategies have been developed that make use of the creation of covalent bonds between the ligand and the MB. For instance, a maleimide moiety agent on the end of the PEG spacer can be used to conjugate a ligand bearing a cysteine in its structure (Kirpotin, et al. 1997). Conjugation is facilitated thorough formation of a stable thioether bond. This strategy also allows for a site-specific conjugation of the proteins, as a cysteine can be inserted into in a controlled position (often used are C- and N-termini). For example, in the work of Punjabi et.al, nanobodies were coupled to the microbubbles through maleimide chemistry, which together with the advantages of nanobodies themselves makes these contrast agents potentially clinically translatable. N-Hydroxysuccinimide (NHS) binding is a further covalent conjugation strategy. In this reaction an NHS on the PEG spacer binds to primary amines of the proteins (such as lysine) under the formation of amide bonds and offers an undirected binding strategy compared to the maleimide conjugation (Klibanov 2005). Click-chemistry can as well be utilized for ligand attachment, using strain-promoted alkyne-azide cycloaddition click reaction. In this approach an azadibenzocyclooctyne group is introduced to a microbubble surface and then bound to an azide group on the desired ligand (Liu, et al. 2018).

1.11.3. Requirements for CEUMI contrast agents

For successful CEUMI, a number of requirements should be fulfilled concerning the targeting ligand and the target itself (Figure 17, (Steinl and Kaufmann 2015). As the targeting with MBs is limited to the vascular compartment due to their size and inability to extravasate, molecular targets should be expressed on the surface of endothelial cells. To image extravascular epitopes, other kinds of contrast agents could potentially be used, such as phase change contrast agents or nanobubbles. The target should be specific for a certain disease and the levels of its expression should differ significantly compared to the constitutive expression levels in the absence of disease. The target should be present of the surface of endothelial cells in sufficient density to the ensure for maximal microbubble attachment (Weller, et al. 2002). Also, the targeting ligand should be conjugated to a contrast agent in maximal surface density and should be highly specific and selective for a given target, so that off-target events are minimized.

Binding kinetics is of high interest in any biologic ligand-target interaction system and is described by rates of spontaneous association (on-rate, k_{on}) and dissociation (off-rate, k_{off}). A targeting ligand that is suitable for CEUMI should have a high affinity to the target, have a high on-rate to facilitate quick binding under flow conditions in the circulation and a low off-rate to ensure for maximal attachment time allowing for the imaging procedure. The on- and off-rates of a ligand are especially important when imaging in large arteries, where shear forces are the highest due to high blood flow velocity and it is crucial for the ligand to bind quickly to its target. In the microvasculature the blood flow is slower and the ligands have more time to bind their target.

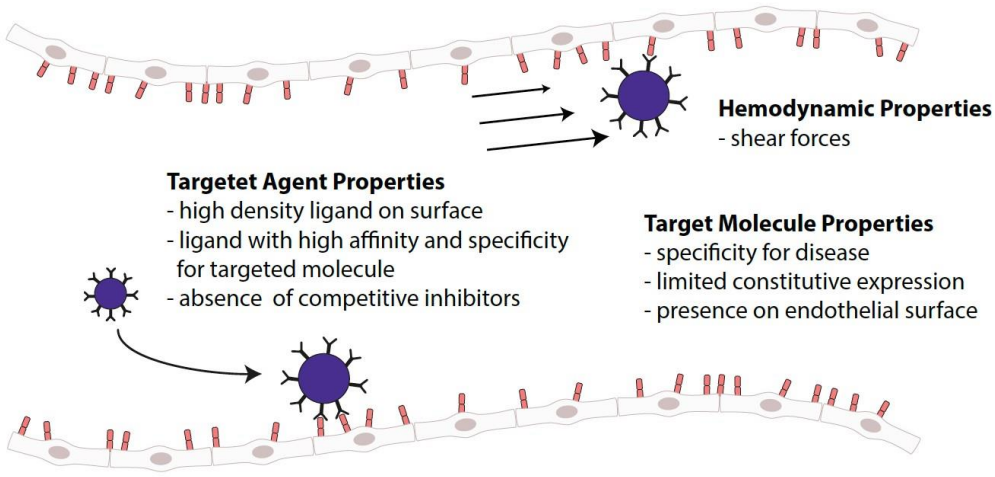

Figure 17: Requirements for the target and targeting ligand for a successful CEUMI. Picture from Steinl and Kaufmann 2015).

Antibodies that are widely used in preclinical research and CEUMI are known to have slow attachment rates (low k_{on}) and slow detachment rates (low k_{off}). They have been successfully used in imaging of microvasculature in skeleton muscles, kidneys and microvasculature of myocardium, where shear stress is around 3-5 dynes/cm^2 (Lindner, et al. 2001, Kaufmann, et al. 2007). Nevertheless, antibody conjugated contrast agents are known to allow for an effective targeting in mouse aorta, where peak shear rate is around 80-90 dynes/cm^2 (Greve, et al. 2006). This fact can be explained by the pulsatile nature of the blood flow in the aortic arch, where the blood velocity is close to zero in diastole. This time is sufficient for the antibodies to bind their target and thanks to low detachment rates, stay on the target even at high shear rates. A targeting ligand with a quick on-rate and a quick off-rate would be therefore not suitable for imaging in the aortic arch, but could be used for imaging in the microvasculature, where the flow speed is much slower.

1.11.4. Imaging of Targeted Signal

A standard protocol for CEUMI is to inject a bolus of several millions of targeted MBs and allow for attachment of the contrast agent to the target for 5-10 minutes. Due to MB uptake by the liver, gas loss and disintegration, a fraction of the MBs will be destroyed during the circulation time. After 5-10 minutes, images are recorded of both attached and circulating microbubbles, followed by a series of short high-power destruction pulses in the region of interest in order to destroy all of the attached microbubbles. After that the region of interest will be replenished with circulating microbubbles and the images of circulating microbubbles only are acquired. A typical imaging procedure is schematically represented in Figure 18. During image analysis, a digital subtraction of pre- and postdestruction images is done, resulting in a signal coming from only the attached microbubbles. In one imaging session several contrast agents can be injected sequentially, which allows for imaging of several targets during one measurement (Lindner, et al. 2001). As the targeting efficiency is relatively low, it is impossible to occupy all the binding sites on the endothelial cells. Therefore, it is possible to target the same kind of molecule for multiple times without a signal decay (Streeter and Dayton 2013).

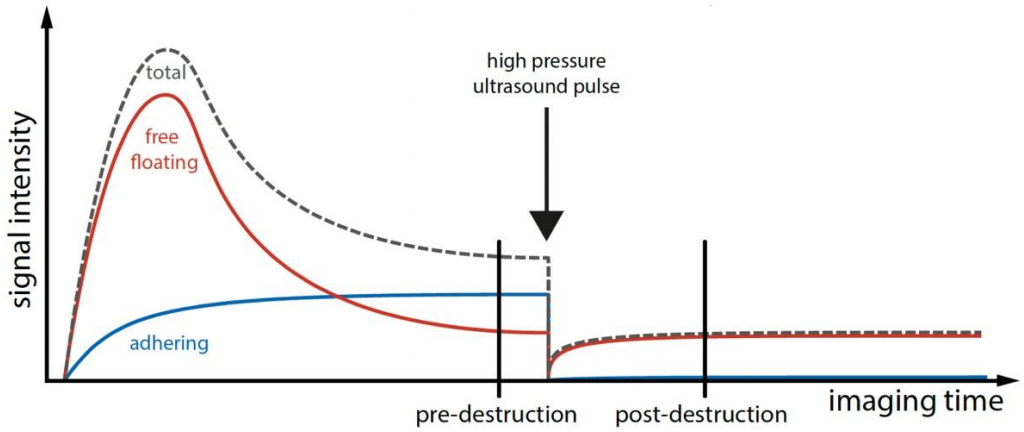

Figure 18: Schematic representation of a typical protocol for CEUMI of the targeted signal. A bolus injection of MBs is injected. After 8 minutes of circulation time images of attached and circulating MBs are recorded, attached MBs are then destroyed and the images of circulating MBs are recorded. Signal of the attached MBs is obtained by digital subtraction of post-destruction from pre-destruction images. Picture from (Steinl and Kaufmann, 2015).

2. Alternative scaffold protein binders

As mentioned above, although being extremely effective, antibodies have several drawbacks, which makes clinical translation challenging. To overcome these limitations, several strategies have been implemented so far.

One strategy is to use antibody fragments instead of full-size antibodies, which makes it possible to produce the fragments in a prokaryotic expression system. For instance, F_v fragments consist of variable regions from heavy and light immunoglobulin (Ig) chain. Unfortunately, the limited stability of the F_v fragments led to an introduction of stabilizing disulfide bond (dsFv), which lowered the yield of production or a linkage peptide (scF_v), which introduced additional sterical complications during the binding to the epitope (Glockshuber, et al. 1990). Other drawbacks of F_v fragments, such as low folding efficacy during expression in *E.coli,* as well as high aggregation probability, limited their application. Another more robust antibody fragment is F_{ab}. This fragment consists of a complete light chain, bound to a variable and CH1 domains of the heavy chain. Being easy and fast in synthesis (recombinant synthesis or enzymatic cleavage from whole antibody (Solomon, et al. 1978)), it still has a number of limitations, such as lower affinity to the target, compared to antibodies, susceptibility to denaturation and presence of immunogenic regions (Nelson and Reichert 2009). Overall Fab is still limited in its clinical application. A further class of antibody fragments, nanobodies, which consist from a single variable domain of the heavy chain (V_H) has been recently developed and successfully used for CEUMI (Hernot, et al. 2012, Punjabi, et al. 2019). They are derived from heavy-chain-only antibodies, which are present only in camelids. Having hydrophobic surfaces, nanobodies are not prone to aggregation and do not cause CDC though the F_c fragment. Moreover, they can be easily produced in prokaryotic and eukaryotic cells in large scale, can be modified in a site-directed manner and share a degree of sequence homology (>80%) with human V_H.

Taken together, antibody fragments have been developed to overcome the limitations of the antibodies. However, unsolved technical limitations still exist when considering stability, folding, aggregation and rapid evolution to recognize the target of interest. These facts underline the necessity of development of alternative protein scaffolds in order to enable straightforward and innovative applications.

Protein scaffolds appeared as a versatile tool for efficient target binding, as they are thermodynamically stable and do not require posttranslational modifications or disulfide bridges. The most prominent are four big classes of scaffold proteins: Adnectins, Affibodies, Anticalins and DARPins

(Rosenberg 2015). This work will be focusing on the application of DARPins as alternative protein scaffold binders.

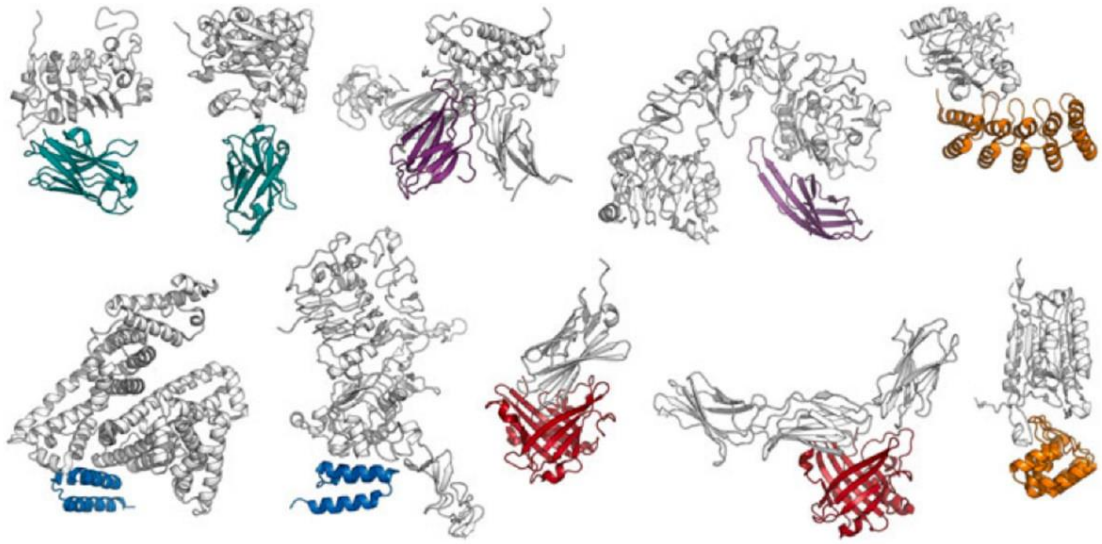

Figure 19: Structures of different single domain antibody fragments and protein scaffolds. Nanobody in complex with EGFR and ricin (green), Adnectin with IL23 and EGFR (violet), DARPin with HER2 (orange), Affibody with albumin and HER2, Anticalin with CTLA-4 and ED-B (red), DARPin with caspase-2 (orange). Picture from (Rosenberg 2015).

2.1. Repeat Proteins

Repeat proteins are naturally occurring protein classes (at least 14% of all proteins) that are particularly efficient in binding other proteins. They are distinguished by non-overlapping regions that share significant sequence similarity. Repeats allow for the formation of an elongated protein scaffold with a continuous binding surface that can be varied in length depending on the number of repeats. There are three main groups of repeat structures: α-structure, β-structure, and a mixed α/β-structure, including leucine rich repeats and ankyrin repeats (Kobe and Deisenhofer 1994, Sedgwick and Smerdon 1999, Andrade, et al. 2001). The beneficial qualities of the repeat proteins have been successfully used to engineer libraries of different repeat proteins, the most promising of which are DARPins.

2.2. Designed Ankyrin Repeat Proteins (DARPins)

DARPins are composed of tightly assembled repeats of usually 33 amino acids. Each repeat is built of a β-turn, which is followed by two antiparallel α-helixes and are connected to a β-loop through a short loop. A protein usually consists of 4-6 repeat units that together form a right-handed solenoid structure with a hydrophobic core and a hydrophilic surface, accessible for solvents (Kobe and Kajava 2000, Tamaskovic, et al. 2012). The first and the last repeat (N-capping repeat or N-cap and C-capping repeat

or C-cap) compose the hydrophilic outside surface and therefore stabilize the protein, as the hydrophobic core is protected from the surface (Binz, et al. 2003). In this way respective repeats are held together by hydrophobic interactions in the core of the protein. The structure of one repeat and a whole DARPin with three internal repeats is represented in Figure 20A.

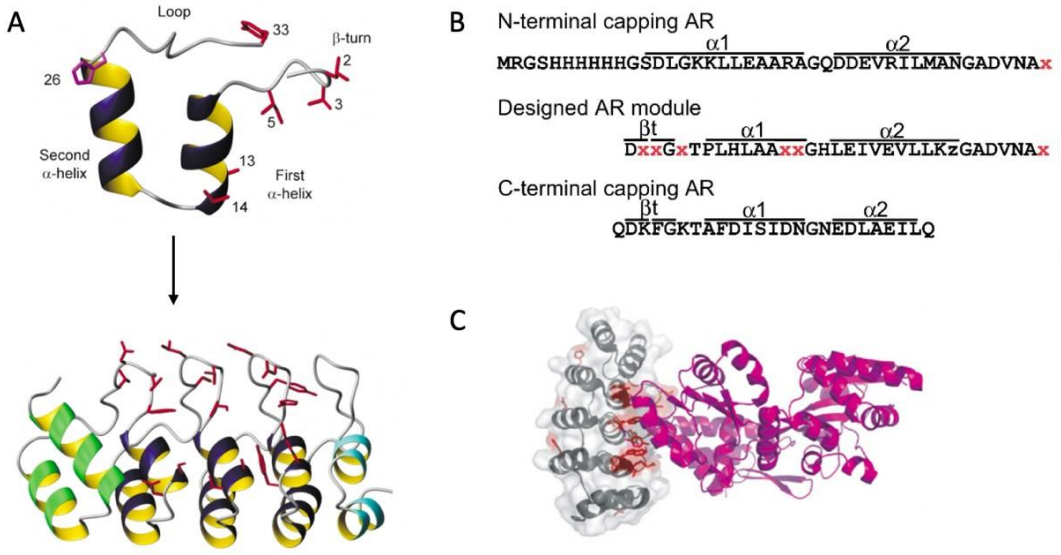

Figure 20: Structure of DARPins. A: Structure of middle ankyrin repeat module, consisting of two antiparallel α-helixes and a β-turn. Variable residues are shown in red, partially randomized residue is shown in magenta. Middle repeats are combined and flanked by N-and C-terminal capping repeats. B: Sequence of a capping repeats and a designed repeat module. C: Crystal structure of a DARPin in complex with maltose binding protein (MBP). Three repeat modules involved in binding can be seen. Pictures A and B from (Binz, et.al. 2003), picture C from (Stumpp, et al. 2008).

A consensus strategy was employed by Binz.et.al., a procedure based on sequence alignments and structural analyses, which led to combinatorial libraries of DARPins of varying sizes (repeat numbers) with fixed and variable positions. Consensus design means that functionally important residues that are involved in maintaining protein folding are usually conserved, while residues involved in target binding are not conserved (Forrer, et al. 2004). Each repeat consists of 27 framework residues (26 are fixed and one can be either asparagine, histidine or tyrosine) and 6 are variable (can be any aminoacids except cysteine, glycine and proline) (Figure 20B). Both introduction of N- and C-terminal repeats and implementation of a consensus strategy make DARPins highly thermodynamically stable, with stability increasing with the length of the protein. DARPins can be produced unproblematically in *E.coli* in large quantities and their expression and purification are straightforward. Studies indicate a high stability of DARPins even during boiling or guanidine hydrochloride exposure, which are known denaturation conditions (Wetzel, et al. 2008, Wetzel, et al. 2010).

An advantage of creating large libraries is the vast diversity of potential binders, which could recognize different epitopes of the target and can be screened in customized assays for a certain application. In this way one the best binder can be chosen and optimized for given conditions and easily produced.

Compared to antibodies that offer only one structure, a vast variety of binders can be created from large DARPin libraries. The theoretical diversity of DARPin libraries is 5.2 x 10^{15} and 3.8 x 10^{23} for two- or three-repeat binders respectively and the real library sizes are equal to the number of different molecules present and are estimated to be around 10^{12} in the ribosome display (Tamaskovic, et al. 2012). From these potential libraries, different DARPins have been already generated to recognize targets with high affinity and high potential for biomedical applications, such as DARPin binder for human immunodeficiency virus (HIV) gp120, epithelial cell adhesion molecule (EpCAM), amyloid-β peptide, vascular endothelial growth factor A (VEGF-A) and human epidermal growth factor receptor 2 (HER2) (Zahnd, et al. 2007, Stefan, et al. 2011, Mann, et al. 2013, Stahl, et al. 2013, Hanenberg, et al. 2014). DARPins show a high potential to be used in tumour targeting due to their small size (15-18 kD), high affinities and the ability to penetrate tumour tissue. For instance, a DARPin binder against HER2 has been designed to bind and inactivate HER2 homodimers. Abicipar pegol is a DARPin-based drug directed to bind all VGEF-A isoforms, which was developed to treat age-related macular degeneration (AMD). Recent results from a Phase III clinical trial showed its non-inferiority against ranibizumab, which is the treatment of choice till date, with less frequent injections. These findings make Abicipar pegol to a promising long-acting anti-VEGF-A treatment of AMD (Moisseiev and Loewenstein 2019). Moreover, with clinical application in mind, DARPins are well suited to be used in different types of fusion products and conjugates and can be potentially used as well in drug delivery and diagnostic detection systems. As DARPins lack cysteines, this allows for the introduction of a terminal cysteine for site-directed conjugation.

2.2.1. Selection Technologies for DARPin Libraries

The introduction of mutations and natural selection during evolution have resulted in a vast variety of organisms. In an attempt to assimilate this process for protein engineering, directed evolution of the protein sequence and structure is attempted to be reached through artificial selection strategies. To ensure for successful artificial directed evolution, two parameters should be combined: genotype (nucleotide sequence) and phenotype (functionality). This has been attempted though diverse *in vivo* selection techniques, such as two-hybrid (Karimova, et al. 1998), phage (Smith 1985), bacterial (Francisco, et al. 1992), yeast displays (Boder and Wittrup 1997) and mammalian display (Beerli, et al. 2008). However, those techniques, which require microbial cells are limited in the number of cells that can technically be transformed and it becomes impossible to work with large libraries. To overcome this problem, *in vitro* selection technologies have been developed, where selection occurs in a cell-free environment. The most prominent are mRNA (Roberts and Szostak 1997), ribosomal display (Hanes and Pluckthun 1997) and SNAP technology (Kaltenbach and Hollfelder 2012). For SNAP

technology a protein of interest is expressed with a SNAP-tag, which is the commercial name for the DNA protein ATG (O^6-alkylguanine DNA alkyltransferase), used as a protein tag. Ribosomal display offers additional advantages of controllable polymerase chain reaction (PCR) error-prone randomization steps for affinity maturation and allows for a directed evolution process.

Ribosomal display is based on the formation of ternary complexes (up to 10^{12} are possible), consisting of a ribosome, mRNA and a respective peptide, that are used for selection (Figure 21). The library of DARPins is inserted into a plasmid with all the necessary sequences for selection, such as T7 promoter for transcription *in vitro*, a Shine-Dalgarno sequence for ribosome attachment, stem loop regions at 5' and 3'-ends for protection of the mRNA from degradation and a tolA spacer sequence that allows the peptide to exit the ribosomal tunnel. The mRNA lacks a stop codon, so that nascent peptide chain is not released from the ribosome. Sequencing of mRNA contained that were eluted allows to determine the sequence of the candidate ligands.

Any given DARPin library is first transcribed from DNA to mRNA and then translated *in vitro*. After translation the ternary complexes are incubated with the immobilized target in a panning step, which can occur in different ways, and the unbound complexes are washed away. The remaining ternary complexes are dissociated and mRNA is reversely transcribed to cDNA. Resulting cDNA is amplified by PCR and again cloned into an expression plasmid for further selection rounds or into expression vector for better characterization. As polymerase inserts errors in the sequences during PCR, an affinity maturation step takes place, which allows for greater sequence diversity. Usually, DARPins with pM to nM affinities can be identified after several rounds of selection.

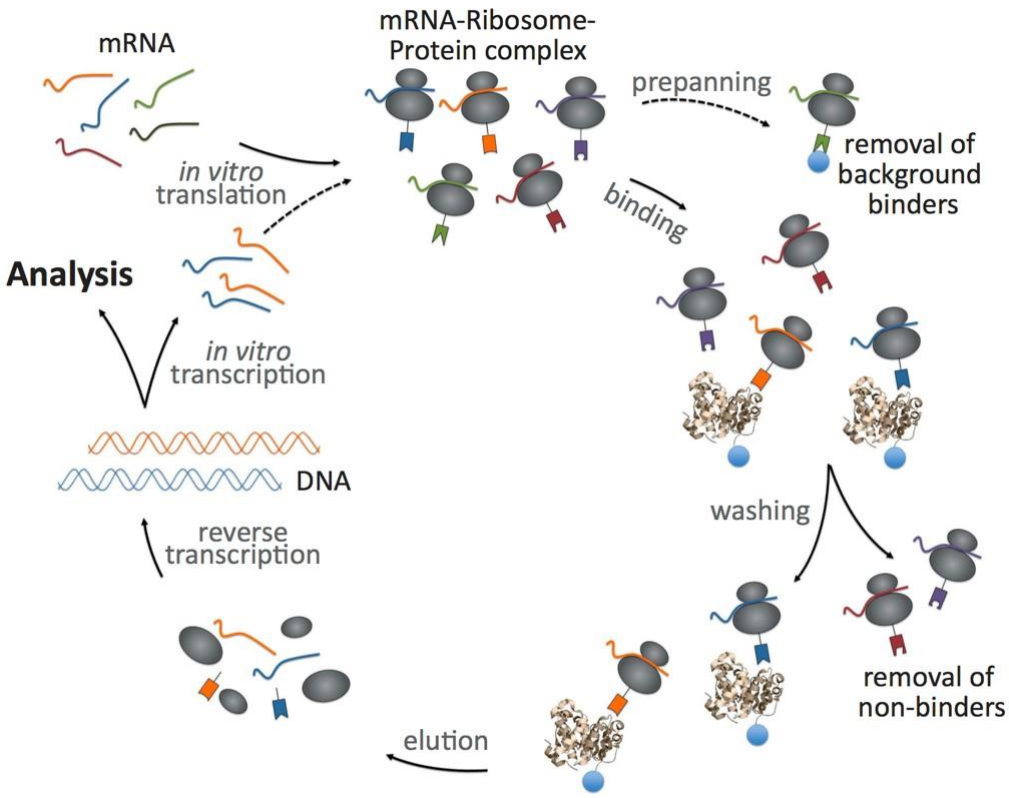

Figure 21: Schematic representation of the ribosomal display selection of DARPin binders. From DNA library, mRNAs are obtained. After translation, mRNA-ribosome-Protein complexes (ternary complexes) are used for affinity selection on the immobilized target. After removal of background binders (prepanning) and non-binders (panning), mRNAs are eluted, reverse transcribed into DNA and amplified by error-prone PCR. Resulting DNAs, representing the selected pool of binders can be used for further ribosome display rounds or cloned into expression vectors and analyzed. Picture from Jonas Schaefer, with permission.

3. Vascular cell adhesion molecule 1 (VCAM-1) as a target for CEUMI

VCAM-1 (CD106) is a 90-kDa glycoprotein (Rice and Bevilacqua 1989) that is predominantly expressed on the surface of endothelial cells upon activation of different extracellular stimuli, such as reactive oxygen species and pro-inflammatory cytokines (Cook-Mills, et al. 2011). During inflammation VCAM-1 serves for the firm adhesion of leukocytes to the vascular wall and serves as a prominent target in the research of inflammatory disorders. Moreover, there is increasing evidence of VCAM-1 being an important regulator of angiogenesis during would healing, ischemia and tumor growth, which makes VCAM-1 to an attractive target in these research areas as well. In this section the role of VCAM-1 in endothelial inflammation and as a special case of it, atherosclerosis, and angiogenesis will be highlighted.

3.1. Endothelial inflammation

The normal endothelium forms an interface between the vascular space and the organs of the body and serves as a barrier to maintain the integrity of the vessel. Under normal physiological conditions, endothelial cells do not enter into close contact with leukocytes circulation in the blood flow. Also, endothelial cells are produce vasoactive compounds, such as nitric oxide (NO) and prostacyclin (PGI_2), which help to maintain vascular tone and have anti-aggregatory effects (Nadia R. Sutton 2014). Without inflammatory stimuli, immune cells are passing by the endothelium in a rolling manner are not recruited as there is no need for an immune answer (Figure 22).

However, when encountering an inflammatory stimulus, such as cytokines, injury, circulating immune complexes, toxins or ischemia, endothelial cells and tissue resident innate immune cells are activated, which results in recruitment of leukocytes to the site of inflammation. Initial leukocyte attachment occurs due to the interaction of adhesion molecules on the surface of endothelial cells, E- and P-selectins with the respective counter ligands on leukocytes (Borregaard, et al. 1994). Selectins are a class of long adhesion receptors that protrude beyond the glycocalyx and interact with sialylated glycoproteins (E-selectin ligand 1 (ESL-1) and P-selectin glycoprotein ligand-1 (PSGL-1)) that are constitutively expressed on leukocytes (Ley 2003). This results in leukocyte rolling, which is transient and reversible. During rolling, the leukocytes cells are exposed to cytokines and chemokines that are released as a reaction to an inflammatory stimulus. Upon activation of the NF-κB signaling pathway (Barnes and Karin 1997), which is a mediator of the most inflammatory vascular responses, a number of genes are upregulated that encode for cytokines, such as Interleukin-6 (IL-6), tumor necrosis factor-

α (TNF-α), interleukin-1β (IL-1β) and chemokines, such as CXCL1 (Olson and Ley 2002, Bazzoni, et al. 2009). The released cytokines bind receptors on the endothelial cells and cause upregulation of the endothelial adhesion molecules (ECAMs), such as intercellular adhesion molecule 1 (ICAM-1) and VCAM-1 and upregulation of their counter ligands, integrins, on the surface of leukocytes (Springer 1990, Ley 1996). Upregulation of ICAM-1 and VCAM-1 has been shown to occur as early as 4 hours after the release of TNF-α and is involved in recruitment of monocytes-/macrophages to sites of inflammation (Fries, et al. 1993). A number of factors are responsible for transmigration of leukocytes out of the vessel, such as the adhesion molecule platelet/endothelial cell adhesion molecule 1 (PECAM-1) and coordinators of gap junction opening (JAMs and VE-Cadherin) (Muller 2011).

In addition, an alternative inflammation pathway, called thrombo-inflammation, has been recently described. During this process, von Willebrand factor (vWF)-mediated platelet adhesion participates in endothelial activation and leukocyte adhesion. Thus, platelet adhesion and vWF related signaling can be considered as markers for endothelial inflammation (Jackson, et al. 2019).

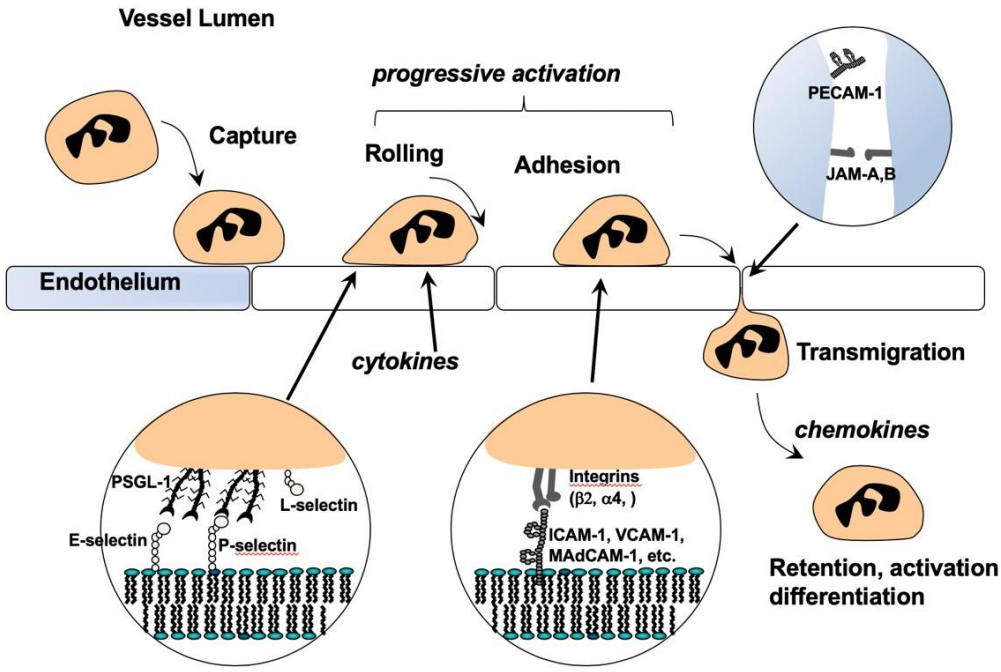

Figure 22: Schematic representation of endothelial inflammation. Initial leukocyte recruiting and rolling are facilitated mainly though interactions between selecting and PSGL-1-like receptors. Rolling enables subsequent firm attachment of leukocytes through adhesion molecules (VCAM-1, ICAM-1 etc.). Adhesion allows for cytokine exposure and transmigration of the leukocytes into the tissue. Picture from (Kosareva, et.al. 2019).

3.2. CEUMI of microvascular inflammation

For CEUMI, a wide range of adhesion molecules can be used as targets to detect microvascular inflammation. The most prominent ones are ECAMs, such as VCAM-1, ICAM-1 and mucosal addressin cell adhesion molecule 1 (MAdCAM-1). Leukocytes that have been recruited to the vascular wall during inflammation, can be also used as targets for CEUMI. For instance, monocyte population can be targeted by using C-X-C motif chemokine receptor 1 (CXCR-1) (Ryu, et al. 2013), T-lymphocytes populations – using CD3 or CD4 (Steinl, et al. 2016) and granulocytes – using complement receptors (Mott, et al. 2016). Microvascular inflammation can be also detected by targeting P-selectin in a mouse model of hind limb inflammation (Khanicheh, et al. 2012).

CEUMI of microvascular inflammation is possible in almost every tissue in different pathological inflammatory conditions. Clinical care could benefit greatly from the advances of CEUMI in terms of disease monitoring and early diagnostics in a number of fields and pathologies:

Acute coronary syndrome (ACS) describes a number of conditions associated with sudden reduction of blood flow to the heart. In symptomatic patients the diagnosis is often challenging, because it relies on clinical history, laboratory evaluation and electrocardiogram (ECG), all the factors, which are often non-diagnostic. To overcome this limitation, CEUMI of ischemia-related inflammation was developed for detecting ACSs (Kaufmann, et al. 2007, Villanueva and Wagner 2008, Davidson, et al. 2014). It was already performed in rodent and non-human primate models of myocardial ischemia-reperfusion by targeting selectins, which are rapidly upregulated in response to ischemia. Different ligands were successfully used for this purpose, such as monoclonal antibodies, sLe^x and recombinant forms of PSGL-1.

CEUMI of microvascular inflammation has also been shown to be feasible in models of allograft transplantation and myocarditis (Steinl, et al. 2016). To date, biopsy remains a gold standard for assessment for rejection in clinics. CEUMI allows for non-invasive imaging of ICAM-1 (Weller, et al. 2003) and T-cells (Wu, et al. 2013) for the assessment of the inflammatory status of the allograft. Similarly, detection of the inflammatory infiltrate of the myocardium during myocarditis is possible and is more sensitive than imaging of the functional consequences of myocarditis such as ejection fraction or wall motion defects.

IBD is a chronic inflammatory condition, marked by regular inflammatory disruption of gastrointestinal function. The disease often begins asymptomatic and becomes evident at later stages, so that early

diagnosis and monitoring is needed. Monitoring of the inflammatory bowel disease (IBD) is possible in mouse models in IBD using microbubbles against MAdCAM-1 and ECAM, involved in gut lymphocyte adhesion and provides a potential for later clinical use (Bachmann, et al. 2006).

3.3. Atherosclerosis

Atherosclerosis is a progressive inflammatory disease of the large arteries (Lusis 2000), which is characterized by of lipid accumulation and chronic inflammation of the vessel wall (Figure 23). It progresses silently over several decades before resulting in severe cardiovascular complications, such as stroke or myocardial infarction. Therefore, there is a clinical need for imaging methods to detect the early stages of atherosclerosis with the aim to better risk stratify patients.

The first observable change of the artery wall during atherosclerotic plaque formation is the deposition of low-density lipoprotein-cholesterol (LDL) in the intima at the sites of lesion predisposition. There, LDL subsequently undergoes oxidation (oxLDL) due to the increased oxidative stress in the vascular wall, which is often caused by cardiovascular risk factors, such as smoking, diabetes, hypertension, lack of physical activity, obesity and hypercholesterolemia (Witztum and Steinberg 1991, Kunsch and Medford 1999, Stocker and Keaney 2004). The presence of reactive oxygen species and oxLDL creates a pro-inflammatory environment in the vascular wall and leads to a number of changes of the endothelial cell surface through activation of the NF-κB signaling pathway. The uptake of oxLDL by monocytes or macrophages leads to their conversion to foam cells and intensifies the inflammatory process and atherosclerotic plaque growth.

During the early atherogenic process, vascular cell adhesion molecule 1 (VCAM-1) is massively expressed on the surface of endothelial cells. VCAM-1 serves to recruit monocytes into the vascular wall by interacting with its counter-ligand integrin α4:β1 (Bevilacqua 1993). This makes VCAM-1 a perfect diagnostic target for detecting early vascular inflammation during the development of atherosclerosis.

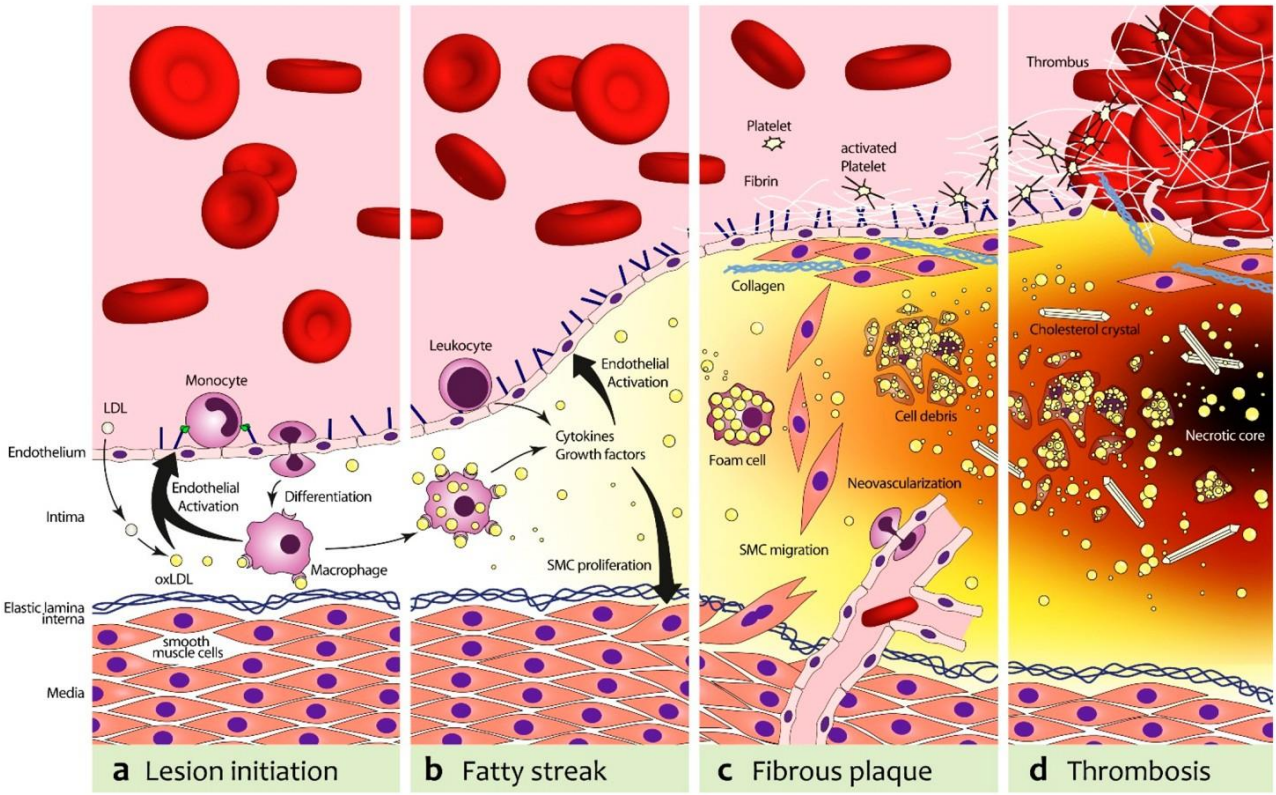

Figure 23: Schematic representation of atherosclerotic progression. A: LDL get deposited in the endothelium, undergo oxidation (oxLDL). As a result, endothelial cells are stimulated to overexpress adhesion molecules (VCAM-1, P-selectin etc.) and recruit monocytes and macrophages. Macrophages then transmigrate into the intima and differentiate to pro—atherogenic macrophages. B: Macrophages phagocytize oxLDL and transform to foam cells, expression of adhesion molecules facilitates leukocyte adhesion and expression of inflammatory cytokines. C: The increasing plaque formation promotes neovascularization; proliferation of smooth muscle cells stabilizes the plaque. D: Foam cells undergo apoptosis and together with accumulated oxLDL and cholesterol crystals form the necrotic core of the plaque. Proteases released from foam cells can destabilize the plaque. This can cause plaque rupture and subsequent thrombotic events.

3.4. CEUMI of Atherosclerosis

Non-invasive targeted imaging of the expression of endothelial cell adhesion molecules with the ultimate goal of detecting early stages of atherosclerosis and thus allow for risk stratification has been studied extensively in preclinical studies. Both VCAM-1 and P-selectin are expressed very early in the course of atherosclerotic disease progression and enabled CEUMI of these targets in the aortic arch of murine atherosclerosis models using monoclonal antibodies (Kaufmann, et al. 2007) and nanobodies (Punjabi, et al. 2019) at the initial fatty streak stage. Compared to imaging in the microvasculature, one should consider high shear stress conditions in large arteries for the imaging of atherosclerosis and therefore pay special attention to increasing targeting efficiency of the contrast agents that are being used. It has been shown that by delivering NO with ELIPs and subsequent imaging of ICAM-1 with ELIPs lead to signal increase. This effect is probably due to increased vascular permeability in

response to NO and increased accumulation of ELIPs within plaques (Kee, et al. 2014). Also, in non-human primate models of diet-induced obesity CEUMI of VCAM-1 and P-selectin were shown to be feasible (Chadderdon, et al. 2014). Apart from its diagnostic use, CEUMI can be used for assessing drug effects on vascular inflammation and is therefore well suited for pre-clinical testing of novel drug candidates (Khanicheh, et al. 2013, Khanicheh, et al. 2013).

3.5. Angiogenesis and arteriogenesis

Angiogenesis is a process by which new blood vessels form from pre-existing ones. Angiogenesis is associated with a number of pathologic conditions, such as cancer, would healing and ischemia (Folkman 1993). It is regulated by a number of upregulated pro-angiogenic factors, with VEGF being the key regulator (Leung, et al. 1989, Hoeben, et al. 2004, Potente, et al. 2011). Arteriogenesis is another mechanism of vessel formation and is characterized by the formation of mature arteries through the remodeling of poorly perfused interconnecting arterioles after an occlusion by formation of collateral vessels that restore blood flow downstream (Cai and Schaper 2008).

There is increasing evidence that VCAM-1 is associated with tumor angiogenesis. VCAM-1 positive tissues in gastric cancer have been associated with greater microvessel density (Ding, et al. 2003), also VCAM-1 serum levels correlate with microvessel density in breast cancer (Byrne, et al. 2000), and could serve as a surrogate biomarker of tumor angiogenesis. In the study of Garmy-Susini et al. it has been shown that VCAM-1 and integrin α4β1 are expressed on the developing vessels in breast cancer and the administration of anti-VCAM-1 antibody (M/K-2) reduced vessel formation in Matrigel plug mouse models (Garmy-Susini, et al. 2005). Recently the IG-like domain of VCAM-1 was identified as a potential angiogenic target for the modulation of TNF- α induced angiogenesis (Kong, et al. 2018).

4. Aims of the Project

VCAM-1 has been characterized as a prominent biomarker for molecular imaging in a number of pathologic conditions, such as microvascular inflammation, atherosclerosis and angiogenesis. Previous studies have shown that CEUMI using microbubble contrast agents directed against VCAM-1 is feasible in murine disease models. However, the ultrasound contrast agents used in these studies are not suitable for clinical translation, and there is a need for the development of microbubbles employing (a) clinically translatable strategies for conjugation of targeting moieties, and (b) targeting ligands that can readily be used in the clinical field. DARPins are a novel class of single domain binders, which can be selected from a large library to bind any given target with high affinity and specificity. They are attractive for applications in molecular imaging, as they are highly specific, non-immunogenic and thus offer the potential for clinical translation.

Given the importance of the detection of VCAM-1 expression, the overall goal of this work is to develop and validate novel VCAM-1 targeted microbubbles with clinically translatable DARPin binders coupled to the microbubble surface using maleimide covalent bonding.

The main objectives of this work were to 1) select DARPin binders recognizing VCAM-1 from a large library, 2) select high affinity DARPin binders with *in vitro* assays, 3) validate the functionality of the selected high affinity DARPin binders in a mouse model of a) hind limb inflammation and b) mouse model of an early and late stage atherosclerosis.

5. Methods

5.1. Selection of high-affinity DARPin ligands from crude bacterial extracts

5.1.1. Ribosomal Display (RD)

In the current study N2C and N3C DARPin libraries (N-terminal capping repeat, two or three internal repeats and C-capping repeat (Binz, et al. 2003)) were used for the ribosomal display to select DARPin binders targeted against murine VCAM-1 as described (Dreier and Pluckthun 2011). The extracellular domain of the VCAM-1 (Met1-Glu698, Sino Biological, China) was used as a target protein. The target was biotinylated and immobilized and on streptavidin-coated magnetic beads (MyOne T1 streptavidin-coated beads (Pierce)). Two strategies of biotinylation were performed: NHS-biotinylation using EZ-link NHS-LC-LC-Biotin (Thermo Scientific) and BirA biotinylation using BirA-500: BirA biotin protein ligase standard reaction kit (Avidity), with biotinylation efficiency being 70% for both strategies. Four iterative rounds of RD in solution with decreasing target concentration and increasing number of washing steps to enrich for binders with high affinities were performed. Target-bound ternary complexes, consisting of ribosomes, mRNA and translated polypeptide, were pulled down with the help of magnetic beads and the non-bound complexes were washed away. Target-bound ternary complexes were eluted and the obtained mRNAs were reversely transcribed and cloned into a bacterial pQIq-based expression vector as fusion with a N-terminal $MRGSH_8$-and C-terminal FLAG tag. After transformation in *E.coli* XL1-blue, 384 individual DARPin clones were expressed in a 96-well format and lysed by addition of Cell lytic B reagent (Sigma), Lysozyme and Pierce nuclease, resulting in crude bacterial extracts, having single clones of DARPins each.

5.1.2. Homogeneous time resolved fluorescence (HTRF)

Initial screening of DARPins obtained from RD for their VCAM-1 target binding properties was performed with the help of HTRF assay in 384-well plate format with the crude bacterial extracts of DARPin binders. HTRF is an established method for high-throughput screening, where the fluorescence resonance energy transfer technology (FRET) principle is used to achieve time resolved, robust and sensitive detection of protein-protein interactions. The emissions are measured at two wavelengths: 620 nm (donor) and 655 nm (acceptor). The close proximity of donor and acceptor, which indicates binding of DARPin and target, takes place, the emission at 620 nm shifts to 655 nm and therefore increases the ratio of the respective signals. The time-resolved measurement allows for the elimination of short-lived non-specific signal. In this assay crude bacterial extracts containing Flag-tagged DARPins were fluorescently labeled and tested upon binding biotinylated fluorescently labeled VCAM-1 by measuring the FRET signal (donor: streptavidin-Tb, acceptor: anti-FLAG-d2, Cisbio). An unselected

library member E3_5 was used as a negative control, an off7 DARPin specifically binding Maltose Binding Protein (MBP) was used as a positive control. With this method 19 binders were selected, which showed a higher signal over background. A background signal was set by using reagents only.

5.1.3. Cell-based saturation binding assay

In parallel to HTRF, 384 crude bacterial extracts of binding candidates, identified with the RD were screened for their target binding properties in a cell-based saturation binding assay. For this purpose, bEnd.3 mouse endothelial cells (ATCC CRL-2299, obtained at passage 25) were grown to confluency (cell culture medium: ATCC-formulated DMEM (ATCC 30-2002)) and stimulated with recombinant TNF-α (10 mg/ml) over night (for 18 hours) for VCAM-1 expression. Passage numbers 28 or 29 were taken for the measurements, as it is reported for bEnd.3 cells to express VCAM-1 before passage 30 after TNF-α stimulation. The cells were trypsinised and resuspended in HBSS with 1% BSA for blocking the unspecific binding. Cells were then incubated with the different crude DARPin extracts for 30 minutes at 4°C on a rocking table. Biotinylated positive (rat anti-mouse CD-106, clone 429, BD Pharmingen) and negative (kappa isotype clone R35-95, BD Pharmingen) control antibodies, as well as the unselected library member E3_5 control DARPin were used. DARPins were detected with a FITC-labeled anti-FLAG secondary antibody (anti-FLAG-M2-FITC, Sigma) and the antibodies were detected with FITC-labeled streptavidin (Leinco Technology). Afterwards cells were washed 3 times with PBS by adding 100 µl of PBS and centrifuging the cells for 6 min at 125 g at 4°C. Subsequently, the cells were stained with a viability dye (Zombie, Biolegend), washed 3 times with PBS again and fixed with 4% formaldehyde (Alfa Aesar). Afterwards a flow cytometrical analysis was performed (CytoFLEX, Beckman Coulter).

For the gating strategy, an arbitrary isotype control threshold of 10% positively stained cells was defined (Figure 24). All cells below this threshold were considered to be non-specifically labeled. Affinity was expressed as percentage of events above the threshold (% of VCAM-1 positive cells).

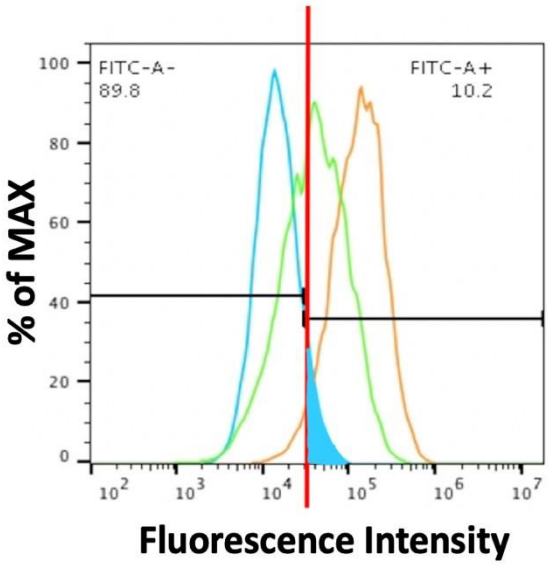

Figure 24: Gating strategy for cell-based assays.

The crude extracts were diluted 1:20 in order to obtain the binders that show a high signal also at a low concentration. After the first round with a cut-off of 25% of VCAM-1 positive cells, 77 binders were selected for further screening. In the second round, the 77 best candidates were screened at a 1:200

dilution in a binding assay. Again, a 25% of VCAM-1 positive cells cut-off was used and 21 binders were selected. These binders were combined with the 19 binders from the HTRF. Eight binders had been selected with both assays. Taken together, a total of 32 binders were selected after the combination of both assays.

5.1.4. Sequence analysis

All 32 candidates were purified and sequenced. Sequencing data then revealed that 8 of them were polyclonal (having a mixture of plasmids after transformation) and two of them appeared to be identical, these candidates were therefore excluded from further analysis. The remaining 23 candidates were expressed in small scale and purified with a 96 well IMAC column (HisPur™ Cobald plates, Thermo Scientific). After the purification DARPins were analyzed with regards to their monomeric state on a Superdex 75 5/150 L column at a concentration of 10 µM (GE healthcare) on an Äkta Micro system (GE Healthcare) with PBS containing 400 nM NaCl as the running buffer. Absorbance was recorded at 280 nm. β-amylase (200 kDa), bovine serum albumin (66 kDa), carbonic anhydrase (29 kDa) and cytochrome c (12.4 kDa) were used as molecular mass standards. After purification, all DARPins were identified to be predominantly monomeric, so it was possible to proceed with further measurements.

In the next step the binding assay was repeated with purified DARPins at a low concentration of 800 pM in order to select the best binders. A cut-off of 20% VCAM-1 positive cells was set and 6 high affinity binders were selected for further characterization (1731-F9, 1732-F8, 1730-E12, 1732-D1, 1730-C7 and 1731-H9).

5.2. Large scale expression and purification

Large scale expression of the 6 DARPin candidates was performed at a 200 ml scale. A cysteine was added to the C-terminal of the DARPin structure for the maleimide conjugation to the MB surface (a cloning strategy is shown in Figure 25). After induction with 1 mM Isopropyl beta-D-1 thiogalactopyranoside (IPTG) and incubation for 4 hours, expression cultures were harvested by centrifugation for 10 min at 4000 rpm. The cell pellet was resuspended in PBS 400 mM NaCl, 10% glycerol, 5mM DTT and 20 mM imidazole adding Pierce Universal nuclease and cells were lysed using sonication. DARPins were purified over a HisTrap FF crude column (GE Healthcare) and desalted over a HiTrap 26/10 Desalting column (GE Healthcare) using an Äkta PURE L1 system (GE Healthcare). Purity was determined by 12% SDS-PAGE and size exclusion chromatography. 1731-H9 DARPin candidate showed aggregation propensity and was therefore excluded from the selection. The remaining 5 binders were clearly monomeric according to analysis.

Figure 25: Cloning strategy of 6 respective DARPins into a new expression vector. A DARPin sequence is inserted between BamHI (not shown) and HindIII restriction sites. A terminal cysteine was added to the sequence.

5.3. Saturation binding assay of DARPin candidates

In order to characterize 5 selected DARPin binders in terms of their affinity to the target, a saturation binding experiment was performed. Experimental procedure was identical to the "cell-based affinity assay", which is described above in section 5.1.3. In this experiment, a concertation range of DARPins of 50pM to 100 nM was used. Equilibrium binding constant (K_d) and maximal specific binding (B_{max}) were determined. Non-specific binding was subtracted by applying the gating strategy mentioned above.

5.4. Microbubble production

MBs were produced by sonication of a decafluorobutane-saturated aqueous suspension of 1,2-distearoyl-sn-glycero-3-phosphocholine (2mg/ml, Avanti), polyoxyethylene (40) stearate (1mg/ml, Sigma) and 1,2-Distearoyl-sn-glycero-3-phosphoethanolamine-maleimide (0.14mg/ml, Creative PEGWorks). MBs were washed 3 times by floatation centrifugation for 1 min at 1200 rpm at room temperature to wash out lipid molecules that were not integrated in the shell. MBs were always produced freshly for each experiment, their size and count were determined using a Multisizer III (Beckman Coulter).

5.5. Conjugation of DARPins to the microbubbles

5.5.1. Conjugation strategy

For further experiments, DARPin binders need to be conjugated to the MB surface (Figure 26, Figure 27). DARPins were conjugated to the MBs through a C-terminal cysteine on the DARPin to the maleimide on the MB surface (MB_{DARPin}). Control MBs bearing an unselected isotype DARPin E3_5 were also prepared ($MB_{control}$).

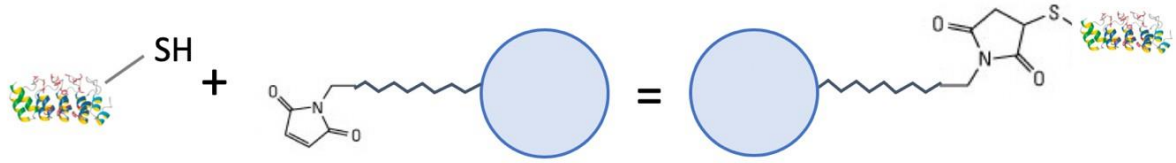

Figure 26: Schematic representation of conjugation of the C-terminal cysteine (sulfhydryl group) on the DARPin to the maleimide on the MB, thus forming a stable thioether bond. Protein structure from (Binz et al. 2004).

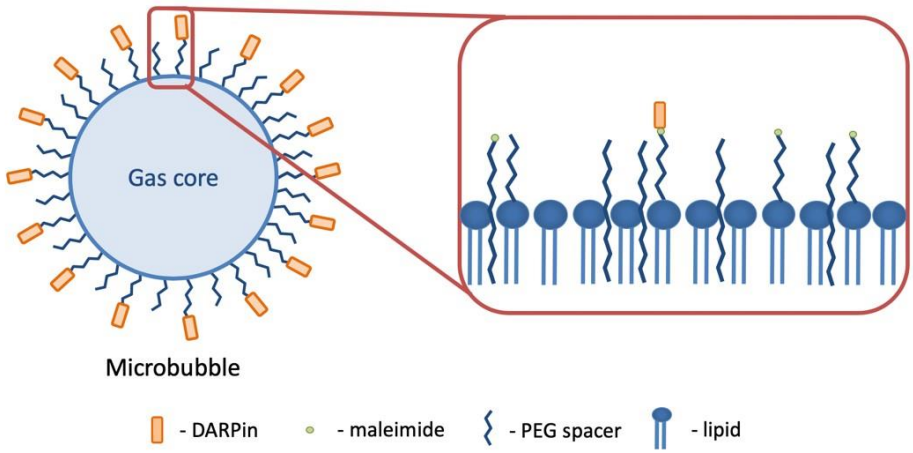

Figure 27: Schematic representation of the MB structure and the conjugation strategy of the DARPins. A DARPin molecule is conjugated to the MB through the C-terminal cysteine, which binds to the maleimide on the microbubble surface.

5.5.2. Determining the optimal conjugation amount of DARPins to the microbubbles

In order to determine the amount of DARPins necessary to saturate the maleimide binding sites on the surface of microbubbles, $1x10^8$ microbubbles were incubated with different amounts of fluorescently labeled DARPins (0 µg, 20 µg, 40 µg, 80 µg, 100 mg, 120 µg, 150 µg and 200 µg) for 2 hours at room temperature. After three washing steps by floatation centrifugation, the fluorescence signal from microbubbles was acquired by flow cytometry (CytoFLEX, Beckman Coulter).

5.5.3. Fluorescence microscopy

In order to verify the presence of the DARPins on the MB surface and validate the chosen conjugation strategy of binding C-terminal cysteine on the DARPin to the maleimide on the MB surface, fluorescence microscopy was employed. First, DARPin 1731-F9 was labeled with Alexa488-NHS according to the manufacturer (Thermo Scientific, 10 mg/ml) instructions. Next, 120 µg of fluorescently labeled 1731-F9 were conjugated to 1×10^8 microbubbles for 2 hours at room temperature. After 3 washing steps, microbubbles were imaged. In order to exclude the possibility of fluorescent tag binding extensively to the microbubble surface and thus causing false positive fluorescent signal on the images, 2 µl of Alexa488-NHS without DARPins was incubated with $1x10^8$ microbubbles, the microbubbles were then washed for 3 times.

Last, in order to further validate the presence of DARPins on the microbubble surface, an excess of unlabeled 1731-F9 (400 µg) was incubated with 1×10^8 microbubbles, to saturate the binding sites, for 2 hours at room temperature and then washed three times. After washing steps, 5×10^7 microbubbles remained and were incubated with 60 µg of Alexa488-1731-F9 for 2 hours at room temperature, washed 3 times and imaged.

5.5.4. Determining the surface density of DARPins on the microbubbles

To determine the number of DARPins conjugated to the MB surface, quantitative fluorescence analysis was employed. For that purpose, 1×10^8 MBs were incubated with 120 µg of fluorescently labeled DARPins or the isotype control DARPin for 2h at room temperature. To remove the unbound material, MBs were washed three times by floatation centrifugation. MB concentration and mean surface area were measured using a Multisizer III (Beckman Coulter). The MBs were destroyed by applying pressure (100 mm Hg). The concentration of the dissolved DARPins was then measured using Gemini XPS fluorescence microplate reader (Molecular Devices) by comparing the fluorescent signal to a fluorescently labeled reference standard of known DARPin concentration. The DARPins density per surface area was then calculated using the information from Multisizer measurements. All measurements were done in triplicates.

5.6. Flow chamber studies

Parallel plate flow chamber experiments were used to assess the specific attachment of MB_{DARPin} to VCAM-1 under flow conditions. Cell culture dishes (35mm×10mm, Corning) with bEnd.3 (ATCC® CRL2299™) murine endothelial cells grown to confluence were used. One plate as used for every individual measurement. Four hours prior to the measurement, the cells were induced with

recombinant TNF-α (50 ng/ml, R&D Systems) to express Vcam-1. The culture plates were mounted on a parallel plate flow chamber (GycoTech Inc, gasket thickness: 0.254mm and channel width: 2.5mm) and put in an inverted position on a microscope (Olympus BV51W). A fluorescent dye DIO (3,3' Dioctadecyloxacarbocyanine perchlorate, 0.1mg/ml, Sigma Aldrich) was additionally included in the formulation of the microbubble shell to enable efficient visualization, MBs were drawn through the flow chamber with a syringe pump (Genie plus, Kent Scientific) at a concentration of 3×10^6 MB/ml.

5.6.1. Flow chamber studies at continuous flow

For the measurements with continuous flow, suspensions of MB_{DARPin} or $MB_{control}$ were drawn through the flow chamber with a syringe pump at a constant flow rate resulting in a shear stress of 2 or 4 dynes/cm^2 (1 dyne = 10^{-5}N). After five minutes of continuous flow, the number of microbubbles attached to the endothelial cells, was counted for 20 optical non-overlapping fields using fluorescence microscopy digital recordings (Olympus BX51WI equipped with a CCD camera, 40x magnification).

5.6.2. Determining the on-rate of the DARPins: pulsatile flow

To study the attachment behavior (on-rate) of different MB_{DARPin} and $MB_{control}$ in conditions that mimic the flow in the aortic arch, pulsatile flow experiments were conducted. The shear rate was set to 8 dynes/cm^2 initially and periodically reduced to 0-0.5 dynes/cm^2 for 5 seconds for 4 times. A video recording of 20 optical non-overlapping fields was done at baseline (B) and after each flow reduction (P1, P2, P3 and P4).

5.6.3. Determining the off-rate of the DARPins: detachment characteristics

To study the detachment characteristics of MB_{DARPin} and $MB_{control,}$ MBs were drawn through the flow chamber at a shear rate of 0.5 dynes/cm^2 for 5 minutes to allow for the maximum attachment. Afterwards, the flow was sequentially increased to 40 dynes/cm^2 in 5 dynes/cm^2 steps every 30 seconds and 20 optical non-overlapping fields were recorded after each shear rate increase to assess MB attachment.

5.7. Animal preparation

All animal experiments were performed in accordance with Swiss Federal Legislation and approved by the local Animal Care and Use Committee of the University Hospital of Basel and the ethics committee of the Veterinary Office of the Canton of Basel. For echocardiography and CEUMI, mice were

anesthetized with inhaled isofurane and maintained with 1-1.5% inhaled anesthesia (isofurane in room air). A heating pad was used to keep the body temperature at 37°C. Jugular vein cannulation (PE50 tubing) was performed for administration of MBs. For CEUMI, animals were transferred to a temperature-controlled imaging stage (Vevo Imaging Station). The heart rate was monitored.

5.8. CEUMI of hind limb inflammation mouse model

In order to validate binding efficiency of $MB_{DARPins}$ to VCAM-1 *in vivo*, a mouse model of microvascular inflammation was used, which is a well-established method to induce the expression of VCAM-1. Shear stress in the hind limb microvasculature is 2-4 dynes/cm^2 and is therefore comparable to the shear stress in the flow chamber experiments with continuous flow. Hind limb inflammation was caused in C57BL/6 wild type male mice maintained on chow diet 15-21 weeks of age (n=13) by intramuscular injection of 250 ng of recombinant TNF–α (Khanicheh, et al. 2012). Four hours after injection, VCAM-1 is expressed on the surface of endothelial cells in the microvasculature. Animals were maintained on 1.5% inhalation isofurane anesthesia during the four hours of TNF-α induction of VCAM-1 expression.

After four hours, a jugular vein was cannulated for MB administration and CEUMI (Sequoia Acuson C512; Siemens Medical Systems USA Inc., Mountain View, CA) was performed with a high-frequency linear-array probe (15L8) held in place by a railed gantry system. The short axis of the adductor muscle of the mouse hind limb was imaged. The gain settings were adjusted just below visible tissue speckle and held constant. 2×10^7 of the five candidate MB_{DARPin} (1731-F9, 1732-F8, 1730-E12, 1732-D1 and 1730-C7) as well as $MB_{control}$ were injected intravenously in random order while imaging was paused. After 8 minutes of circulation time, imaging was performed with power modulation and pulse inversion (Contrast Pulse Sequence) modes at a centerline frequency of 7 MHz, dynamic range of 50 dB and a high mechanical index of 0.87. In this imaging sequence, one imaging frame was recorded, in order to assess signal from MBs attached to the vascular wall within the microcirculation as well as circulating MBs. All MBs within the field of view were then destroyed by increasing the mechanical index to 0.87 using several image frames. Post destruction images (n=5) representing only the circulating microbubbles were acquired at a mechanical index of 0.87 at a long pulsing interval (10 seconds). Finally, anatomic images of the hind limb were acquired with fundamental imaging at 14 MHz to determine the region of interest. The signal from the attached MBs only was calculated by digitally subtracting the average signal of the post-destruction contrast frames from the average signal of the pre-destruction contrast frames. Image analysis was performed by an investigator blinded to MB species on the individual imaging sequences.

5.9. Atherosclerosis mouse model and experimental setup

This experiment aimed to assess the functionality of MB_{DARPin} in a patho-physiologically relevant disease model of atherosclerosis. Double knockout (DKO) mice with a knockout for LDL receptor and apolipoprotein B-48 (ApoB-48) on a C57BL/6 background were used. LDL receptor is a cell surface receptor on hepatocytes that binds to apolipoprotein E (ApoE) to clear it from the blood. LDL receptor also binds to LDL via interactions with ApoB to clear LDL from the circulation. ApoB exists in two isoforms in mammals: ApoB-48 and ApoB-100. It is known that mice lacking ApoB-48 have higher LDL and LDL-triacylglycerol blood levels (Farese, et al. 1996). The DKO mice used for this experiment, express only the ApoB-100 isoform and a truncated non-functional LDL receptor (unable to bind LDL). Overall, these mice quickly develop atherosclerotic plaques on a chow diet and are well suited to study cardiovascular pathologies. Models of early stage atherosclerosis (mice 10 weeks of age) and late stage atherosclerosis (mice 40 weeks of age) were used. Age-matched C57BL/6 wild type male mice on a chow diet were used as a negative control. The imaging procedure was similar to the hind limb inflammation model protocol. The ascending aorta including the sinus of Valsalva was imaged in a long axis. Mice were anesthetized and jugular vein was cannulated. Directly after cannulation, 1×10^6 of MB_{DARPin} (1732-F8, 1730-E12 and 1730-C7) as well as $MB_{control}$ were injected *i.v.* in random order while the imaging was paused. After 8 minutes of circulation time, imaging was resumed and one image at MI 0.87 was recorded. All MBs within the field of view were then destroyed by using several (>10) image frames at a mechanical index of 0.87. Post destruction images (n=5) representing only the circulating microbubbles were acquired at a long-pulsing interval (10 seconds). Finally, anatomic images of the ascending aorta and aortic arch were acquired with fundamental imaging at 14 MHz. The region of interest included the sinus of Valsalva, the ascending aorta and extended into the origin of the brachiocephalic artery. The signal from the attached MBs was calculated by digitally subtracting the average signal of the post-destruction contrast frames from the signal of the pre-destruction contrast frame. Image analysis was performed by an investigator blinded to MB species on the individual imaging sequences.

5.10. Statistical Analysis

Data were analyzed using GraphPad Prism version 8.0d (GraphPad Software. Inc., La Jolla, CA). Datapoints are expressed as mean ± SEM, unless stated otherwise. For saturation binding curves, curve fitting was carried out by nonlinear regression using a saturation binding model. For flow chamber with continuous flow and animal experiments, Kruskal-Wallis test with Dunn's post hoc multiple comparisons test was used, comparing each MB agent against the isotype. For flow chamber experiments with pulsatile flow, Friedman's test with multiple comparisons was used for comparing

the number of MBs at each flow reduction compared to the baseline. For flow chamber experiments examining detachment characteristics, Friedman's test with multiple comparisons was used to compare the number of attached MBs versus the baseline after each flow increase. P-values < 0.05 were considered statistically significant (2 sided).

6. Results

6.1. Selection of high-affinity DARPin ligands from crude bacterial extracts

6.1.1. HTRF Assay

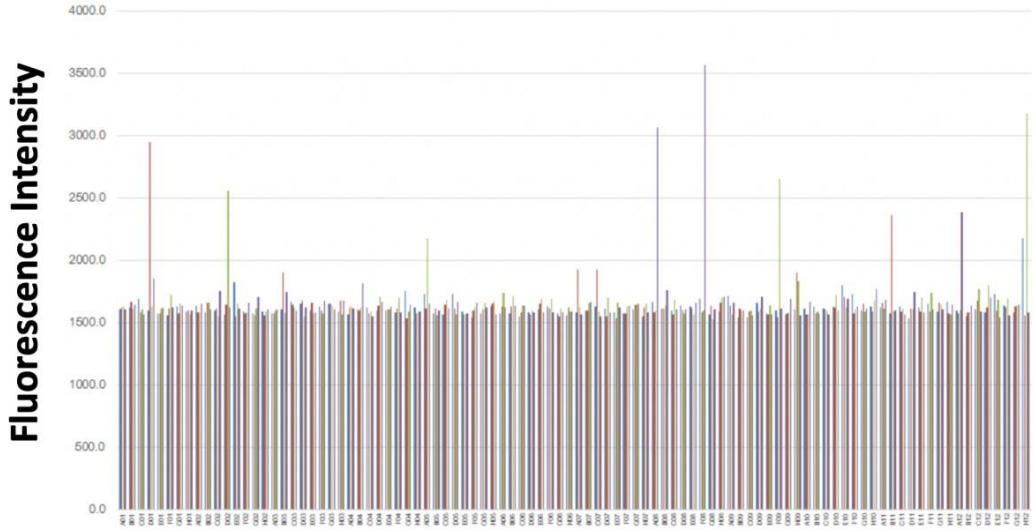

Figure 28: Homogenous Time Resolved Fluorescence (HTRF) assay of 384 clones from a DARPin library obtained after the fourth round of selection against the extracellular domain of recombinant VCAM-1. The name of each clone refers to its position on the plate. The values are represented in arbitrary florescence intensity units.

From HTRF, 19 high affinity DARPin binders were selected from 384 crude bacterial extracts of DARPin candidates identified in the ribosomal display (Figure 28). From this assay, all the binding candidates that showed a signal higher than the background were selected for further characterization.

DARPin	Fluorescent signal
1729_E02	1825.0
1729_E10	1795.9
1730_D01	2952.2
1730_B03	1898.2
1730_A07	1924.4
1730_C07	1927.8
1730_H09	1902.5
1730_B11	2365.5
1731_D02	2556.2
1731_A05	2172.6

DARPin	Fluorescent signal
1731_F09	2649.2
1731_H09	1833.9
1731_C12	1771.6
1731_D12	1799.8
1732_D01	1853.6
1732_B04	1812.8
1732_A08	3063.1
1732_F08	3567.7
1732_A12	2383.1
background	1566.0

Table 2: DARPins selected with HTRF. Fluorescent signal is expressed in arbitrary intensity units. The background signal was set by measuring the signal of the reagents only.

6.1.2. Cell-based flow cytometry assay

Crude extracts of the same 384 binding candidates, tested with HTRF, were tested for their target binding efficiency in a cell-based affinity assay. In the first step, 1:20 dilutions of the crude extracts were measured to exclude candidates with low target binding efficiency (Figure 29).

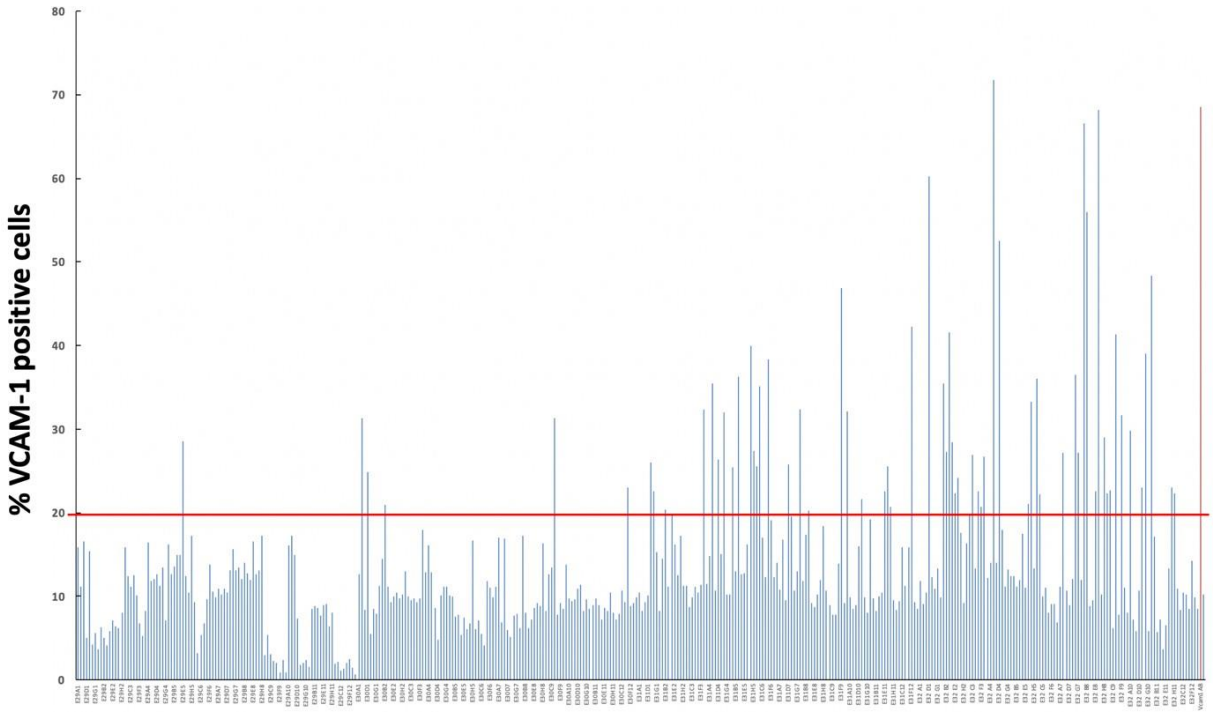

Figure 29: Affinity comparison of 384 binders to VCAM-1 in a cell-based assay, cut-off of 20% VCAM-1 positive cells was applied (red line). Crude bacterial extracts were diluted 1:20. The red bar represents the signal from a positive control antibody.

After application of a cut-off of 20% positively stained cells, 77 binders were selected. In the next step, crude extracts of this binders were measured again at a higher dilution of 1:200 to select high affinity binders (Figure 30).

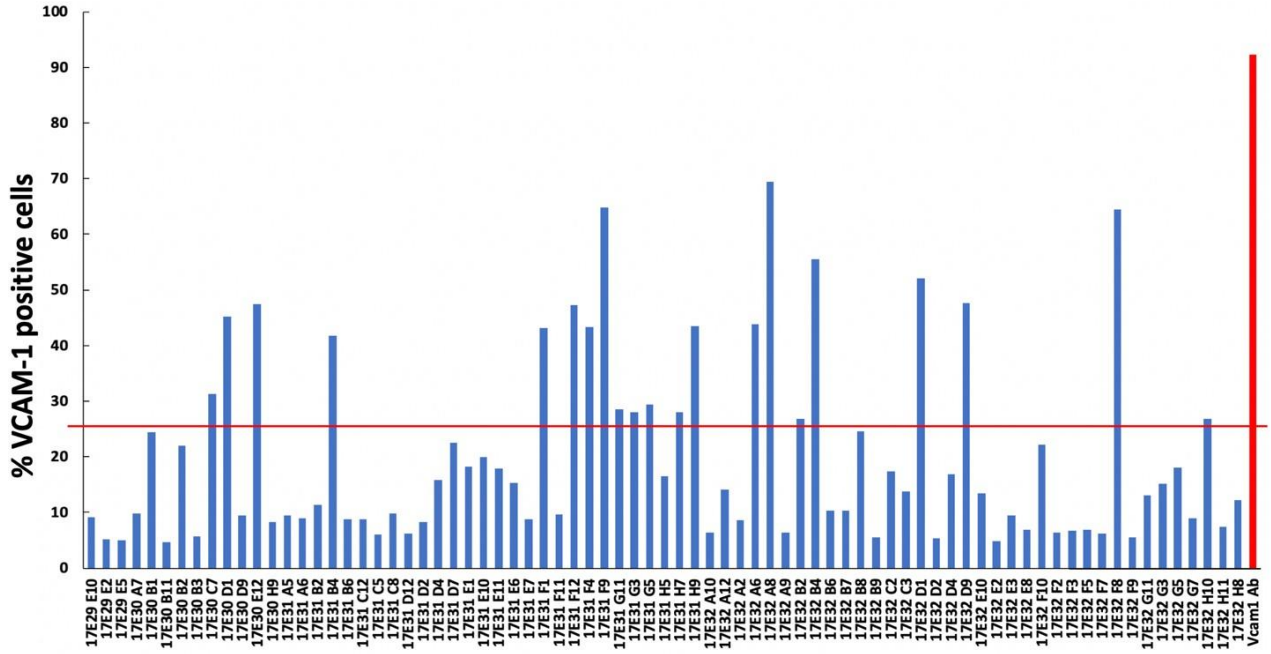

Figure 30: Affinity comparison of 77 binders to VCAM-1 in a cell-based assay, cut-off of 25% VCAM-1 positive cells was applied (red line). Crude bacterial extracts were diluted 1:200. The red bar represents the signal from a positive control antibody.

After application of a cut-off of 25% positively stained cells, 21 binders were selected. Those binders were then combined with 19 selected binders from the HTRF assay. 8 were identified with both assays, thus resulting in 32 binders after combining both assays (Figure 35).

6.1.3. Sequence Analysis

Sequences of the selected binders were analyzed using Sanger sequencing. As described in the methods section, two sequences showed identical amino acid sequence and therefore one was excluded from the pool of candidates. Eight candidates appeared to be polyclonal (bearing more than one plasmid after transformation and therefore more than one DARPin in the crude extract) and were also excluded from the pool (Figure 31). After excluding these sequences, 23 of 32 initial clones remained for further analysis and characterization. For the following analysis all the DARPin candidates were re-expressed and purified.

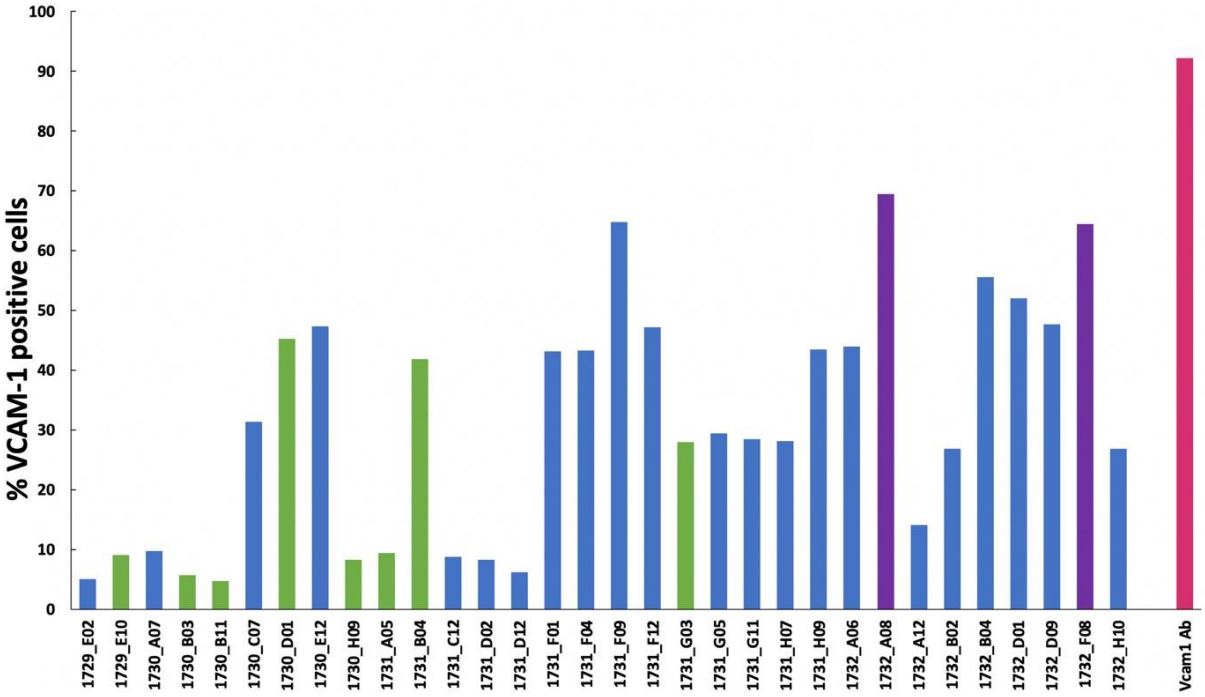

Figure 31: Sequence analysis of 32 selected DARPin candidates. Eight clones are polyclonal (green), two clones are identical (violet) and were excluded from the analysis. The red bar represents the signal from a positive control antibody.

A sequence alignment of the 23 selected DARPin binders was performed on Clustal Omega, showing that all the DARPins represented unique sequences (Figure 32).

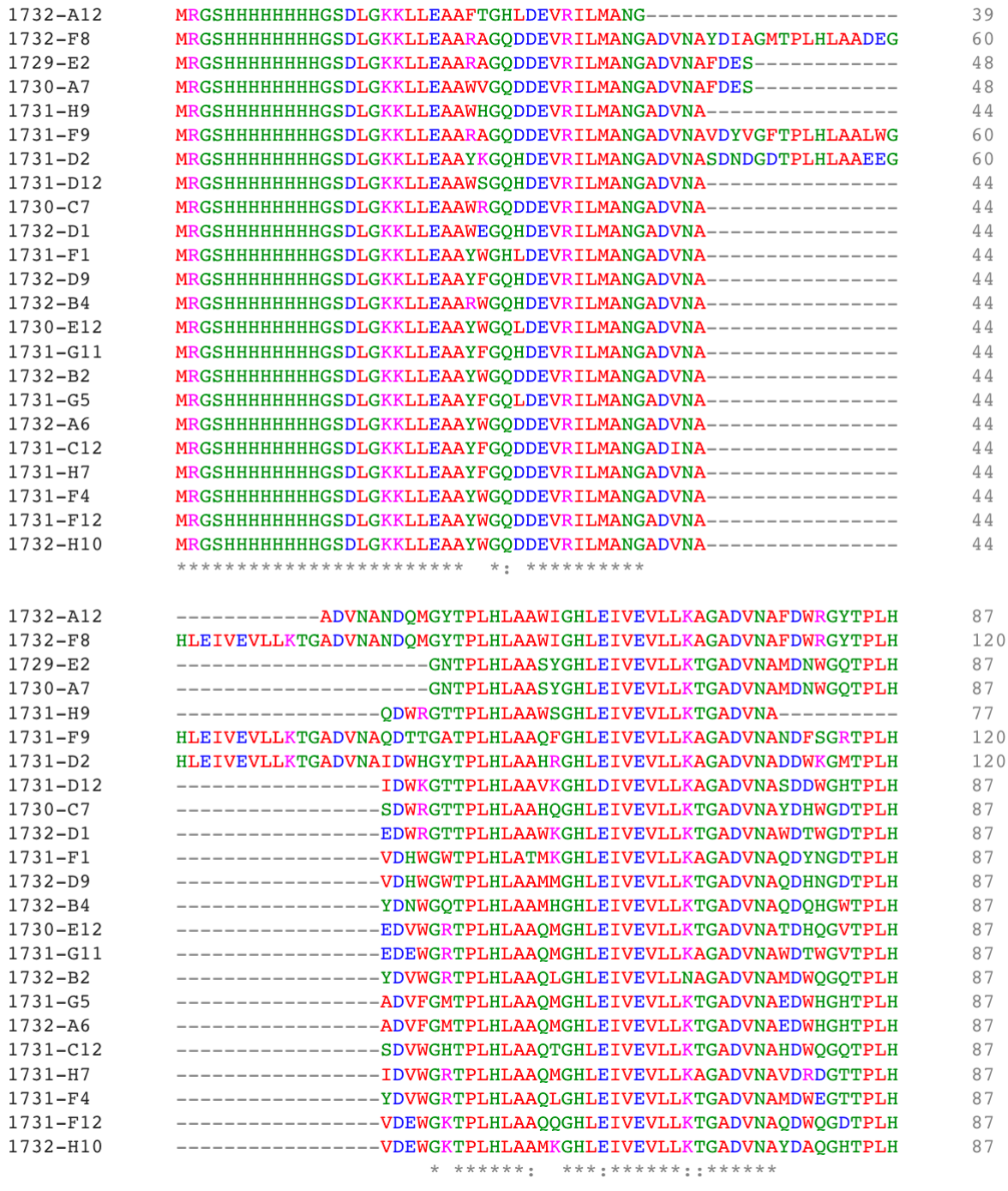
1732-A12 MRGSHHHHHHHHGSDLGKKLLEAAFTGHLDEVRILMANG---------- 39
1732-F8 MRGSHHHHHHHHGSDLGKKLLEAARAGQDDEVRILMANGADVNAYDIAGMTPLHLAADEG 60
1729-E2 MRGSHHHHHHHHGSDLGKKLLEAARAGQDDEVRILMANGADVNAFDES---------- 48
1730-A7 MRGSHHHHHHHHGSDLGKKLLEAAWVGQDDEVRILMANGADVNAFDES---------- 48
1731-H9 MRGSHHHHHHHHGSDLGKKLLEAAWHGQDDEVRILMANGADVNA---------- 44
1731-F9 MRGSHHHHHHHHGSDLGKKLLEAARAGQDDEVRILMANGADVNAVDYVGFTPLHLAALWG 60
1731-D2 MRGSHHHHHHHHGSDLGKKLLEAAYKGQHDEVRILMANGADVNASDNDGDTPLHLAAEEG 60
1731-D12 MRGSHHHHHHHHGSDLGKKLLEAAWSGQHDEVRILMANGADVNA---------- 44
1730-C7 MRGSHHHHHHHHGSDLGKKLLEAAWRGQDDEVRILMANGADVNA---------- 44
1732-D1 MRGSHHHHHHHHGSDLGKKLLEAAWEGQHDEVRILMANGADVNA---------- 44
1731-F1 MRGSHHHHHHHHGSDLGKKLLEAAYWGHLDEVRILMANGADVNA---------- 44
1732-D9 MRGSHHHHHHHHGSDLGKKLLEAAYFGQHDEVRILMANGADVNA---------- 44
1732-B4 MRGSHHHHHHHHGSDLGKKLLEAARWGQHDEVRILMANGADVNA---------- 44
1730-E12 MRGSHHHHHHHHGSDLGKKLLEAAYWGQLDEVRILMANGADVNA---------- 44
1731-G11 MRGSHHHHHHHHGSDLGKKLLEAAYFGQHDEVRILMANGADVNA---------- 44
1732-B2 MRGSHHHHHHHHGSDLGKKLLEAAYWGQDDEVRILMANGADVNA---------- 44
1731-G5 MRGSHHHHHHHHGSDLGKKLLEAAYFGQLDEVRILMANGADVNA---------- 44
1732-A6 MRGSHHHHHHHHGSDLGKKLLEAAYWGQDDEVRILMANGADVNA---------- 44
1731-C12 MRGSHHHHHHHHGSDLGKKLLEAAYFGQDDEVRILMANGADINA---------- 44
1731-H7 MRGSHHHHHHHHGSDLGKKLLEAAYFGQDDEVRILMANGADVNA---------- 44
1731-F4 MRGSHHHHHHHHGSDLGKKLLEAAYWGQDDEVRILMANGADVNA---------- 44
1731-F12 MRGSHHHHHHHHGSDLGKKLLEAAYWGQDDEVRILMANGADVNA---------- 44
1732-H10 MRGSHHHHHHHHGSDLGKKLLEAAYWGQDDEVRILMANGADVNA---------- 44
********************** *: **********
1732-A12 ----------ADVNANDQMGYTPLHLAAWIGHLEIVEVLLKAGADVNAFDWRGYTPLH 87
1732-F8 HLEIVEVLLKTGADVNANDQMGYTPLHLAAWIGHLEIVEVLLKAGADVNAFDWRGYTPLH 120
1729-E2 ----------GNTPLHLAASYGHLEIVEVLLKTGADVNAMDNWGQTPLH 87
1730-A7 ----------GNTPLHLAASYGHLEIVEVLLKTGADVNAMDNWGQTPLH 87
1731-H9 ----------QDWRGTTPLHLAAWSGHLEIVEVLLKTGADVNA---------- 77
1731-F9 HLEIVEVLLKTGADVNAQDTTGATPLHLAAQFGHLEIVEVLLKAGADVNANDFSGRTPLH 120
1731-D2 HLEIVEVLLKTGADVNAIDWHGYTPLHLAAHRGHLEIVEVLLKAGADVNADDWKGMTPLH 120
1731-D12 ----------IDWKGTTPLHLAAVKGHLDIVEVLLKAGADVNASDDWGHTPLH 87
1730-C7 ----------SDWRGTTPLHLAAHQGHLEIVEVLLKTGADVNAYDHWGDTPLH 87
1732-D1 ----------EDWRGTTPLHLAAWKGHLEIVEVLLKTGADVNAWDTWGDTPLH 87
1731-F1 ----------VDHWGWTPLHLATMKGHLEIVEVLLKAGADVNAQDYNGDTPLH 87
1732-D9 ----------VDHWGWTPLHLAAMMGHLEIVEVLLKTGADVNAQDHNGDTPLH 87
1732-B4 ----------YDNWGQTPLHLAAMHGHLEIVEVLLKTGADVNAQDQHGWTPLH 87
1730-E12 ----------EDVWGRTPLHLAAQMGHLEIVEVLLKTGADVNATDHQGVTPLH 87
1731-G11 ----------EDEWGRTPLHLAAQMGHLEIVEVLLKAGADVNAWDTWGVTPLH 87
1732-B2 ----------YDVWGRTPLHLAAQLGHLEIVEVLLNAGADVNAMDWQGQTPLH 87
1731-G5 ----------ADVFGMTPLHLAAQMGHLEIVEVLLKTGADVNAEDWHGHTPLH 87
1732-A6 ----------ADVFGMTPLHLAAQMGHLEIVEVLLKTGADVNAEDWHGHTPLH 87
1731-C12 ----------SDVWGHTPLHLAAQTGHLEIVEVLLKTGADVNAHDWQGQTPLH 87
1731-H7 ----------IDVWGRTPLHLAAQMGHLEIVEVLLKAGADVNAVDRDGTTPLH 87
1731-F4 ----------YDVWGRTPLHLAAQLGHLEIVEVLLKTGADVNAMDWEGTTPLH 87
1731-F12 ----------VDEWGKTPLHLAAQQGHLEIVEVLLKTGADVNAQDWQGDTPLH 87
1732-H10 ----------VDEWGKTPLHLAAMKGHLEIVEVLLKTGADVNAYDAQGHTPLH 87
* ******: ***:******::******

```
1732-A12        LAAKYGHLEIVEVLLKHGADVNAQDKFGKTPFDLAIDNGNEDIAEVLQKAAKLNDYKDDD      147
1732-F8         LAAKYGHLEIVEVLLKHGADVNAQDKFGKTPFDLAIDNGNEDIAEVLQKAAKLNDYKDDD      180
1729-E2         LAAKWGHLEIVEVLLKHGADVNAQDKFGKTPFDLAAWRGNEDIAEVLQKAAKLNDYKDDD      147
1730-A7         LAAKWGHLEIVEVLLKHGADVNAQDKFGKTPFDLAAWRGNEDIAEVLQKAAKLNDYKDDD      147
1731-H9         ----------------------QDYWGDTPFDLAAHVGNEDIAEVLQKAAKLNDYKDDD      114
1731-F9         LAAHWGHLEIVEVLLKHGADVNAQDKFGKTAFDISIDNGNEDIAEVLQKAAKLNDYKDDD      180
1731-D2         LAAKWGHLEIVEVLLKHGADVNAQDKFGKTPFDLAIDNGNEDIAEVLQKAAKLNDYKDDD      180
1731-D12        LAAAYGHLEIVEVLLKHGADVNAQDKFGKTAFDISIDNGNEDIAEVLQKAAKLNDYKDDD      147
1730-C7         LAATKGHLEIVEVLLKHGADVNAQDKFGKTPFDLAIDNGNEDIAEVLQKAAKLNDYKDDD      147
1732-D1         LAATTGHLEIVEVLLKHGADVNAYDKFGKTPFDLAIDNGNEDIAEVLQKAAKLNDYKDDD      147
1731-F1         LAAREGHLEIVEVLLKHGADVNAQDKFGKTAFDISIDNGNEDIAEVLQKAAKLNDYKDDD      147
1732-D9         LAAANGHLEIVEVLLKHGADVNAQDKFGKTAFDISIDNGNEDIAEVLQKAAKLNDYKDDD      147
1732-B4         LAAIFGHLEIVEVLLKHGADVNAQDKFGKTPFDLAIDNGNEDIAEVLQKAAKLNDYKDDD      147
1730-E12        LAAIEGHLEIVEVLLKHGADVNAQDKFGKTPFDLAIDNGNEDIAEVLQKAAKLNDYKDDD      147
1731-G11        LAAAEGHLEIVEVLLKHGADVNAQDKFGKTPFDLAIDNGNEDIAEVLQKAAKLNDYKDDD      147
1732-B2         LAAKEGHLEIVEVLLKHGADVNAQDYEGETPFDLAIDNGNEDIAEVLQKAAKLNDYKDDD      147
1731-G5         LAAAEGHLEIVEVLLKHGADVNAQDKFGKTAFDISIDNGNEDIAEVLQKAAKLNDYKDDD      147
1732-A6         LAAAEGHLEIVEVLLKHGADVNVQDKFGKTPFDLAINNGNEDIAEVLQKAAKLNDYKDDD      147
1731-C12        LAAANGHLEIVEVLLKHGADVNAQDKFDKTAFDISIDNGNEDIAEVLQKAAKLNDYKDDD      147
1731-H7         LAASEGHLEIVEVLLKHGADVNAQDKFGKTAFDISIDNGNEDIAEVLQKAAKLNDYKDDD      147
1731-F4         LAAAEGHLEIVEVLLKHGADVNAQDKFGKTAFDISIDNGNEDIAEVLQKAAKLNDYKDDD      147
1731-F12        LAAAEGHLEIVEVLLKAGADVNAQDKFGKTAFDISIDNGNEDIAEVLQKAAKLNDYKDDD      147
1732-H10        LAAAEGHLEIVEVLLKHGADVNAQDKFGKTAFDISIDNGNEDIAEVLQKAAKLNDYKDDD      147
                                        *  ..* **::   **********************

1732-A12        DK          149
1732-F8         DK          182
1729-E2         DK          149
1730-A7         DK          149
1731-H9         DK          116
1731-F9         DK          182
1731-D2         DK          182
1731-D12        DK          149
1730-C7         DK          149
1732-D1         DK          149
1731-F1         DK          149
1732-D9         DK          149
1732-B4         DK          149
1730-E12        DK          149
1731-G11        DK          149
1732-B2         DK          149
1731-G5         DK          149
1732-A6         DK          149
1731-C12        DK          149
1731-H7         DK          149
1731-F4         DK          149
1731-F12        DK          149
1732-H10        DK          149
                **
```

Figure 32: Sequence alignment of 23 selected DARPins performed on Clustal Omega 1.2.4 (multiple sequence alignment). All the sequences contain a FLAG-tag (DYKDDDDK).

6.2. Selection of high-affinity DARPins from purified bacterial extracts

After large scale production of the 23 selected binders and their purification, their affinities were re-measured using cell-based affinity assay at a known low concentration of 800 pM (Figure 33). A cut-off of 20% was applied and 6 binders were selected for further characterization (1731-F9, 1732-F8, 1730-E12, 1732-D1, 1730-C7 and 1731-H9, as its signal was close to 20% VCAM-1 positive cells).

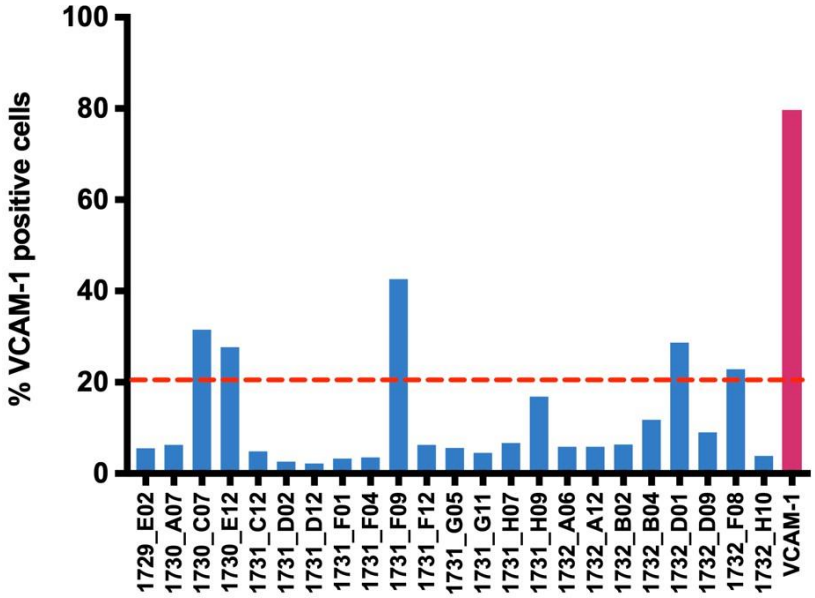

Figure 33: Affinity comparison of 23 binders to VCAM-1 in a cell-based assay. Purified DARPins were used at a concentration of 800 pM. A 20% cut off of positively labeled cells was applied.

All the DARPins were perfectly monomeric, except for the 1731-H9 DARPin, which showed aggregation tendency (heavy bands around 70 kD) and was therefore excluded from further analysis (Figure 34).

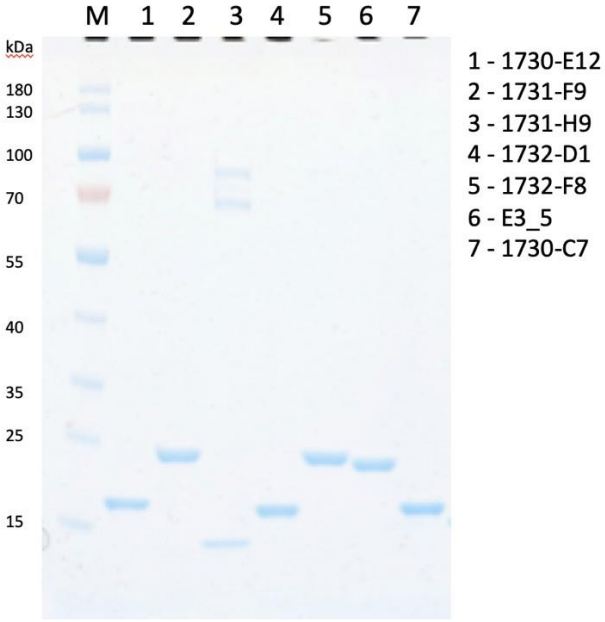

Figure 34: SDS page analysis of 6 DARPin binders and an isotype control DARPin (E3_5). 1731-H9 DARPin showed aggregation propensity (bands around 70 kD), all the other DARPins were perfectly monomeric and did not show any aggregation.

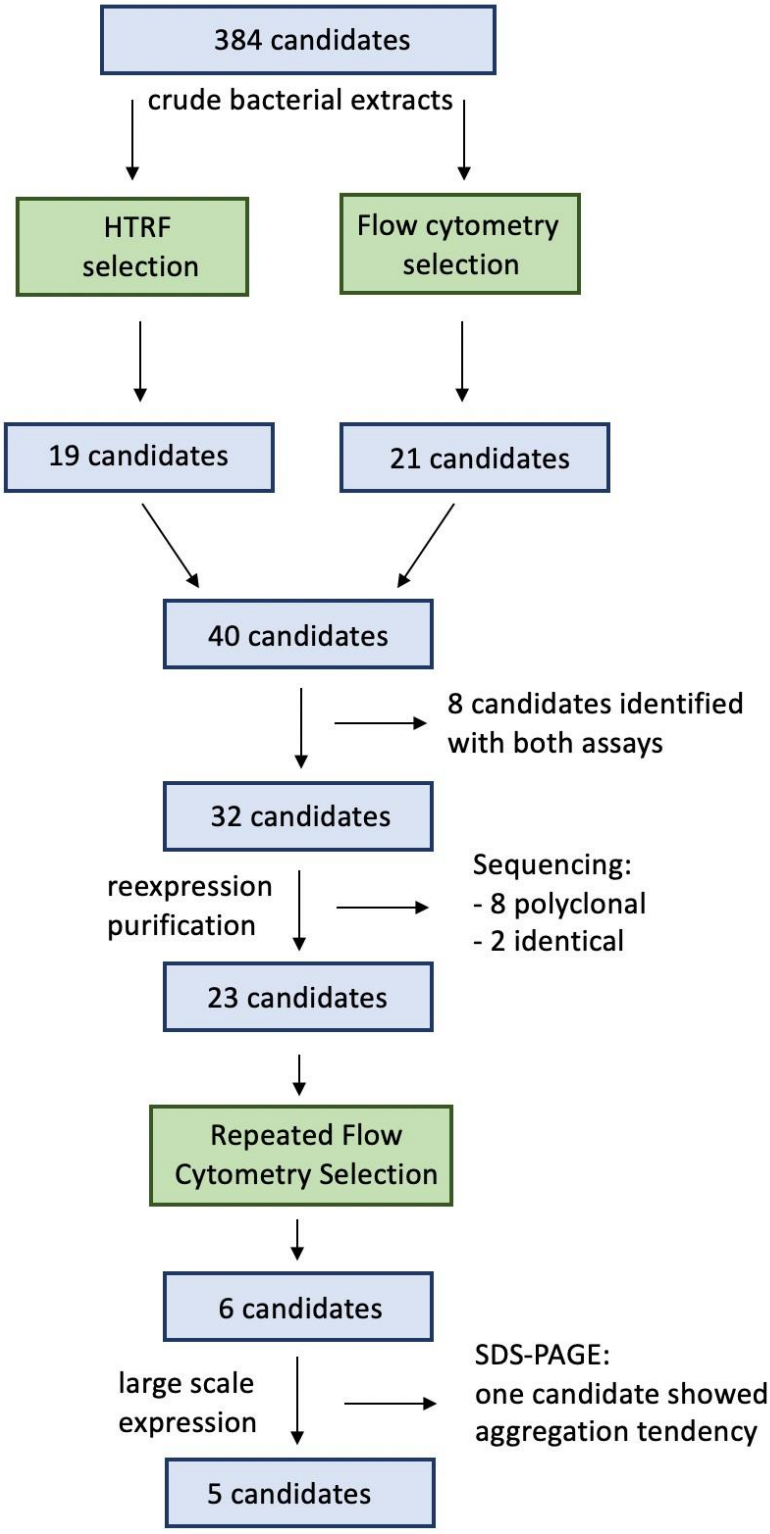

Figure 35: Summary of the selection strategy for high affinity DARPin binders.

6.3. Saturation Binding Affinity Assay of DARPin candidates

In the first characterization step, the affinities of the five selected DARPins were assessed in a cell-based saturation binding affinity assay by using a range of DARPin concentrations (Figure 36). Two paraments could be determined: equilibrium binding constant (K_d) and maximum specific binding (B_{max}), summarized in Table 3. K_d around 1 nM were obtained for all the DARPin binders, meaning that DARPin concentration of 1 nM is needed to achieve the half maximal binding at equilibrium. K_d was even lower for 1731-F9 and 1730-C7, indicating even better affinity. B_{max} was higher for 1731-F9 and 1732-F8, than for 1730-E12, 1732-D1 and 1730-C7. The isotype control DARPin as well as isotype control antibody did not bind to the target at any concentration, confirming that non-specific binding was very low under static conditions *in vitro*.

DARPin	1731-F9	1732-F8	1730-E12	1732-D1	1730-C7
K_d, nM	0.91	1.81	1.34	1.08	0.41
B_{max}, nM	82.79	80.57	62.06	61.53	52.27

Table 3: Affinity properties of five selected DARPin binders. K_d and B_{max} were determined using saturation binding fitting model in Prism 8.

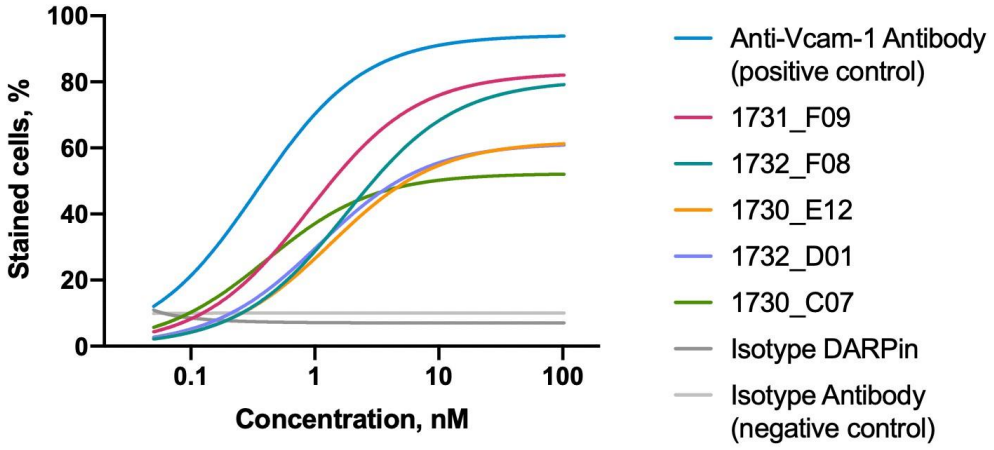

Figure 36: Saturation binding curves of individual DARPins and isotype control DARPin. Anti-VCAM-1 antibody and the corresponding isotype antibody were used as a positive and a negative control respectively.

6.4. Conjugation of DARPins to the microbubbles

6.4.1. Determining the optimal conjugation amount of DARPins to the microbubbles

Incubation of MBs with increasing concentrations of fluorescein labeled DARPins lead to an increase in MBs fluorescent intensity up to incubation of 1×10^8 MBs with 120 µg of DARPin, whereas a further increase in the amount of DARPins did not lead to a further increase in fluorescence intensity of the MBs (Figure 37). Thus, at an incubation of 1×10^8 MBs with 120 µg of DARPins all available maleimide binding sites were occupied, and the maximum of DARPin surface density on the MB shell was reached. As a consequence, for all further experiments, 1×10^8 MBs were incubated with 120 µg.

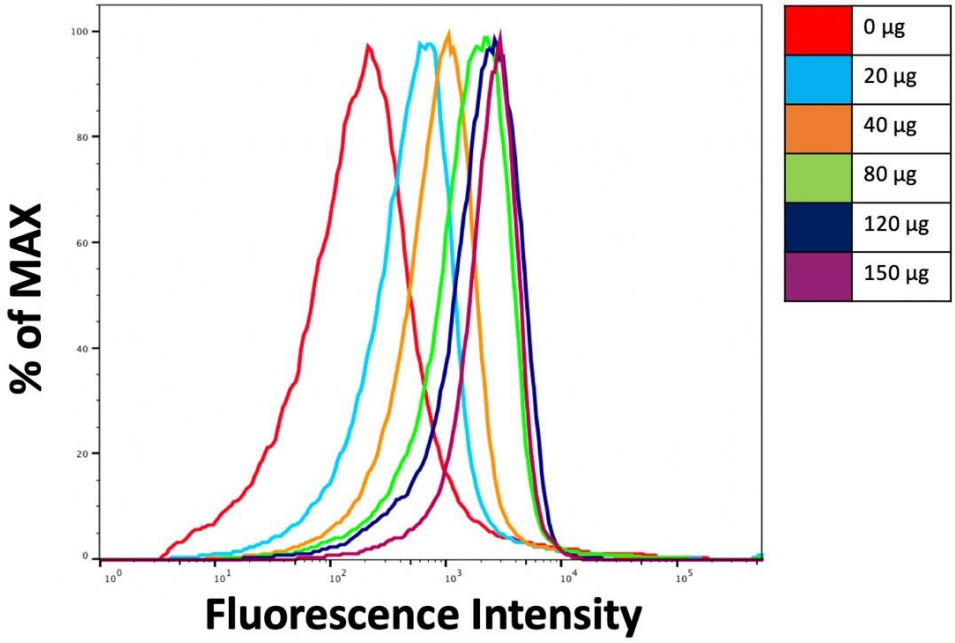

Figure 37: Determination of optimal conjugation concentration of DARPins by measuring the fluorescence intensity after incubating 1×10^8 MBs with increasing concentrations of fluorescently labeled 1730-E12 DARPin candidate.

6.4.2. Fluorescent Microscopy

In order to also visually validate the conjugation of DARPins to the maleimide on the microbubble surface via the C-terminal cysteine, fluorescence microscopy was used. As shown on Figure 38A, incubation with Alexa488-labeled 1731-F09 lead to bright fluorescence of the microbubble shell, and the fluorescent staining was uniformly distributed to all microbubbles within the visual field. In contrast, incubation with Alexa 488 only did not result in a fluorescence signal on the microbubble surface (Figure 38B), excluding a non-specific interaction of the Alexa 488 fluorophore itself with the microbubble shell. Also, as shown in Figure 38C, incubation with no-labeled 1731-F09 followed by incubation with Alexa488-labeled 1731-F09 resulted in minimal fluorescence signal on the

microbubble shell. Together, these data indicate that Alexa488-labeled 1731-F09 does bind to the microbubble shell surface via the maleimide moiety.

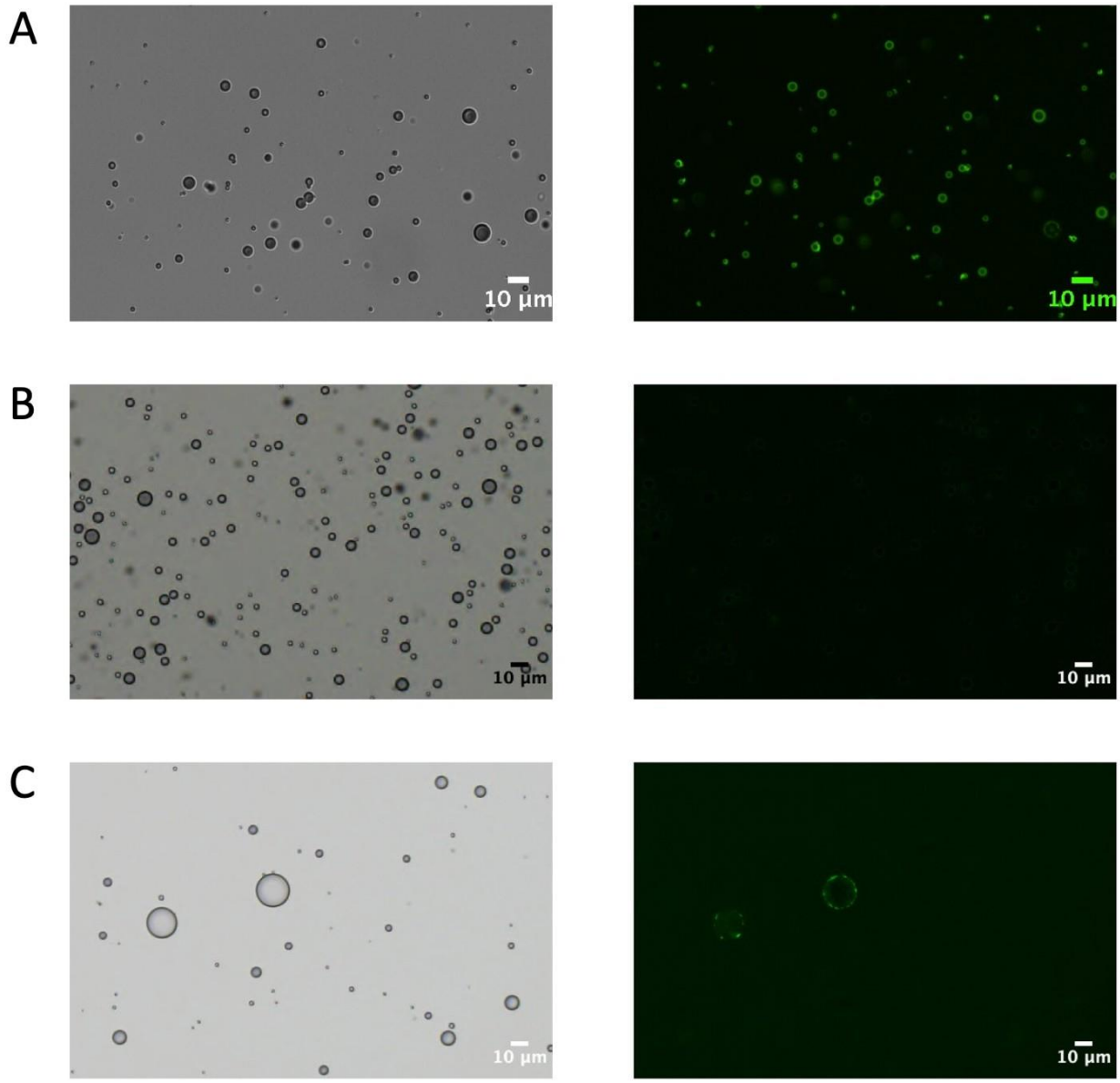

Figure 38: Bright field (left) and fluorescent (right) microscopy of MBs, carrying a (A) MB incubated with 120 µg of Alexa488-labeled DARPin 1731-F9, (B) MB incubated with 2 ml of Alexa488 and (C) MB incubated first with 400 µg of 1731-F9 and after washing steps with 60 µg of Alexa488-labeled DARPin 1731-F9. Scale bar of 10 µm is shown.

6.4.3. Determining the surface density of DARPins on the microbubble

Using 120 µg of DARPins as the optimal conjugation amount, the number of DARPins per microbubble was determined as $1.4x10^6 \pm 7.9x10^5$ and the number of DARPin molecules per μm^2 as $1.5x10^5 \pm 9.2x10^4$. Thus, one DARPin molecule occupies approximately 6.8 nm^2 (Figure 39) on the microbubble shell surface.

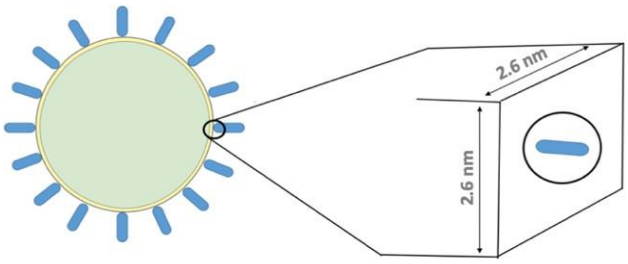

Figure 39: Surface density of DARPins on the surface of the microbubble. A surface area of DARPin molecule is shown.

6.5. Flow chamber studies with continuous flow

Flow chamber assays were used to characterize $MB_{DARPins}$ under continuous flow conditions and to select the binders with highest efficiency in binding VCAM-1 (Figure 40).

In a parallel flow chamber at a shear stress of 2 dynes/cm^2 significant retention of microbubbles carrying 1730-E12 DARPin candidate compared to $MB_{control}$ (18±3 vs. 6±1 MBs per optical field, p=0.0056) was observed on activated murine endothelial cells expressing VCAM-1. At a shear stress of 4 dynes/cm^2 1730-E12 (18±5 MBs per optical field vs. 1±0.2, p<0.0001) and 1732-D1 (6±1 vs.1±0.2, p=0.0058) DARPin candidates were significantly retained compared to $MB_{control}$. The remaining candidate binders showed a slightly increased retention, which was not significantly different from $MB_{control}$.

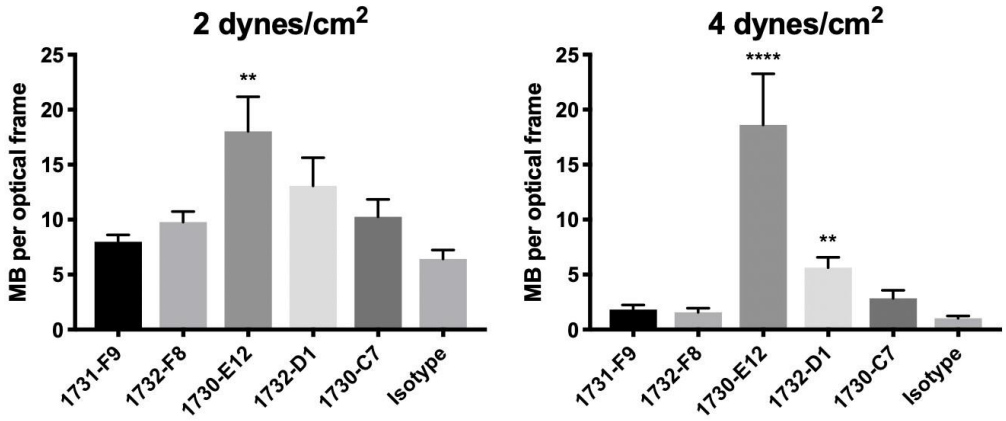

Figure 40: Significant retention of microbubbles carrying 1730-E12 and 1732-D1 DARPin candidates compared to $MB_{control}$ (n=6-9).

6.6. Hind limb inflammation mouse model

In this experiment following DARPin binders showed increased retention: 1732-F8 ($p = 0.0004$), 1730-C7 ($p = 0.0024$) and 1732-D1 ($p = 0.019$) (Figure 41).

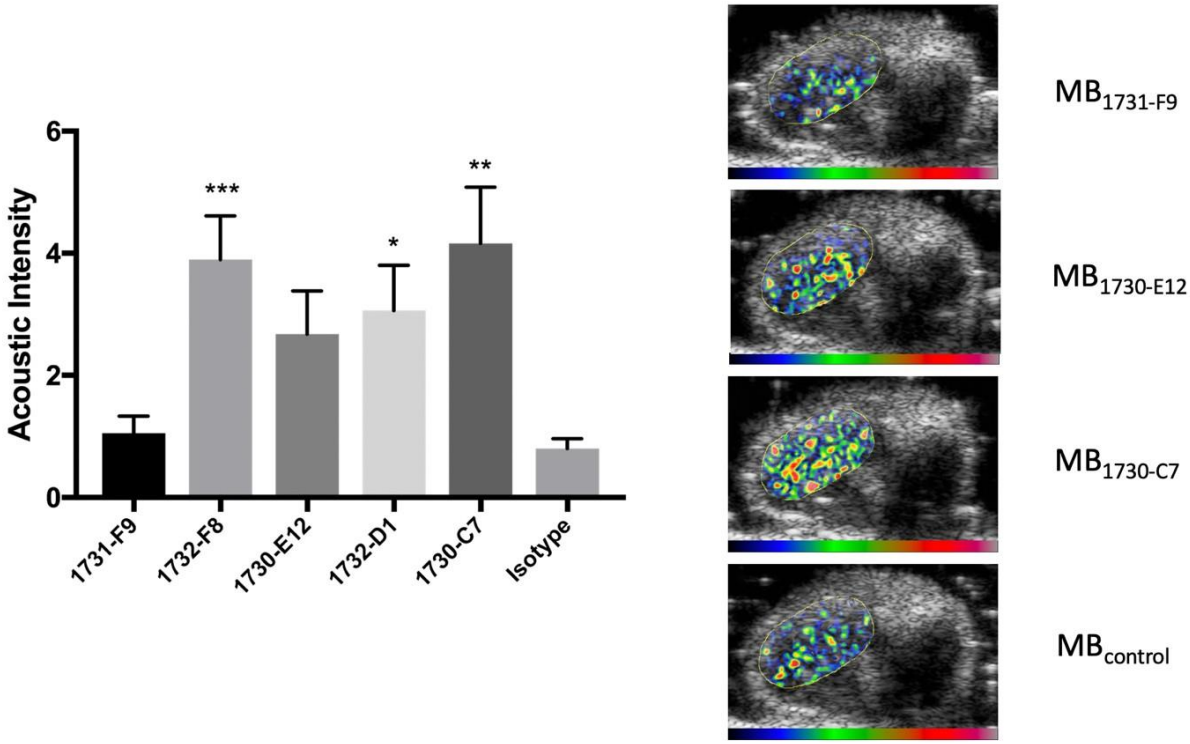

*Figure 41: CEUMI of inflamed hind limb showed significant signal enhancement above control for 1732-F8, 1732-D1 and 1730-C7 DARPin binders (*p<0.05, **p<0.005, ***p<0.0005, n=13). On the right panel representative background subtracted color coded images are shown.*

By comparing the results obtained from flow chamber assay and hind limb inflammation experiment, no correlation in ligand-induced microbubble attachment to VCAM-1 could be observed among the five candidate binders.

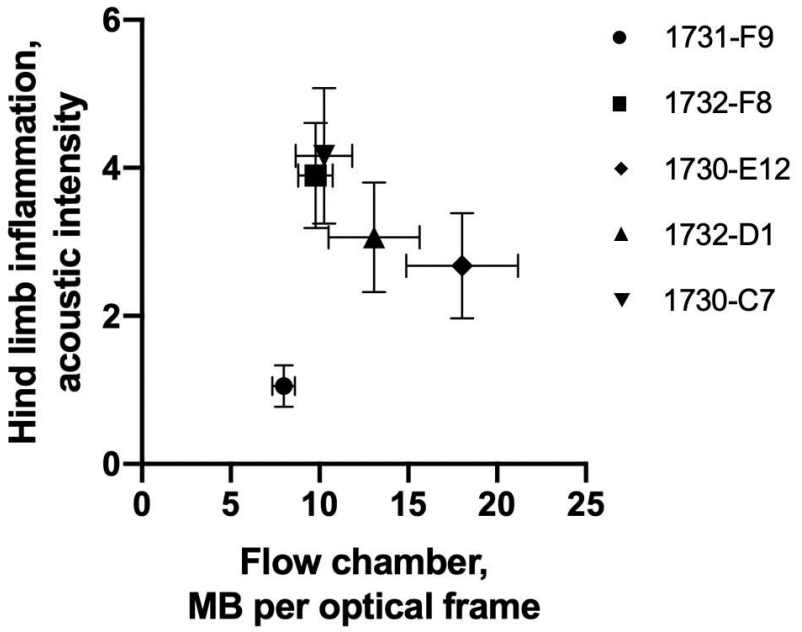

Figure 42: Correlation plot of signal intensities of $MB_{DARPins}$, comparing the results from the flow chamber assay with the results from hind limb inflammation model. No correlation could be found between the two assays.

Overall, these results clearly showed that $MB_{DARPins}$ targeted to VCAM-1 can be used *in vivo* to detect the presence of VCAM-1 on the surface of endothelial cells in a model of hind limb inflammation. For further validation, the two best DARPin candidates were chosen from the hind limb inflammation experiment: 1732-F8 and 1730-C7. An additional binder 1730-E12 with an intermediate target binding efficiency in the hind limb was also taken for further validation, as it showed significant results *in vitro* flow chamber studies. Thus, three DARPin candidates were chosen for further validation: 1732-F8, 1730-C7 and 1730-E12.

6.7. *In vivo* CEUMI of VCAM-1 expression in mouse aorta

The functionality of the selected DARPin binders was tested in a patho-physiologically relevant mouse model of early stage (Figure 43) and late stage (Figure 44) atherosclerosis. In this experimental setup $MB_{DARPins}$ were not significantly retained compared to $MB_{control}$, neither in the early, nor in the late stage of atherosclerotic progression. The amounts of the retention of $MB_{DARPins}$ and $MB_{control}$ are comparable to the negative control mice (wild type).

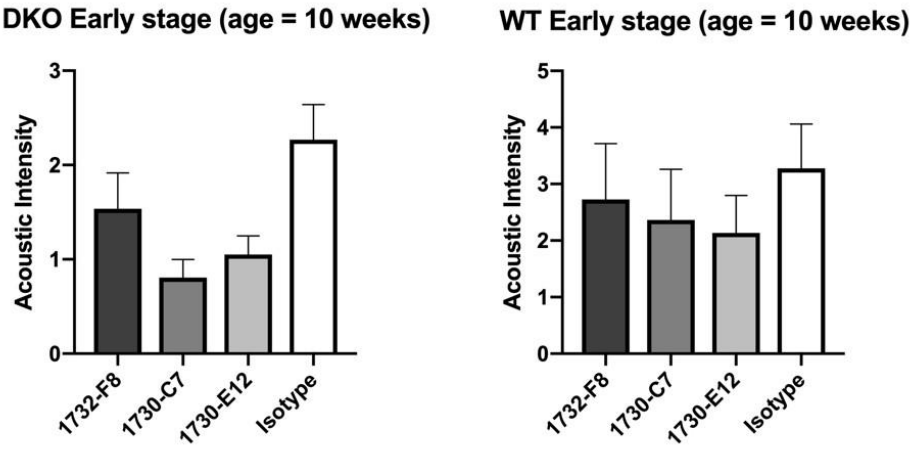

Figure 43: CEUMI of the aortic arch in double knockout (DKO, n=15) and wild type (WT, n=11) in the early stage of atherosclerotic pathogenesis (mice aged 10 weeks) after injection of $MB_{DARPins}$ and $MB_{control}$ targeting murine VCAM-1.

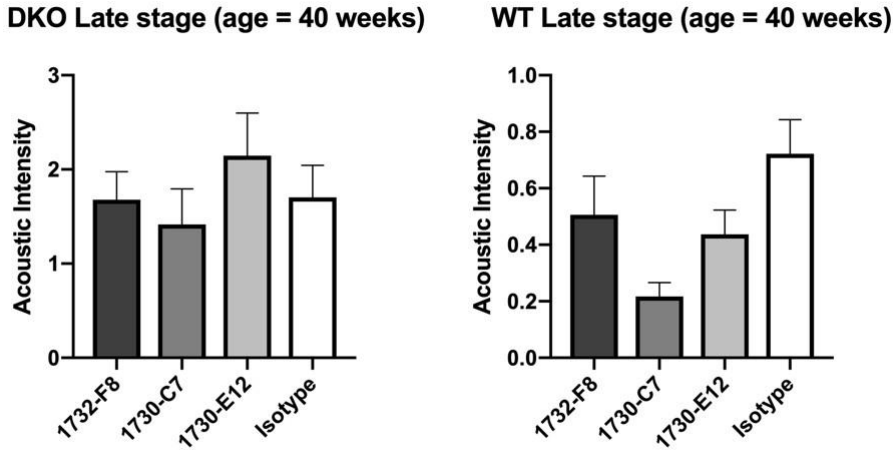

Figure 44: CEUMI of the aortic arch in double knockout (DKO, n=16) and wild type (WT, n= 16) in the late stage of atherosclerotic pathogenesis (mice aged 40 weeks) after injection of $MB_{DARPins}$ and $MB_{control}$ targeting murine VCAM-1.

6.8. Attachment and detachment characteristics of the selected DARPins

As no signal enhancement could be achieved in a high shear stress model of VCAM-1 expression, further flow chamber studies were conducted to better assess the binding kinetics properties of the selected DARPins.

6.8.1. Attachment characteristics

Attachment characteristics of the three selected DARPin binders were characterized *in vitro* in a flow chamber assay with a pulsatile flow (Figure 45). These experiments were carried out to determine whether short reductions in shear stress in the murine aorta during the diastole allow for microbubble

attachment. Sequential reductions in flow rate resulted in a significant increase in $MB_{DARPins}$ attachment for 1732-F8 and 1730-C7, but not for 1730-E12 DARPin binder, compared to the baseline. Although not significant, increased attachment of MB_{DARPin} 1730-E12 was observed compared to $MB_{control}$. Friedman's test with multiple comparisons was used for comparing the number of MBs at each flow reduction compared to the baseline.

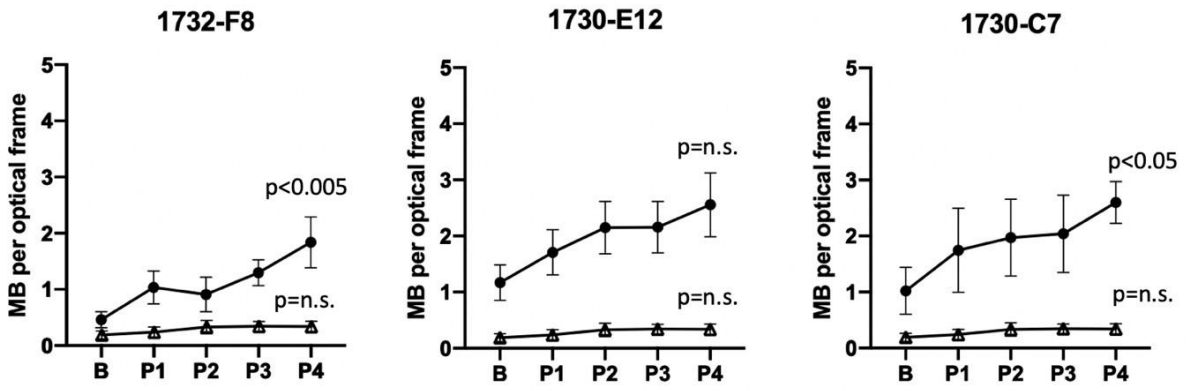

Figure 45: Pulsatile flow conditions: adhesion of $MB_{DARPins}$ (dots) compared to $MB_{control}$ after transient flow reductions (Baseline (B), P1, P2, P3, and P4) to <0.5 dyne/cm2, (n=5 each).

6.8.2. Detachment characteristics

Detachment characteristics of the three $MB_{DARPins}$ and $MB_{control}$ were studied in a flow chamber set up (Figure 46). These experiments were carried out to determine whether microbubbles attaching to VCAM-1 during brief reductions in shear stress are subsequently able to withstand the peak shear stresses in the murine aorta during systole. After initial attachment of the microbubbles at a low flow speed, $MB_{DARPins}$ as well as $MB_{control}$ showed low detachment rates. After the flow speed was increased, 1730-C7 and 1730-E12 showed quick detachment rate, comparable to the $MB_{control}$, with increased detachment at 20 dynes/cm^2 and a significant drop in the number of attached microbubbles at 25 dynes/cm^2. Although 1732-F8 candidate was showing variability in the detachment rates, it showed better retention compared to the other $MB_{DARPins}$. At the shear stress of 40 dynes/ cm^2 the median value of 1732-F8 was 21 MBs per optical field, which is 2 times more than for 1730-C7 (9.5 MBs per optical field), 14 times more than for 1730-E12 (1.5 MBs per optical field) and 10 times more than for the isotype control (2 MBs per optical field).

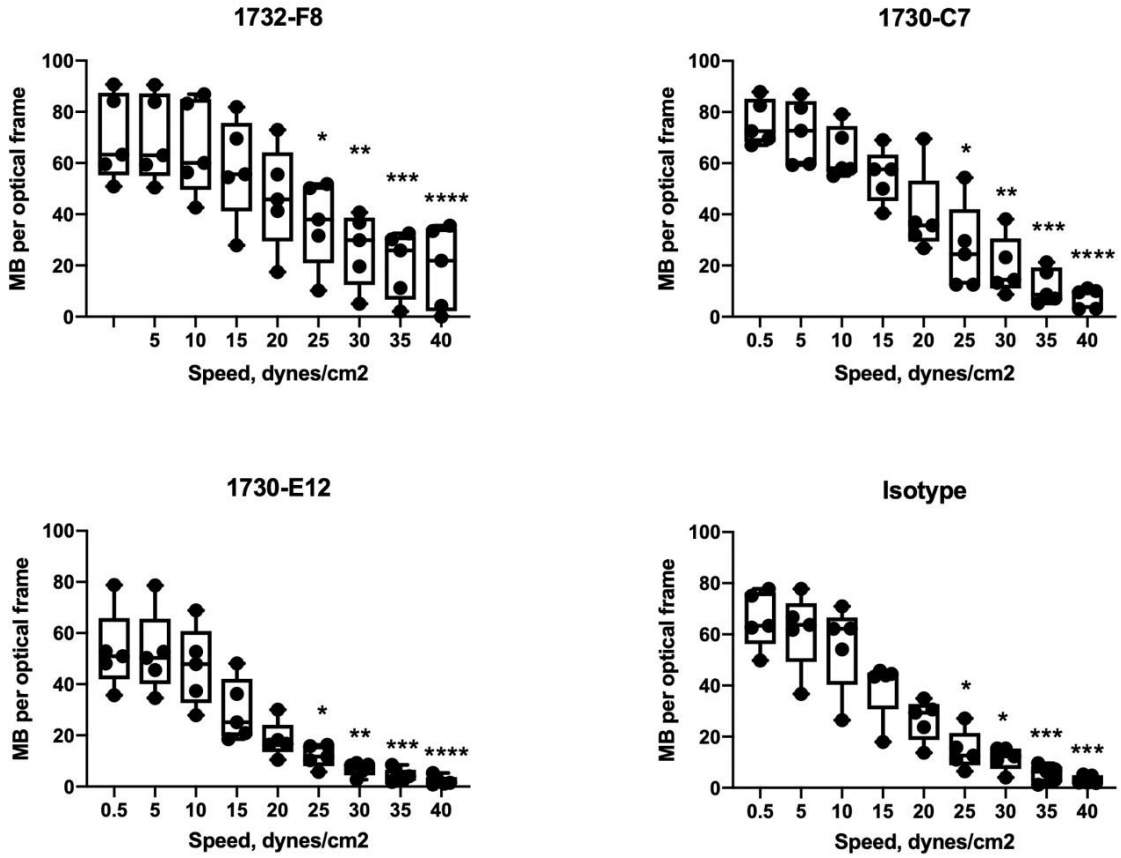

*Figure 46: Retention rates of $MB_{DARPins}$ and $MB_{control}$ under high shear stress conditions. The flow speed was sequentially increased from 0.5 dynes/cm^2 to 40 dynes/cm^2 in 5 dynes/cm^2 steps (*p<0.05, **p<0.01, ***p<0.001, ****p<0.0001, n=5 each). Median values (horizontal line) and range of values (whiskers) are presented. The boxes represent 25% and 75% percentiles.*

In Table 4 the results of all the assays with high affinity DARPin binders are compared semi-quantitatively:

Table 4: Comparison of the binding efficiency of DARPin binders in different in vitro and in vivo assays.

DARPin	1731-F9	1732-F8	1730-E12	1732-D1	1730-C7
Saturation Binding Assay	++	++	+	+	+
Flow Chamber, 2 dynes/cm^2	-	-	++	-	-
Flow Chamber, 4 dynes/cm^2	-	-	+	-	-
Hind Limb Inflammation model	-	++	+	+	++
Atherosclerotic model		-	-		-

7. Discussion

In this PhD thesis, we describe the selection, characterization and *in vitro* as well as *in vivo* evaluation of DARPins, a novel class of protein binders, for ultrasound molecular imaging. From a set of 384 DARPins, five candidates were selected using HTRF and flow cytometry. These five candidates performed similarly in a saturation binding assay under stationary conditions. However, after ligand attachment to microbubbles and under flow conditions in a flow chamber assay, large differences in ligand-induced microbubble adherence to VCAM-1 became evident among the five candidate binders. In an *in vivo* model of microvascular inflammation with endothelial expression of VCAM-1, three of the five DARPin ligands allowed for selective signal enhancement. However, there was no correlation between *in vitro* assays and the *in vivo* model in terms of the performance of the individual DARPins, indicating that flow chamber assays are not suitable for screening of candidate small protein ligands for ultrasound molecular imaging. Furthermore, in a high shear model of VCAM-1 expression in the murine aorta with early and advanced stages of atherosclerosis, selective signal enhancement was not achieved. Flow chamber assays investigating on-rates of DARPin carrying microbubbles during pulsatile flow and off-rates at increasing shear rates indicate that high off-rates may be responsible for the lack of selective signal enhancement in a high shear environment.

Comparison of the binding properties of DARPin binders in saturation binding assay and in flow chambers

Under stationary conditions in a cell-based saturation binding assay, the five selected DARPins behaved similarly and showed good affinities (K_d around 1nM) to the target on the surface of endothelial cells. However, in a flow chamber assay under dynamic conditions, attachment efficiencies differed between the DARPin binders, with 1730-E12 candidate showing higher attachment amounts compared to the remaining four candidates. In flow chamber assays DARPin binders were conjugated to the MBs and flow was introduced, and thus changes in the experimental conditions may well explain the different results compared to the stationary conditions. First, the introduction of flow and thus shear stress forces opposing the attachment of the DARPin ligand to VCAM-1 may have played a role. Second, in the flow chamber setup, the DARPins were conjugated to the MBs that are particles about the third of the size of red blood cells. Drag forces acting upon the MBs upon attachment to inflamed endothelium may have contributed to the detachment characteristics observed in our flow chamber experiments. DARPins are conjugated to the surface of the MBs using a PEG spacer arm (MW 3400 Da), to project the DARPin molecule away of the microbubble surface and thus expose it better to the target. One strategy to potentially increase targeting efficiency would be to alter the length the PEG

spacer arm (Khanicheh, et al. 2012). In fact, it has been already shown in a flow chamber set up, that the use of longer PEG spacers for ligand conjugation to the microparticles (MW 10000 Da compared to MW 3400 Da) leads to an increase in targeting efficiency under low shear stress conditions (Ham, et al. 2009). Moreover, in the same study it has been shown that targeting efficiency is improved due to the increasing bond lifetime of microparticles under shear stress conditions, as longer spacers allow the bond to preferentially localize on the trailing edge of the moving microparticle resulting in a reduction in torque acting on the adhesive site.

Sequence analysis

After several selection rounds, 32 DARPin binders were selected, purified and sequenced. After excluding polyclonal and identical candidates, sequencing analysis of the remaining 23 candidates revealed that 19 of them were members of N2C library, three binders (1731-D2, 1731-F9 and 1732-F8) were members of N3C library and one binder (1731-H9) a member of N1C library. In the final panel of five DARPin binders, two of them were members of N3C library (1731-F9 and 1732-F8) and three ones were members of N2C library (1730-E12, 1732-D1 and 1730-C7).

1731-F9 and 1730-C7 have a slightly better affinity (in pM range) than other DARPins according to the results from the cell-based saturation binding assay. The difference in the affinities (K_d) was not dependent on the number of internal repeats. Maximum specific binding, B_{max}, was shown to be higher for 1731-F9 and 1732-F8 DARPin binders. This could reflect differences in epitopes accessed by the individual DARPins, with given conditions being more favorable for 1731-F9 and 1732-F8. We can only speculate that stationary conditions were more favorable for the binders that exhibited three internal repeats (N3C library).

Comparison of the binding properties of MBs carrying DARPin binders to VCAM-1 in *in vitro* flow chamber assays versus the *in vivo* mouse hind limb inflammation model

While 1730-E12 showed selective adhesion to VCAM-1 *in vitro* on endothelial cells under flow conditions, three different DARPin candidates, 1732-F8, 1730-C7 and 1732-D1 showed increased retention *in vivo* in a hind limb inflammation model. Thus, we conclude that *in vitro* flow chamber studies were not predictive for the selection of high affinity binders for *in vivo* studies. An important parameter, which was technically impossible to avoid, is the difference in biochemical composition and viscosity between cell culture medium and mouse blood. These differences can potentially affect the epitope accessibility of VCAM-1 on the surface of endothelial cells *in vivo*, causing preferential

binding of 1732-F8, 1730-C7 DARPins and 1732-D1 over 1730-E12. Moreover, in a mouse model of hind limb inflammation, immune cells are recruited to VCAM-1 on endothelial cells shortly after induction of inflammation. The presence of these cells alters the accessibility to VCAM-1, which is not the case in a flow chamber set up. Another fact to be considered is a possible difference in the distribution of VCAM-1 on the surface of endothelial cells in a 2D cell culture in a flow chamber and in a 3D inflamed microvasculature. Potentially, the combination of the aforementioned factors influences binding of $MB_{DARPins}$ to VCAM-1 in two different set ups.

Still, our results indicate, that DARPin binders in a mouse of hind limb inflammation, it could be concluded that DARPin binders conjugated to the MBs through a maleimide coupling can be readily used for CEUMI of VCAM-1 expression in the microcirculation. VCAM-1 is expressed during inflammation processes in pathologic conditions, described earlier, but also in vascular remodeling processes during would healing, ischemia-mediated arteriogenesis and tumor neovascularization. In the study of Behm. et al. it has been demonstrated that the expression of VCAM-1 during ischemia-induced arteriogenesis can be successfully imaged in a mouse model of hind limb ischemia (Behm, et al. 2008). Pro-inflammatory VCAM-1 is expressed on the surface of endothelial cells during active vascular remodeling and acts as a homing receptor for circulation progenitor cells and may influence cell survival (Garmy-Susini, et al. 2005). Also, in a model of tumor neovascularization VCAM-1 was shown to act as a homing receptor for progenitor cells through $\alpha_4\beta_1$ ligands, whereas no homing took place in normal nonimmune tissues (Jin, et al. 2006). As angiogenesis is a hallmark of tumor growth, targeted CEUMI of VCAM-1 provides an opportunity to evaluate tumor growth or response to therapy.

Binding properties of DARPin binders in a mouse model of atherosclerosis

Based on the hind limb assay, high affinity DARPins were selected for validation in a patho-physiologically relevant model of atherosclerosis. For this purpose, two DARPins with the highest acoustic signal were selected: 1732-F8 and 1730-C7 as well as a DARPin with an intermediate acoustic signal intensity (1730-E12).

The DKO mouse model of atherosclerosis is characterized by a progressive development of atherosclerotic plaques. These DKO mice develop atherosclerosis in a predictable, time dependent fashion while on a normal chow diet (Farese, et al. 1996, Powell-Braxton, et al. 1998). In this experimental set up we were aiming to validate the binding of high affinity DARPins to VCAM-1 in an early (10 week of age) and a late (40 weeks of age) stage of atherosclerosis in mice. At both time points $MB_{DARPins}$ did not show selective signal enhancement for VCAM-1 and the signals were comparable to

the signal of $MB_{control}$. Given the fact that microbubble-DARPin conjugation (section 5.5.3), CEUMI imaging (Kaufmann, et al. 2007) and the mouse model (Khanicheh, et al. 2012) have been previously validated, the most likely reason for the lack of attachment are the binding kinetics properties of DARPin binders when exposed to the high shear stress environment. As mentioned before, the shear stress in a mouse aorta can reach a peak value of 80-90 dynes/cm^2 (Greve, et al. 2006) (compared to the shear stress in a hind limb inflammation model, which is not more than 3-5 dynes/cm^2 (Lindner, et al. 2001, Kaufmann, et al. 2007)). The high blood flow speed constitutes a great challenge for the binding properties of the targeting ligand, as the attachment is strongly dependent on a quick on-rate and slow off-rate. Given the pulsatile nature of the blood flow in the ascending aorta, low on-rate values could be tolerated when compensated by a very high affinity, as there is time for the targeting ligand to bind during diastole, as in the case of antibodies. On the contrary, a quick off-rate would cause a disability of the targeting ligand to stay attached to the target during the systole, even if the on-rate is quick enough.

Binding kinetics properties of DARPin binders

Having this in mind, we went back to the flow chamber set up in order to better characterize the binding kinetics properties of the three selected DARPin binders and the isotype control DARPin under high shear stress conditions. To estimate the on-rate, experiments with pulsatile flow were conducted. As it can be seen in Figure 45, for 1732-F8 and 1730-C7 DARPin binders, the number of attached microbubbles increased significantly with the number of flow reductions performed compared to the isotype control DARPin. For 1730-C7 MB_{DARPin} there was a steady increase in the number of attached microbubbles as compared to the $MB_{control}$. This increase did not achieve significance due to the high variability of the measurements. According to these data, we conclude that all $MB_{DARPins}$ have a sufficient on-rate in pulsatile flow conditions at a high shear stress of 8 dynes/cm^2. Pulsatile flow experiments with higher shear stress levels above 8 dynes/cm^2 were difficult to conduct due to technical limitations of the set up and high cost of consumables.

Also, the off-rate was estimated by studying detachment characteristics of $MB_{DARPins}$ in flow chambers by sequentially increasing the shear stress up to 40 dynes/cm^2. A significant decrease in the number of attached microbubbles was observed already at 25 dynes/cm^2 for all the $MB_{DARPins}$ as well as for the $MB_{control}$, at 40 dynes/cm^2 all the microbubbles were dislodged (Figure 46). Although 1732-F8 DARPin binder showed retention of the microbubbles even at 40 dynes/cm^2 for some measurements, its off-rate seems still to be too quick to resist the high shear stress in the aortic arch and the dissociation half-time is therefore as well very short.

As binding kinetics constants are a function of environmental parameters, like pH, temperature and, of course, speed of blood flow, *in vitro* flow chamber experiments represent the closest experimental set up to the mouse model, although on-and off-rates can still differ *in vivo*. As mentioned above, in the aortic arch, a low on-rate can be tolerated due the pulsatile nature of the flow. However, slow off-rate is crucial parameter for the efficient binding, which makes it a main determinant of the affinity in a given set up. Off-rate describes the highest transition state of the ligand leaving the binding pocket, which is related to the number of qualities of all atomic interaction within the binding pocket. Therefore, already during the selection process one should, if possible, aim to obtain binders with low off-rates.

Limitations of the study

Several limitations of the current study deserve mentioning. First, during ribosomal display, the DARPin binders were selected from a subset of a library. Selection of more potential candidate binders from larger libraries would have been possible, however, subsequent screening would have required a high-throughput setup not available in our laboratory. Second, in our set up we conjugated one DARPin type per to the MBs at a time. To increase the targeting efficiency one could use dual, or multiple targeting by conjugating different DARPins to the same microbubbles (Ferrante, et al. 2009). In order to do so, competition experiments would be needed in order assess the epitope recognition pattern of the selected binders. Last, the differences in biochemical composition between cell culture medium and mouse blood were could not be avoided.

Conclusion

In this PhD thesis, three DARPin binders (1732-F8, 1730-C7 and 1732-D1) were selected, which can be used for CEUMI of VCAM-1 expression in microcirculation. Using these contrast agents, vascular inflammation can be detected with non-invasive imaging in animal models. However, imaging in large arteries using these contrast agents, is limited, probably due to poor binding kinetics characteristics of the selected DARPin binders.

8. List of Abbreviations

ACS	Acute coronary syndrome
ADCC	Antibody-dependent cell-mediated cytotoxicity
AMD	Age-related macular degeneration
CA-125	Cancer Antigen 125
CCD	Charge-coupled device
CD3/CD4	Cluster of differentiation 3/4
CDC	Complement-dependent cytotoxicity
CEUMI	Contrast enhanced ultrasound molecular imaging
CPS	Contrast Pulse Sequence
CT	Computed tomography
CXCL1	C-X-X motif chemokine ligand 1
DARPin	Designed ankyrin repeat protein
dB	Decibel
DTT	Dithiothreitol
ECAM	endothelial cell adhesion molecule
ECG	electrocardiogram
ELIP	Echogenic liposome
EpCAM	endothelial cell adhesion molecule
FDA	Food and Drug Administration
FRET	fluorescence resonance energy transfer
HER2	Human epidermal growth factor receptor 2
HGF	Hepatocellular growth factor
HIV	Human immunodeficiency virus
HTRF	Homogeneous time resolved fluorescence
IBD	inflammatory bowel disease
ICAM-1	Intercellular adhesion molecule 1
Ig	Immunoglobulin
IL	Interleukin
IPTG	Isopropyl beta-D-1 thiogalactopyranoside
kHz, MHz	Kilohertz, Megahertz
k_{off}	Off-rate constant
k_{on}	On-rate constant

LDL	Low density lipoprotein
LV	Left ventricle
MAdCAM-1	Mucosal addressin cell adhesion molecule 1
MB	Microbubble
MI	Mechanical index
MPa	Megapascal
MRI	Magnetic resonance imaging
NB	Nanobubble
NF-κB	Nuclear factor kappa light chain enhancer of activated B cells
NHS	N-Hydroxysuccinimide
nm	nanometer
oxLDL	Oxidized low density lipoprotein
PCCA	Phase-change-contrast-agents
PCR	polymerase chain reaction
PECAM-1	Platelet/endothelial cell adhesion molecule 1
PEG	Polyethylene glycol
PET	Positron emission tomography
PGI_2	prostacyclin
PNP	Peak negative pressure
PPP	Peak positive pressure
PSGL-1	P-selectin glycoprotein ligand-1
RD	Ribosome Display
sLe^x	Sialyl Lewis X
SPECT	Single-photon emission computed tomography
TNF-α	Tumour-necrosis-factor alpha
UCA	Ultrasound contrast agents
VCAM-1	Vascular cell adhesion molecule 1
VEGF-A	Vascular endothelial growth factor A
vWF	Von Willebrand factor
W	Watt

9. References

Anderson DR, Tsutsui JM, Xie F, Radio SJ, Porter TR. The role of complement in the adherence of microbubbles to dysfunctional arterial endothelium and atherosclerotic plaque. Cardiovasc Res 2007;73:597-606.

Andrade MA, Perez-Iratxeta C, Ponting CP. Protein repeats: structures, functions, and evolution. J Struct Biol 2001;134:117-31.

Averkiou M, Powers J, Skyba D, Bruce M, Jensen S. Ultrasound contrast imaging research. Ultrasound Q 2003;19:27-37.

Bachmann C, Klibanov AL, Olson TS, Sonnenschein JR, Rivera-Nieves J, Cominelli F, Ley KF, Lindner JR, Pizarro TT. Targeting mucosal addressin cellular adhesion molecule (MAdCAM)-1 to noninvasively image experimental Crohn's disease. Gastroenterology 2006;130:8-16.

Barnes PJ, Karin M. Nuclear factor-kappaB: a pivotal transcription factor in chronic inflammatory diseases. N Engl J Med 1997;336:1066-71.

Bazzoni F, Rossato M, Fabbri M, Gaudiosi D, Mirolo M, Mori L, Tamassia N, Mantovani A, Cassatella MA, Locati M. Induction and regulatory function of miR-9 in human monocytes and neutrophils exposed to proinflammatory signals. Proc Natl Acad Sci U S A 2009;106:5282-7.

Beerli RR, Bauer M, Buser RB, Gwerder M, Muntwiler S, Maurer P, Saudan P, Bachmann MF. Isolation of human monoclonal antibodies by mammalian cell display. Proc Natl Acad Sci U S A 2008;105:14336-41.

Behm CZ, Kaufmann BA, Carr C, Lankford M, Sanders JM, Rose CE, Kaul S, Lindner JR. Molecular imaging of endothelial vascular cell adhesion molecule-1 expression and inflammatory cell recruitment during vasculogenesis and ischemia-mediated arteriogenesis. Circulation 2008;117:2902-11.

Bevilacqua MP. Endothelial-leukocyte adhesion molecules. Annu Rev Immunol 1993;11:767-804.

Binz HK, Amstutz P, Pluckthun A. Engineering novel binding proteins from nonimmunoglobulin domains. Nat Biotechnol 2005;23:1257-68.

Binz HK, Stumpp MT, Forrer P, Amstutz P, Pluckthun A. Designing repeat proteins: well-expressed, soluble and stable proteins from combinatorial libraries of consensus ankyrin repeat proteins. J Mol Biol 2003;332:489-503.

Boder ET, Wittrup KD. Yeast surface display for screening combinatorial polypeptide libraries. Nat Biotechnol 1997;15:553-7.

Borden MA, Streeter JE, Sirsi SR, Dayton PA. In vivo demonstration of cancer molecular imaging with ultrasound radiation force and buried-ligand microbubbles. Mol Imaging 2013;12:357-63.

Borregaard N, Kjeldsen L, Sengelov H, Diamond MS, Springer TA, Anderson HC, Kishimoto TK, Bainton DF. Changes in subcellular localization and surface expression of L-selectin, alkaline phosphatase, and Mac-1 in human neutrophils during stimulation with inflammatory mediators. J Leukoc Biol 1994;56:80-7.

Byrne GJ, Ghellal A, Iddon J, Blann AD, Venizelos V, Kumar S, Howell A, Bundred NJ. Serum soluble vascular cell adhesion molecule-1: role as a surrogate marker of angiogenesis. J Natl Cancer Inst 2000;92:1329-36.

Cai W, Schaper W. Mechanisms of arteriogenesis. Acta Biochim Biophys Sin (Shanghai) 2008;40:681-92.

Chadderdon SM, Belcik JT, Bader L, Kirigiti MA, Peters DM, Kievit P, Grove KL, Lindner JR. Proinflammatory endothelial activation detected by molecular imaging in obese nonhuman primates coincides with onset of insulin resistance and progressively increases with duration of insulin resistance. Circulation 2014;129:471-8.

Chan V, Perlas, A. Basics of Ultrasound Imaging, In: S. N, ed. *Atlas of Ultrasound-Guided Procedures in Interventional Pain Management*. New York, NY: Springer, 2011. 13-19.

Conrad SA. Focused Echocardiography in the ICU. *Bedside Procedures for the Intensivist,*: Springer Science+Business Media,, 2010.

Cook-Mills JM, Marchese ME, Abdala-Valencia H. Vascular cell adhesion molecule-1 expression and signaling during disease: regulation by reactive oxygen species and antioxidants. Antioxid Redox Signal 2011;15:1607-38.

Cormode DP, Roessl E, Thran A, Skajaa T, Gordon RE, Schlomka JP, Fuster V, Fisher EA, Mulder WJ, Proksa R, Fayad ZA. Atherosclerotic plaque composition: analysis with multicolor CT and targeted gold nanoparticles. Radiology 2010;256:774-82.

Davidson BP, Chadderdon SM, Belcik JT, Gupta S, Lindner JR. Ischemic memory imaging in nonhuman primates with echocardiographic molecular imaging of selectin expression. J Am Soc Echocardiogr 2014;27:786-93 e2.

Dayton PA, Morgan KE, Klibanov AL, Brandenburger GH, Ferrara KW. Optical and acoustical observations of the effects of ultrasound on contrast agents. IEEE Trans Ultrason Ferroelectr Freq Control 1999;46:220-32.

de Jong N, Hoff, L., Skotland, T., Bom, N. Absorption and scatter of encapsulated gas filled microspheres: Theoretical considerations and some measurements. *Ultrasonics*: Elsevier B.V., 1992. 95-103.

Deshpande N, Needles A, Willmann JK. Molecular ultrasound imaging: current status and future directions. Clin Radiol 2010;65:567-81.

Ding YB, Chen GY, Xia JG, Zang XW, Yang HY, Yang L. Association of VCAM-1 overexpression with oncogenesis, tumor angiogenesis and metastasis of gastric carcinoma. World J Gastroenterol 2003;9:1409-14.

Dreier B, Pluckthun A. Ribosome display: a technology for selecting and evolving proteins from large libraries. Methods Mol Biol 2011;687:283-306.

Farese RV, Jr., Veniant MM, Cham CM, Flynn LM, Pierotti V, Loring JF, Traber M, Ruland S, Stokowski RS, Huszar D, Young SG. Phenotypic analysis of mice expressing exclusively apolipoprotein B48 or apolipoprotein B100. Proc Natl Acad Sci U S A 1996;93:6393-8.

Ferrante EA, Pickard JE, Rychak J, Klibanov A, Ley K. Dual targeting improves microbubble contrast agent adhesion to VCAM-1 and P-selectin under flow. J Control Release 2009;140:100-7.

Fisher NG, Christiansen JP, Klibanov A, Taylor RP, Kaul S, Lindner JR. Influence of microbubble surface charge on capillary transit and myocardial contrast enhancement. J Am Coll Cardiol 2002;40:811-9.

Folkman J. Diagnostic and therapeutic applications of angiogenesis research. C R Acad Sci III 1993;316:909-18.

Forrer P, Binz HK, Stumpp MT, Pluckthun A. Consensus design of repeat proteins. Chembiochem 2004;5:183-9.

Francisco JA, Earhart CF, Georgiou G. Transport and anchoring of beta-lactamase to the external surface of Escherichia coli. Proc Natl Acad Sci U S A 1992;89:2713-7.

Fries JW, Williams AJ, Atkins RC, Newman W, Lipscomb MF, Collins T. Expression of VCAM-1 and E-selectin in an in vivo model of endothelial activation. Am J Pathol 1993;143:725-37.

Garmy-Susini B, Jin H, Zhu Y, Sung RJ, Hwang R, Varner J. Integrin alpha4beta1-VCAM-1-mediated adhesion between endothelial and mural cells is required for blood vessel maturation. J Clin Invest 2005;115:1542-51.

Glockshuber R, Malia M, Pfitzinger I, Pluckthun A. A comparison of strategies to stabilize immunoglobulin Fv-fragments. Biochemistry 1990;29:1362-7.

Gramiak R, Shah PM. Echocardiography of the aortic root. Invest Radiol 1968;3:356-66.

Greve JM, Les AS, Tang BT, Draney Blomme MT, Wilson NM, Dalman RL, Pelc NJ, Taylor CA. Allometric scaling of wall shear stress from mice to humans: quantification using cine phase-contrast MRI and computational fluid dynamics. Am J Physiol Heart Circ Physiol 2006;291:H1700-8.

Ham AS, Klibanov AL, Lawrence MB. Action at a distance: lengthening adhesion bonds with poly(ethylene glycol) spacers enhances mechanically stressed affinity for improved vascular targeting of microparticles. Langmuir 2009;25:10038-44.

Hanenberg M, McAfoose J, Kulic L, Welt T, Wirth F, Parizek P, Strobel L, Cattepoel S, Spani C, Derungs R, Maier M, Pluckthun A, Nitsch RM. Amyloid-beta peptide-specific DARPins as a novel class of potential therapeutics for Alzheimer disease. J Biol Chem 2014;289:27080-9.

Hanes J, Pluckthun A. In vitro selection and evolution of functional proteins by using ribosome display. Proc Natl Acad Sci U S A 1997;94:4937-42.

Herlyn DM, Koprowski H. Monoclonal anticolon carcinoma antibodies in complement-dependent cytotoxicity. Int J Cancer 1981;27:769-74.

Hernot S, Unnikrishnan S, Du Z, Shevchenko T, Cosyns B, Broisat A, Toczek J, Caveliers V, Muyldermans S, Lahoutte T, Klibanov AL, Devoogdt N. Nanobody-coupled microbubbles as novel molecular tracer. J Control Release 2012;158:346-53.

Hobbs SK, Monsky WL, Yuan F, Roberts WG, Griffith L, Torchilin VP, Jain RK. Regulation of transport pathways in tumor vessels: role of tumor type and microenvironment. Proc Natl Acad Sci U S A 1998;95:4607-12.

Hoeben A, Landuyt B, Highley MS, Wildiers H, Van Oosterom AT, De Bruijn EA. Vascular endothelial growth factor and angiogenesis. Pharmacol Rev 2004;56:549-80.

Hosse RJ, Rothe A, Power BE. A new generation of protein display scaffolds for molecular recognition. Protein Sci 2006;15:14-27.

Huang SL. Liposomes in ultrasonic drug and gene delivery. Adv Drug Deliv Rev 2008;60:1167-76.

Issa B, Obaidat IM, Albiss BA, Haik Y. Magnetic nanoparticles: surface effects and properties related to biomedicine applications. Int J Mol Sci 2013;14:21266-305.

Jackson SP, Darbousset R, Schoenwaelder SM. Thromboinflammation: challenges of therapeutically targeting coagulation and other host defense mechanisms. Blood 2019;133:906-18.

Jayaweera AR, Edwards N, Glasheen WP, Villanueva FS, Abbott RD, Kaul S. In vivo myocardial kinetics of air-filled albumin microbubbles during myocardial contrast echocardiography. Comparison with radiolabeled red blood cells. Circ Res 1994;74:1157-65.

Jin H, Aiyer A, Su J, Borgstrom P, Stupack D, Friedlander M, Varner J. A homing mechanism for bone marrow-derived progenitor cell recruitment to the neovasculature. J Clin Invest 2006;116:652-62.

Kaltenbach M, Hollfelder F. SNAP display: in vitro protein evolution in microdroplets. Methods Mol Biol 2012;805:101-11.

Karimova G, Pidoux J, Ullmann A, Ladant D. A bacterial two-hybrid system based on a reconstituted signal transduction pathway. Proc Natl Acad Sci U S A 1998;95:5752-6.

Kaufmann BA, Lewis C, Xie A, Mirza-Mohd A, Lindner JR. Detection of recent myocardial ischaemia by molecular imaging of P-selectin with targeted contrast echocardiography. Eur Heart J 2007;28:2011-7.

Kaufmann BA, Sanders JM, Davis C, Xie A, Aldred P, Sarembock IJ, Lindner JR. Molecular imaging of inflammation in atherosclerosis with targeted ultrasound detection of vascular cell adhesion molecule-1. Circulation 2007;116:276-84.

Kaufmann BA, Wei K, Lindner JR. Contrast echocardiography. Curr Probl Cardiol 2007;32:51-96.

Kee PH, Kim H, Huang S, Laing ST, Moody MR, Vela D, Klegerman ME, McPherson DD. Nitric oxide pretreatment enhances atheroma component highlighting in vivo with intercellular adhesion molecule-1-targeted echogenic liposomes. Ultrasound Med Biol 2014;40:1167-76.

Khanicheh E, Mitterhuber M, Kinslechner K, Xu L, Lindner JR, Kaufmann BA. Factors affecting the endothelial retention of targeted microbubbles: influence of microbubble shell design and cell surface projection of the endothelial target molecule. J Am Soc Echocardiogr 2012;25:460-6.

Khanicheh E, Mitterhuber M, Xu L, Haeuselmann SP, Kuster GM, Kaufmann BA. Noninvasive ultrasound molecular imaging of the effect of statins on endothelial inflammatory phenotype in early atherosclerosis. PLoS One 2013;8:e58761.

Khanicheh E, Qi Y, Xie A, Mitterhuber M, Xu L, Mochizuki M, Daali Y, Jaquet V, Krause KH, Ruggeri ZM, Kuster GM, Lindner JR, Kaufmann BA. Molecular imaging reveals rapid reduction of endothelial activation in early atherosclerosis with apocynin independent of antioxidative properties. Arterioscler Thromb Vasc Biol 2013;33:2187-92.

Kirpotin D, Park JW, Hong K, Zalipsky S, Li WL, Carter P, Benz CC, Papahadjopoulos D. Sterically stabilized anti-HER2 immunoliposomes: design and targeting to human breast cancer cells in vitro. Biochemistry 1997;36:66-75.

Klibanov AL. Ligand-carrying gas-filled microbubbles: ultrasound contrast agents for targeted molecular imaging. Bioconjug Chem 2005;16:9-17.

Klibanov AL, Maruyama K, Torchilin VP, Huang L. Amphipathic polyethyleneglycols effectively prolong the circulation time of liposomes. FEBS Lett 1990;268:235-7.

Kobe B, Deisenhofer J. The leucine-rich repeat: a versatile binding motif. Trends Biochem Sci 1994;19:415-21.

Kobe B, Kajava AV. When protein folding is simplified to protein coiling: the continuum of solenoid protein structures. Trends Biochem Sci 2000;25:509-15.

Kong DH, Kim YK, Kim MR, Jang JH, Lee S. Emerging Roles of Vascular Cell Adhesion Molecule-1 (VCAM-1) in Immunological Disorders and Cancer. Int J Mol Sci 2018;19.

Kunsch C, Medford RM. Oxidative stress as a regulator of gene expression in the vasculature. Circ Res 1999;85:753-66.

Landmark KE, Johansen PW, Johnson JA, Johansen B, Uran S, Skotland T. Pharmacokinetics of perfluorobutane following intravenous bolus injection and continuous infusion of sonazoid in healthy volunteers and in patients with reduced pulmonary diffusing capacity. Ultrasound Med Biol 2008;34:494-501.

Leung DW, Cachianes G, Kuang WJ, Goeddel DV, Ferrara N. Vascular endothelial growth factor is a secreted angiogenic mitogen. Science 1989;246:1306-9.

Ley K. Molecular mechanisms of leukocyte recruitment in the inflammatory process. Cardiovasc Res 1996;32:733-42.

Ley K. The role of selectins in inflammation and disease. Trends Mol Med 2003;9:263-8.

Lindner JR, Coggins MP, Kaul S, Klibanov AL, Brandenburger GH, Ley K. Microbubble persistence in the microcirculation during ischemia/reperfusion and inflammation is caused by integrin- and complement-mediated adherence to activated leukocytes. Circulation 2000;101:668-75.

Lindner JR, Dayton PA, Coggins MP, Ley K, Song J, Ferrara K, Kaul S. Noninvasive imaging of inflammation by ultrasound detection of phagocytosed microbubbles. Circulation 2000;102:531-8.

Lindner JR, Firschke C, Wei K, Goodman NC, Skyba DM, Kaul S. Myocardial perfusion characteristics and hemodynamic profile of MRX-115, a venous echocardiographic contrast agent, during acute myocardial infarction. J Am Soc Echocardiogr 1998;11:36-46.

Lindner JR, Song J, Christiansen J, Klibanov AL, Xu F, Ley K. Ultrasound assessment of inflammation and renal tissue injury with microbubbles targeted to P-selectin. Circulation 2001;104:2107-12.

Lindner JR, Song J, Jayaweera AR, Sklenar J, Kaul S. Microvascular rheology of Definity microbubbles after intra-arterial and intravenous administration. J Am Soc Echocardiogr 2002;15:396-403.

Liu X, Gong P, Song P, Xie F, Miller Ii AL, Chen S, Lu L. Fast functionalization of ultrasound microbubbles using strain promoted click chemistry. Biomater Sci 2018;6:623-32.

Lusis AJ. Atherosclerosis. Nature 2000;407:233-41.

Malm S, Frigstad S, Sagberg E, Larsson H, Skjaerpe T. Accurate and reproducible measurement of left ventricular volume and ejection fraction by contrast echocardiography: a comparison with magnetic resonance imaging. J Am Coll Cardiol 2004;44:1030-5.

Mann A, Friedrich N, Krarup A, Weber J, Stiegeler E, Dreier B, Pugach P, Robbiani M, Riedel T, Moehle K, Robinson JA, Rusert P, Pluckthun A, Trkola A. Conformation-dependent

recognition of HIV gp120 by designed ankyrin repeat proteins provides access to novel HIV entry inhibitors. J Virol 2013;87:5868-81.

Moccetti F, Weinkauf CC, Davidson BP, Belcik JT, Marinelli ER, Unger E, Lindner JR. Ultrasound Molecular Imaging of Atherosclerosis Using Small-Peptide Targeting Ligands Against Endothelial Markers of Inflammation and Oxidative Stress. Ultrasound Med Biol 2018;44:1155-63.

Moisseiev E, Loewenstein A. Abicipar pegol-a novel anti-VEGF therapy with a long duration of action. Eye (Lond) 2019.

Moller E. Cytotoxicity by nonimmune allogeneic lymphoid cells. Specific suppression by antibody treatment of the lymphoid cells. J Exp Med 1967;126:395-405.

Mott B, Packwood W, Xie A, Belcik JT, Taylor RP, Zhao Y, Davidson BP, Lindner JR. Echocardiographic Ischemic Memory Imaging Through Complement-Mediated Vascular Adhesion of Phosphatidylserine-Containing Microbubbles. JACC Cardiovasc Imaging 2016;9:937-46.

Muller WA. Mechanisms of leukocyte transendothelial migration. Annu Rev Pathol 2011;6:323-44.

Nadia R. Sutton AB, David J. Pinsky. Endothelial Cells and Inflammation: Springer, New York, NY, 2014.

Nelson AL, Reichert JM. Development trends for therapeutic antibody fragments. Nat Biotechnol 2009;27:331-7.

Olson TS, Ley K. Chemokines and chemokine receptors in leukocyte trafficking. Am J Physiol Regul Integr Comp Physiol 2002;283:R7-28.

Paul S, Nahire R, Mallik S, Sarkar K. Encapsulated microbubbles and echogenic liposomes for contrast ultrasound imaging and targeted drug delivery. Comput Mech 2014;53:413-35.

Potente M, Gerhardt H, Carmeliet P. Basic and therapeutic aspects of angiogenesis. Cell 2011;146:873-87.

Powell-Braxton L, Veniant M, Latvala RD, Hirano KI, Won WB, Ross J, Dybdal N, Zlot CH, Young SG, Davidson NO. A mouse model of human familial hypercholesterolemia: markedly elevated low density lipoprotein cholesterol levels and severe atherosclerosis on a low-fat chow diet. Nat Med 1998;4:934-8.

Punjabi M, Xu L, Ochoa-Espinosa A, Kosareva A, Wolff T, Murtaja A, Broisat A, Devoogdt N, Kaufmann BA. Ultrasound Molecular Imaging of Atherosclerosis With Nanobodies: Translatable Microbubble Targeting Murine and Human VCAM (Vascular Cell Adhesion Molecule) 1. Arterioscler Thromb Vasc Biol 2019;39:2520-30.

Pysz MA, Gambhir SS, Willmann JK. Molecular imaging: current status and emerging strategies. Clin Radiol 2010;65:500-16.

Rapoport N, Gao Z, Kennedy A. Multifunctional nanoparticles for combining ultrasonic tumor imaging and targeted chemotherapy. J Natl Cancer Inst 2007;99:1095-106.

Rice GE, Bevilacqua MP. An inducible endothelial cell surface glycoprotein mediates melanoma adhesion. Science 1989;246:1303-6.

Roberts RW, Szostak JW. RNA-peptide fusions for the in vitro selection of peptides and proteins. Proc Natl Acad Sci U S A 1997;94:12297-302.

Rojas JD, Dayton PA. In Vivo Molecular Imaging Using Low-Boiling-Point Phase-Change Contrast Agents: A Proof of Concept Study. Ultrasound Med Biol 2019;45:177-91.

Rosenberg AaD, B. Biobetters: Protein engineering to approach the curative,: Springer, 2015.

Ruehm SG, Corot C, Vogt P, Kolb S, Debatin JF. Magnetic resonance imaging of atherosclerotic plaque with ultrasmall superparamagnetic particles of iron oxide in hyperlipidemic rabbits. Circulation 2001;103:415-22.

Ryu JC, Davidson BP, Xie A, Qi Y, Zha D, Belcik JT, Caplan ES, Woda JM, Hedrick CC, Hanna RN, Lehman N, Zhao Y, Ting A, Lindner JR. Molecular imaging of the paracrine proangiogenic effects of progenitor cell therapy in limb ischemia. Circulation 2013;127:710-9.

Sedgwick SG, Smerdon SJ. The ankyrin repeat: a diversity of interactions on a common structural framework. Trends Biochem Sci 1999;24:311-6.

Sen T, Tufekcioglu O, Koza Y. Mechanical index. Anatol J Cardiol 2015;15:334-6.

Senior R, Khattar RS. Cardiac investigation for prognosis in coronary artery disease: where negative is positive. Eur Heart J Cardiovasc Imaging 2017;18:988-89.

Sheeran PS, Luois S, Dayton PA, Matsunaga TO. Formulation and acoustic studies of a new phase-shift agent for diagnostic and therapeutic ultrasound. Langmuir 2011;27:10412-20.

Skerra A. Alternative non-antibody scaffolds for molecular recognition. Curr Opin Biotechnol 2007;18:295-304.

Skerra A, Pluckthun A. Assembly of a functional immunoglobulin Fv fragment in Escherichia coli. Science 1988;240:1038-41.

Smith GP. Filamentous fusion phage: novel expression vectors that display cloned antigens on the virion surface. Science 1985;228:1315-7.

Solomon A, Gramse M, Havemann K. Proteolytic cleavage of human IgG molecules by neutral proteases of polymorphonuclear leukocytes. Eur J Immunol 1978;8:782-5.

Springer TA. Adhesion receptors of the immune system. Nature 1990;346:425-34.

Stahl A, Stumpp MT, Schlegel A, Ekawardhani S, Lehrling C, Martin G, Gulotti-Georgieva M, Villemagne D, Forrer P, Agostini HT, Binz HK. Highly potent VEGF-A-antagonistic DARPins as anti-angiogenic agents for topical and intravitreal applications. Angiogenesis 2013;16:101-11.

Stefan N, Martin-Killias P, Wyss-Stoeckle S, Honegger A, Zangemeister-Wittke U, Pluckthun A. DARPins recognizing the tumor-associated antigen EpCAM selected by phage and ribosome display and engineered for multivalency. J Mol Biol 2011;413:826-43.

Steinl DC, Kaufmann BA. Ultrasound imaging for risk assessment in atherosclerosis. Int J Mol Sci 2015;16:9749-69.

Steinl DC, Xu L, Khanicheh E, Ellertsdottir E, Ochoa-Espinosa A, Mitterhuber M, Glatz K, Kuster GM, Kaufmann BA. Noninvasive Contrast-Enhanced Ultrasound Molecular Imaging Detects Myocardial Inflammatory Response in Autoimmune Myocarditis. Circulation. Cardiovascular imaging 2016;9.

Stocker R, Keaney JF, Jr. Role of oxidative modifications in atherosclerosis. Physiol Rev 2004;84:1381-478.

Streeter JE, Dayton PA. An in vivo evaluation of the effect of repeated administration and clearance of targeted contrast agents on molecular imaging signal enhancement. Theranostics 2013;3:93-8.

Talu E, Hettiarachchi K, Zhao S, Powell RL, Lee AP, Longo ML, Dayton PA. Tailoring the size distribution of ultrasound contrast agents: possible method for improving sensitivity in molecular imaging. Mol Imaging 2007;6:384-92.

Tamaskovic R, Simon M, Stefan N, Schwill M, Pluckthun A. Designed ankyrin repeat proteins (DARPins) from research to therapy. Methods Enzymol 2012;503:101-34.

Verma G. Advances in Diagnostic Techniques for Therapeutic Intervention, In: S. P, ed. *Biomedical Engineering and its Applications in Healthcare*. Singapore: Springer, 2019. 105-21.

Villanueva FS, Wagner WR. Ultrasound molecular imaging of cardiovascular disease. Nat Clin Pract Cardiovasc Med 2008;5 Suppl 2:S26-32.

Wei K, Jayaweera AR, Firoozan S, Linka A, Skyba DM, Kaul S. Quantification of myocardial blood flow with ultrasound-induced destruction of microbubbles administered as a constant venous infusion. Circulation 1998;97:473-83.

Weller GE, Lu E, Csikari MM, Klibanov AL, Fischer D, Wagner WR, Villanueva FS. Ultrasound imaging of acute cardiac transplant rejection with microbubbles targeted to intercellular adhesion molecule-1. Circulation 2003;108:218-24.

Weller GE, Villanueva FS, Klibanov AL, Wagner WR. Modulating targeted adhesion of an ultrasound contrast agent to dysfunctional endothelium. Ann Biomed Eng 2002;30:1012-9.

Weller GE, Villanueva FS, Tom EM, Wagner WR. Targeted ultrasound contrast agents: in vitro assessment of endothelial dysfunction and multi-targeting to ICAM-1 and sialyl Lewisx. Biotechnol Bioeng 2005;92:780-8.

Werner RG. Economic aspects of commercial manufacture of biopharmaceuticals. J Biotechnol 2004;113:171-82.

Wetzel SK, Ewald C, Settanni G, Jurt S, Pluckthun A, Zerbe O. Residue-resolved stability of full-consensus ankyrin repeat proteins probed by NMR. J Mol Biol 2010;402:241-58.

Wetzel SK, Settanni G, Kenig M, Binz HK, Pluckthun A. Folding and unfolding mechanism of highly stable full-consensus ankyrin repeat proteins. J Mol Biol 2008;376:241-57.

Whittingham TA. Contrast-Specific Imaging Techniques: Technical Perspective. *Contrast Media in Ultrasonography*: Springer, Berlin, Heidelberg, 2005. 43-70.

Willmann JK, Cheng Z, Davis C, Lutz AM, Schipper ML, Nielsen CH, Gambhir SS. Targeted microbubbles for imaging tumor angiogenesis: assessment of whole-body biodistribution with dynamic micro-PET in mice. Radiology 2008;249:212-9.

Wilson K, Homan K, Emelianov S. Biomedical photoacoustics beyond thermal expansion using triggered nanodroplet vaporization for contrast-enhanced imaging. Nat Commun 2012;3:618.

Wilson SR, Greenbaum LD, Goldberg BB. Contrast-enhanced ultrasound: what is the evidence and what are the obstacles? AJR Am J Roentgenol 2009;193:55-60.

Witztum JL, Steinberg D. Role of oxidized low density lipoprotein in atherogenesis. J Clin Invest 1991;88:1785-92.

Wong P. Science of Ultrasound and Echocardiography, In: W. M-H, ed. *Transesophageal Echocardiography for Congenital Heart Disease*. London: Springer, 2014. 1-48.

Wu H, Rognin NG, Krupka TM, Solorio L, Yoshiara H, Guenette G, Sanders C, Kamiyama N, Exner AA. Acoustic characterization and pharmacokinetic analyses of new nanobubble ultrasound contrast agents. Ultrasound Med Biol 2013;39:2137-46.

Xu N, Cai G, Ye W, Wang X, Li Y, Zhao P, Zhang A, Zhang R, Cao B. Molecular imaging application of radioiodinated anti-EGFR human Fab to EGFR-overexpressing tumor xenografts. Anticancer Res 2009;29:4005-11.

Yanagisawa K, Moriyasu F, Miyahara T, Yuki M, Iijima H. Phagocytosis of ultrasound contrast agent microbubbles by Kupffer cells. Ultrasound Med Biol 2007;33:318-25.

Yin T, Wang P, Zheng R, Zheng B, Cheng D, Zhang X, Shuai X. Nanobubbles for enhanced ultrasound imaging of tumors. Int J Nanomedicine 2012;7:895-904.

Zahnd C, Amstutz P, Pluckthun A. Ribosome display: selecting and evolving proteins in vitro that specifically bind to a target. Nat Methods 2007;4:269-79.

Zahnd C, Wyler E, Schwenk JM, Steiner D, Lawrence MC, McKern NM, Pecorari F, Ward CW, Joos TO, Pluckthun A. A designed ankyrin repeat protein evolved to picomolar affinity to Her2. J Mol Biol 2007;369:1015-28.

Curriculum Vitae

Alexandra Kosareva

Date of Birth: 16.12.1990
Nationality: Russian
Place of Birth: Snezhinsk, Russia
Working address: Department Biomedicine
Universitätsspital Basel
Hebelstrasse 20
4031 Basel
Email: Alexandra.kosareva@unibas.ch

Education

May 2017 – Feb 2020	PhD in Biomedical Research, University Hospital of Basel PhD Thesis: Targeting of vascular cell adhesion molecule 1 with an ultrasound contrast agent bearing Designed Ankyrin Repeat Proteins
Oct 2013 – Oct 2016	Master of Science in Biochemistry, Technical University of Munich Master Thesis: Renilla Luciferase Labeled MFG-E8, a Novel Probe forthe Analysis of Dead Cells Thesis accomplished at Ludwig-Maximilian University of Munich
May 2014 - Jun 2014	Research Internship, Belgian nuclear research center - SCK•CEN
Oct 2010 – Oct 2013	Bachelor of Science in Biochemistry, Technical University of Munich Bachelor Thesis: Force Spectroscopic Investigation of the Kinesin Stalk 2 Domain of Drosophila melanogaster using Optical Tweezers
Oct 2009 – June 2010	Studienkolleg bei den Universitäten des Freistaates Bayern, M-Kurs
Sep 2008 – June 2009	Moscow State University, faculty of biochemistry
Sep 1997 – Jun 2008	School Education: Gymnasium Nr. 127, Snezhinsk, Russia

Work Experience

Jan 2015 – Apr 2017	Student Research Associate (part-time), Ludwig Maximillian University of Munich

Publications

Kosareva A, Abou-Elkacem L, Chowdhury S, Lindner JR, Beat A. Kaufmann (in press) Seeing the invisible – ultrasound molecular imaging. Ultrasound Med Biol.

Punjabi M, Xu L, Ochoa-Espinosa A, **Kosareva A**, Wolff T, Murtaja A, Broisat A, Devoogdt N, Kaufmann BA (2019) Ultrasound molecular imaging of atherosclerosis with nanobodies: Translatable microbubble targeting murine and human vascular cell adhesion molecule 1. Arterioscler Thromb Vasc Biol. 2019 Dec;39(12):2520-2530.

Languages

Russian	Mother tongue
German	Fluent
English	Fluent